# Operational Behavior Of A Doubly-Fed, Permanent Magnet Generator For Wind Turbines

by

## Sivananda Kumjula Reddy

B.E., University of Madras (May 2003)

Submitted to the Department of Electrical Engineering and Computer Science
in partial fulfillment of the requirements for the degree of

Master of Science

at the

MASSACHUSETTS INSTITUTE OF TECHNOLOGY

June 2005

Author . . . . . . . . . .      . . . . . . . . . . . . . . . . . . . . . .
Department of Electrical Engineering and Computer Science
May 06, 2005

Certified by. . . . . . . . . . . . . . . . . . . . . . . . . . . . . . . . . . . . . . . . . . . . . . . . . . . . . . . . .
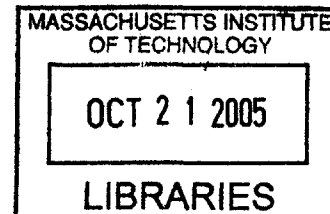Professor James L. Kirtley Jr.
Professor of Electrical Engineering
Thesis Supervisor

Accepted by . . . . . . . . . .
Arthur C. Smith
Chairman, Department Committee on Graduate Students

# Operational Behavior Of A Doubly-Fed, Permanent Magnet Generator For Wind Turbines

by

Sivananda Kumjula Reddy

## Abstract

Greater efficiency in wind turbine systems is achieved by allowing the rotor to change its rate of rotation as the wind speed changes. The wind turbine system is decoupled from the utility grid and a variable speed operation is implemented. Since wind speed varies, the shaft speed should too. But electrical output frequency should be synchronous and Induction machines on their own do not allow for variable ratio of shaft speed to electrical frequency. Permanent Magnet(PM) machines have major advantages: Efficiency and power density are both high; they are also inherently synchronous. A prototype ($\sim$20 kW) of a novel hybrid machine that encompasses the desired features of Permanent Magnet Generators and Doubly-Fed Induction Generators (DFIGs) is being built. This novel geometry machine has to be tested for stability on a test-bed and controlled using an appropriate power electronics and controller circuit.

A MATLAB $5^{th}$ order model of the machine is built, linearized, simulated and examined for stability. The dynamics of the PM rotor is studied. The electrical equivalent behavior of this component of the machine is vital because the frequency of the output power is a direct function of its mechanical speed. As a culmination of this research work, possible paths for the scope of future work on this technology is presented.

Keywords: wind turbines, modified torus geometry, permanent magnet, doubly-fed induction, dynamic state-space model, electromechanical stability analysis.

Thesis Supervisor: Professor James L. Kirtley Jr.
Title: Professor of Electrical Engineering

# Acknowledgments

*To my parents,*
*Nandagopal and Swapna Reddy,*
*who have been a great inspiration*
*and made sacrifices for us.*

# Contents

# List of Figures

# List of Tables

# Chapter 1

# *Introduction*

## 1.1 Motivation

*"Electric power is everywhere present in unlimited quantities and can drive the world's machinery without the need of coal, oil, gas, or any other of the common fuels."*

– Nikola Tesla

On his $77^{th}$ birthday in 1933, Nikola Tesla made the above declaration and in response to a journalist's question on whether the sudden introduction of his principle would upset the contemporary economic climate, replied that it was already badly upset. Wind energy being a cost-effective and reliable solution is the ideal power source for many applications. Research advances over the last 25 years have helped drop the cost of extracting energy from the wind dramatically by around 85%. Moreover several incentives like the net metering provisions and federal production tax credit made available in some regions help improve the economics of wind energy.

Combining the efficiencies of both the rotor (turbine) and generator, an all-encompassing 'system efficiency' can be defined. The world's best turbines can convert about 40% of the wind's energy to mechanical energy. Today, with a typical generator, efficiencies of about 85% can be reached. Hence the wind energy conversion system equipment can achieve a maximum overall efficiency of around 35%. These conversion numbers compare favorably with other energy conversion technologies. Typical commercially available photovoltaic modules have efficiencies of less than 15%; conventional power plants have 30% to 40% thermal efficiency.

There are also expected to be advances in technologies related to wind turbine components which clearly promise to increase productivity and push costs down further. Current research include technologies such as airfoils developed specifically for wind turbines, sophisticated control systems that adapt to complex operating mechanisms, innovative generators (combining conventional technologies and altering generator topologies) that will replace commonly used induction generators, and an entire range of rotors designed specifically for

corresponding turbines. The trend in most utility-scale turbines is to build bigger machines, some a few megawatts or more. A record 6,868 megawatts (MW) of new wind power capacity was installed worldwide in 2002 alone, increasing generating capacity by 28% last year, according to figures released from the American Wind Energy Association and European Wind Energy Association. Wind power technology worth $7.3 billion was installed globally, driving total wind power installation to over 31,000 MW, enough to power 7.5 million average American homes (16 million average European homes).

In this scenario the quest for meeting power needs, taking into account economical and environmental factors, more efficiently has brought to the forefront the need to re-examine conventional core generator technologies in wind turbine systems. The focus is on more efficient energy capture, thereby reducing cost for a given capacity. An excellent report compiled, listed in [5], describes in great detail trends in wind turbine generator design and their associated power electronics. The survey indicates that major investment of wind turbines will in the future be done in wind farms with hundreds of MW power capacity. In order to maintain system stability it is important that each wind farm can provide voltage and frequency control by means of power electronic systems. In conclusion, the report adds:

"[As] recommendation for further research in this area it can be mentioned:

- Study and analysis of switched reluctance machine for high-power applications in wind turbines;
- Study and analysis of transverse flux machine for high-power applications in wind turbines;
- Study and analysis of double-fed induction machine and converter optimization;,
- High-voltage machine design for wind turbines;
- Optimization of back-to-back PWM-VS converter;
- Study and analysis of matrix and multilevel converter for wind turbine application;
- Identification and analysis of new power converter topologies."

Ideally wind turbine and generator development should not be a pursuit of pure technological innovation alone, but research must include a judicious amount of economics to deliver a good number of kWh at the lowest possible cost to the community. Improving the technical efficiency of a wind turbine is not of paramount importance, indeed it is unnecessary given that wind as a resource is plentiful and saving it is not a priority. It is however vital that in a fixed period, the quantity of electrical energy generated must be as high as optimally possibly since turbine installation, rotor construction etc. incurs a certain amount of opportunity cost per installed area.

## 1.2 Previous Work

A series of developments in the area of electric machine design over the last few years has led to several topologies being proposed for wind turbine systems. Beginning with the more traditional variety of fixed speed turbines and constant speed generators, each design overcame major issues of control and flexibility in its own unique way. However, the most important consideration is to have constant frequency output power despite a varying wind speed input at the driveshaft. This is vital because a variable speed operation of the wind turbine system allows for much higher efficiencies of energy capture. In this aspect, two important configurations have particularly stood out.

### 1.2.1 Doubly-Fed Induction Generators

Induction machine technologies were developed by Nicola Tesla in the later years of the 19th century and has undergone significant improvements ever since. Doubly-Fed Induction Generators (DFIGs) are a popular choice among wind turbine designers and manufacturers for most variable speed applications. The power electronics package for this machine would need to handle only around 20-30% of the total power. This allows for losses, especially within the package, to be greatly reduced. A detailed introduction to this configuration is in [20].

The capability of synchronous operation and independent control of the reactive and active components of power has enabled the DFIG to be used as a wind power converter and in hydroelectrical systems as well. Power is extracted from the stator (as it is done in a conventional induction generator), and via an AC/DC/AC converter, from the rotor. This method is perhaps one of the most widely used for the purpose.The machine can thus be operated in sub-synchronous and super-synchronous zones by using the right power electronics which handle a certain percentage of the total power. A scheme such as a back-to-back PWM inverter as suggested in [17] could be implemented. The super-synchronous mode allows power to be extracted from the rotor. This increases the effective capacity of the machine. Of all systems known to the wind energy community it has been shown that DFIG wind turbines are more stable under grid fluctuations than standard induction generators [14].

The most attractive feature of DFIGs from the wind energy extraction stand-point however is its ability to take a variable speed (variable rpm) and produce a constant frequency output. The rotor is excited by a voltage the magnitude and frequency of which can vary independently. The superimposition of the injected excitation frequency to the rotor on the actual rotor speed creates a synchronous rotating field.

Hence variable speed constant frequency characteristics over a wide speed range is obtained. The excitation voltage magnitude can be varied to control the stator and rotor power factor thus achieving maximum efficiencies. The angle, $\alpha$ between the stator and rotor voltage
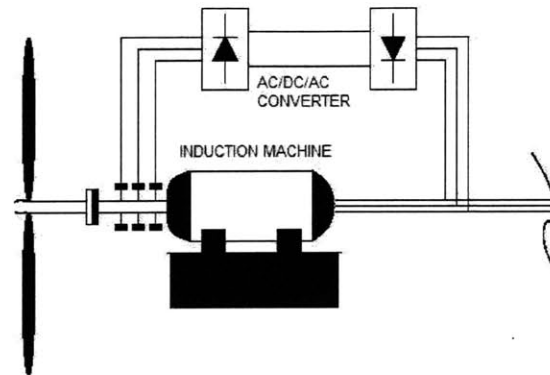
Figure 1.1: Schematic of a Doubly-Fed Induction Generator

phasors can be altered to control the active power delivered. A schematic of the DFIG is show in Figure 1.1.

### 1.2.2 Permanent Magnet Generators

Permanent Magnet (PM) generators have also been proposed for similar wind turbine applications. They differ from the Induction Generator in that the magnetization is provided by a PM system in the rotor and not by excitation current from the armature winding terminals as in induction generators. In this case the mode of operation is synchronous and not asynchronous. The ability to self-excite is an attractive feature that makes it a suitable choice for operation at higher power factors and efficiencies. It is very reliable and has unity or leading power factor design. A key advantage of this technology is its high power density.

On the flip-side, construction of such machines on a large scale or for utility-scale purposes is especially cumbersome because of management issues related to the magnets. Hence increased manufacturing costs have been the bane of this scheme. PM material is also expensive and moreover the cost of the power electronics necessary for this system do not justify the overall advantages.

Permanent magnet machines do have overloading capability and full torque capability at zero and very low speeds. The low volume of this design is an attractive plus as well. However, the features that interest us most about this technology are its high efficiency and power density.
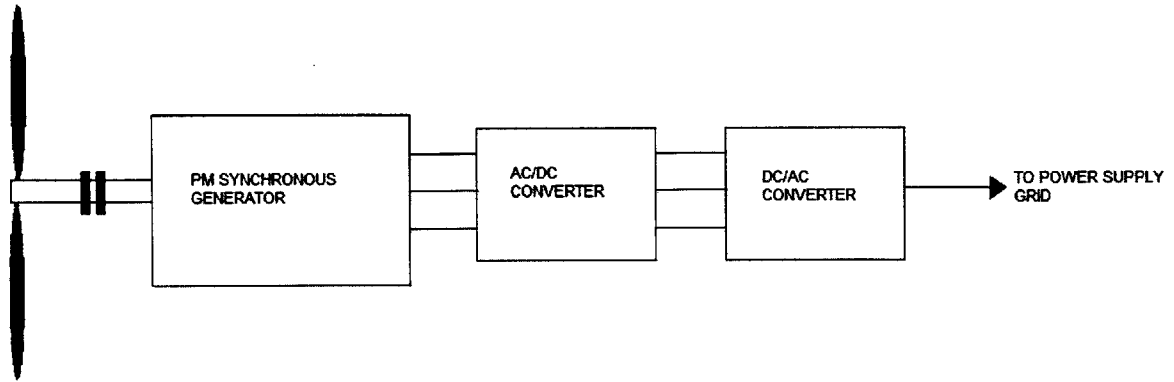
Figure 1.2: Schematic of a PM Synchronous Generator connected to the grid

### 1.2.3  Hybrid Technology Generators

The apparent advantages of the topologies descried above can be combined to create a hybrid machine the behavior of which is the subject of this thesis. Hybrid electrical machines of this or similar type are not new to the wind energy community. In a survey of generator technologies and power electronics, with respect to wind turbines[5] several topologies were examined and their performances documented. These include a few hybrid machines and results indicated the need for combining technologies to encapsulate desired features in a single unit.

The doubly-salient PM generator [18], describes a hybrid technology which does not claim to improve performance of the single rotor type. However, it is a demonstration of how saliency is added to improve performance. Additional magnets are used to bias the magnetic circuit.

Hybrid Axial Flux PM Generator with salient poles is another hybrid technology configuration described in [15]. The design is modular and the assembly is simplified while the stator is wound like a torus.

An image of our hybrid technology generator within the power system is shown schematically in Figure 1.3.

## 1.3  Research Progress

The bulk of the research work done so far is contained in quarterly reports to the original sponsors of the project, the National Renewable Energy Laboratory (NREL), [12]. MIT graduate student, Andrew Thomas has documented the progress and mechanical engineering
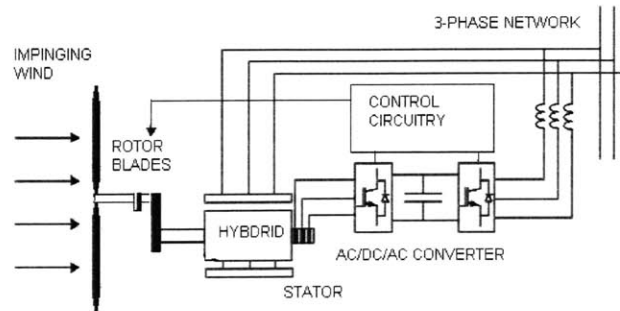
Figure 1.3: Schematic of our Hybrid machine technology connected to a typical 3-phase power system network.

features of the hybrid machine in his thesis [19].

The project involves the design and construction of a 20kW prototype of a hybrid technology Dual Rotor Constant Frequency, Variable Speed Generator for Wind Turbines. The machine is essentially a DFIG with an additional set of PM rotors. It has been mounted on a test rig and undergone initial tests with a Hyper Terminal operated dynamometer which later can be advanced to a LABVIEW-based system.

The development of optimization techniques to find a set of parameters given certain constraints is not covered in detail here but prior to actually building the prototype machine a design paradigm[1] called the "Novice Design Assistant" (NDA) which uses the Monte Carlo scheme for generating candidate designs and multi-attribute evaluation of those designs was used. More information about this aspect of the design process is covered in great detail with the actual MATLAB code in [12].

A radial geometry machines like most conventional systems cannot be used to implement the hybrid concept. The design requires two rotors and the construction of such a machine would be embarrassingly complicated. The addition of permanent magnets in the geometry of the DFIG system is supposed to allow for more manufacturing tolerances as air gaps need not be small and winding slots can be eliminated.

---

[1]The NDA is a computer aided tool for designing three-phase induction motors and was used in the [Continued...] trade-off analysis for our machine to come up with an optimum set of *'attributes'*. Attributes in this context are associated with the design process; all things being equal, they can either be maximized (e.g., a quantity like efficiency) or minimized (e.g., a quantity like cost). Further discussion about optimization to find a set of machine dimensions as well as materials and methods of assembly to come up with the best machine can be found in [10].

The Torus is a machine geometry developed in the United Kingdom. It uses axial flux, permanent magnets and a Gramme-Ring (winding strategy to obtain as near as possible a sine wave) stator. It is relatively compact and efficient. Thomas also touches upon the fact that the machine will have better thermal efficiencies as a result of the wider dimensional constraints and the axial geometry.

We modified the torus geometry to add another pair of rotors. Now, it has a PM rotor (freely spinning, fitted with bearings to the shaft) and a power rotor (wound rotor, fixed to the shaft).

## 1.4 Thesis Scope

This thesis includes an account of the design and construction of the prototype and the challenges encountered. Since [11], the design has evolved and the completed machine has been mounted on a test-rig and coupled to a dynamometer.

Thomas[19], in his analysis of the hybrid machine came up with a full blown $10^{th}$ order model which very succinctly describes the dynamic response of the machine to sudden perturbations and load changes. However it fails on actual implementation because of its unwieldy nature and it also presents an interfacing problem. Higher order models are a bane since MATLAB simulations require infinitesimally smaller time steps and fewer number of state variables to carry out the computations in each iteration faster and more accurately. In this thesis a straightforward $5^{th}$ order model will be presented and a demonstration on how it can be used to describe the machine's dynamic behavior and stability will be explored. Of course to completely describe the dynamic behavior of the technology, the model must approach simulation of real machine dynamics and to do this one must account for several damper circuits which if nothing contribute to increasing the order.

Mathematical models of the machine predict encouraging performance data. This thesis will cover an investigation into the operational characteristics of the machine. A series of simple preliminary tests conducted on the machine will be described and the results presented (Chapter 5). This early data will be analyzed, but is not expected to provide any significant insight into the machine's behavior when coupled to a power system.

This thesis does not cover the analysis of wind profile data (which could either be meteorological or artificially generated) and the use of this information for the modeling of wind - wind turbine interaction phenomena. The dynamic attributes of the wind turbine system can only be determined if due consideration is given to these tasks. It is an important part of the process necessary to develop a complete representation of the new technology. However much of the groundwork related to this aspect of the research has already been laid down by previous researchers within the wind energy community.

Two important considerations, also not covered in this thesis, integral to any electrical machine design and simulation models are the power electronics package that feeds the

power rotors and the control system. At the time of writing this thesis, a power electronics component has been built and tested. Again, much of design work anticipated for developing this component is expected to go along the lines of standard DFIG systems. Vector-control techniques have already been well discussed for doubly-fed induction generators using back-to-back PWM converters in related literature [16]. Monitoring the nature of the power output to the mains (purely real power - stator output current is in phase with the mains voltage) and other control related tasks for the hybrid machine have been discussed briefly in [19] but much work remains to be done.

## 1.5 Thesis Organization

The next chapter covers in detail the engineering challenges and a description of the approaches to them. Previous work and the evolution of the design is also covered and a brief overview of methods considered at the outset of the research.

Chapter 3 with present the actual dynamic analysis of the machine. A well contained first order model is presented and simulated. The results are presented and examined.

Steady state values are obtained from the simulation and used in the linearized model that is the subject of Chapter 4. Also a full-blown linearized model is developed that is able to predict the stability of the dynamic system.

A few preliminary tests were carried out on the prototype machine. The results of these tests are presented in Chapter 5 and interpreted. Information on a power electronics package which uses a microcontroller is given at the close of the chapter.

The setup of the test-rig is described and shown schematically in Chapter 6. Additionally, configuration details of the dynamometer and Hyper Terminal to control the speed of the machine are explained.

An overview of what was accomplished is given in the last chapter. Also, the path for future research with this technology is charted and the groundwork is laid out. Techniques employed to simulate wind data and its use to observe the machine's operational behavior as well as to finally generate power curves for comparison of the technology with others in the same power class.

The appendices include relevant technical notes and photographs of the machine as well as additional drawings.

# *Design and Construction Details*

This chapter supplements an account of the construction tasks and processes described in [12] and comments briefly on the design and constructional features of the novel technology variable speed constant frequency machine. The sixth report cited above describes in excruciating detail the difficulties encountered while dealing with the stator and rotor windings, the slip-ring assembly to feed the rotors, the redesign of the machine housing and setting up the test-rig. Thomas, over two theses describes the finer aspects of these processes and the technical challenges we encountered. After his work was completed several additional changes of the design had to be made and implemented. Details of these alterations are presented in this chapter.

Construction-related operations, external to the machine itself, such as developing forms to build the coils and a mounting rig to test and balance the rotor assembly, constantly evolved and took up a bulk of the time and resources. This chapter also briefly covers few aspects of alternative designs which were not pursued because of mechanical engineering constraints. A couple of *in situ* tests to verify the integrity of the windings of the stator and rotor are described.

## 2.1  Design Approach

The montecarlo based design synthesis tool, Novice Design Assistant (NDA) which was introduced briefly in the Introduction to this work is a Matlab program that uses a multi-attribute approach to evaluation of machine designs [9]. A Pareto surface, the design frontier, is constructed presenting an optimum solution. Six variables including winding thickness, magnet thickness, inner radius, outer radius, iron axial length, and relative rotation gap were considered. Five attributes, namely efficiency, magnet mass, iron mass, winding mass and leakage reactance were also included.

The MATLAB script using for this process is presented in the appendix to [9]. A list of design attributes is generated for each scenario and one is selected which represents the optimum machine. Some of the dimensions generated by the script are; rating of 10 kW, frequency of 60 Hz, rotor inner and outer radius of 27 and 35 cms, 10 pole pairs, a voltage per turn of approximately 1.12 V. The projected efficiency of this machine was 90.08%.
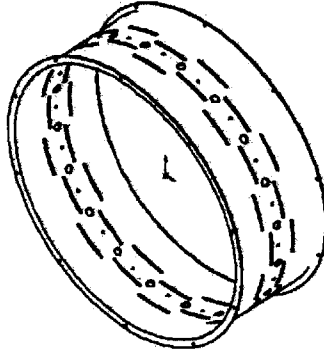
Figure 2.1: SolidWorks impression of the original housing. *(Source: A. Thomas)*

## 2.2   Housing and End Plates

The housing of the machine had undergone a design evolution at the mid-construction stage which was necessitated by a manufacturing error. The primary purpose of the housing was to hold the stator in place and also to provide a means of transferring the weight of the machine to the end plates and eventually to the test-bed mounting points. Several active torques are present in the machine the effect of which are greatly reduced by the sheer radial dimensions of its structure. Thus, the aluminum end plates and the housing material has a small thickness.

The initial design provided for a slotted cylindrical housing that would encompass the stator and rotors. The MIT Central Machine Shop built the rolled and welded aluminium housing. However it was realized during construction that the housing had a smaller peripheral radius and could not accommodate the overhang portions of the power rotor windings. Moreover the stiffness of the stator winding wires made it extremely difficult for the wires to be bent and forced out through the holes provided for it on the original housing. A picture of the original housing is show in the appendix with the machine pictures; a drawing is produced in Figure 2.1. To allow the cooling air to escape ventilation slots were provided which ran around the circumference of the sleeve at the location of the 4 rotational gaps. These slots took up about 50% of the circumference.

The new housing design was far less elegant and assumed a "skeletal" structure. A rolled and welded aluminum ring was employed for the purpose and 10 C-section aluminum 'stringers' were used to reach across to the two end plates. The cross sectional area of the aluminum bars are around $1 \times \frac{3}{4}$" inches which is approximately the same if not greater than the
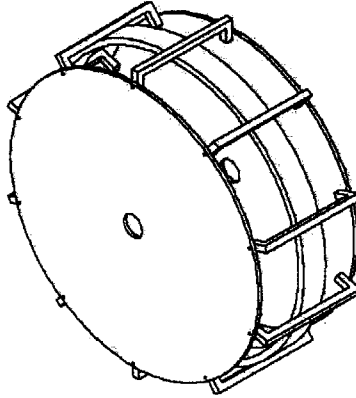
Figure 2.2: SolidWorks impression of the new "skeletal" housing. *(Source: A. Thomas)*

thickness of the material in the original housing. Hence no structural integrity and torque handling capability was compromised as a consequence. A SolidWorks impression of this new housing is shown in Figure 2.2. Other design issues specific to each component in the construction process are covered in the following sections.

The C-section aluminum stringers were built to bridge the two end plates and also to provide support and transfer the weight of the machine to its base. A dimensioned picture of a single stringer is shown in Figure 2.3.

## 2.3   Stator And Rotors

The stator and two power rotors are built from the same core while the Permanent Magnet (PM) rotors have 20 magnets embedded in each of them. The power rotors are mounted on thick aluminium discs. Air must be forced to flow axially down the center of the machine, rather than around the end of the rotors. The rotors have concentric circles of holes for the passage of air to cool the system. The thermodynamics of the air flow necessitates a path from the outer surface of the end-plates via the holes and out of the periphery of the machine. The airgaps in the machine forces the air to move outward radially.

The ventilation scheme just described keeps the temperature of the wiring and the core within permissible levels less than 80°C which is an acceptable value; anything more than 80°C may be detrimental to the insulation and the epoxy-fibre protection of the stator windings and the power rotor coils. At this point, it is not out of place to mention how the earlier housing design provided for a neat ventilation scheme.
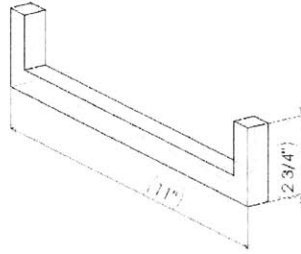
Figure 2.3: One of 10 C-Section stringers that bridge the two end plates and provide a housing for the machine.

The slots of the cylindrical housing was expected to provide a culmination of the airflow path in the machine. In the case when the natural ventilation scheme was not sufficient, blowers[1] were to be mounted to each endplate and air forced into the moving system. Improvised sealing methods to prevent the flow of air through the space between the end plates and the beginning of the rotor assembly around the power rotors were also considered in anticipation of the eventuality.

### 2.3.1   Magnetic Cores

There are 3 magnetic cores in the machine, one in the stator and one in either power rotor. The primary purpose of the core is to provide a path for the flux between the poles of the magnets. For this reason, the reluctance of these cores must hence be as low as physically possible. Silicon electrical steel has high permeability. M-19 steel, a medium grade non-oriented steel which also has low conductivity was selected.

The core was wound from a strip (thickness less than skin depth $\approx 0.35$ mm) of this material until it was thick enough for the purpose and dipped in a low-viscosity epoxy. The strip had an coating that provided insulation between subsequent layers. A rotor core thickness of 16.5 mm was developed. For the stator core, twice that value $\approx 33$ mm sounds reasonable as the core will have to handle flux from two sides.

---

[1]Covered in [12]. Two blowers of $0.1 m^3/s$ rating, one on each endplate were decided upon. Generated heat that would have caused a temperature rise of as much as 20 K would have to be dissipated.
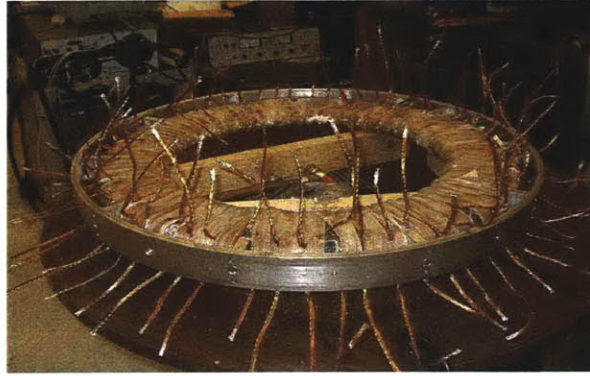
Figure 2.4: Stator: The winding ends here are yet to be soldered before the stator is assembled with the rest of the machine.

### 2.3.2   Stator Design details

The stator is a tape-wound steel core with a 20-pole 3-phase winding. The core was fabricated from magnetic strip steel which was wound onto a wooden form and impregnated with epoxy resin and finished with a fibreglass cloth wrap. Four such tape wound cores were made, and two of these were combined to form the stator core.

The two sides of the stator must consist of current carrying conductors in the moving magnetic field. A form of winding called the Gramme-Ring winding is employed for this purpose. The windings wrap all the way around the rectangular cross-section of the toroidal stator. They are made up of sixty coils, each with ten turns and fabricated of flat transposed Litz wire consisting of seven conductors of number $16\frac{1}{2}$ AWG wire. For the same power handling capacity if a single wire with the same thickness was used skin-current losses would occur. Two levels (5 turns on each level) of closely spaced and pressed wire just fits into the space assigned for it. The stator winding handles the majority of the power in our machine. An image of the completed stator within the stator ring is shown in Figure 2.4.

### 2.3.3   PM Rotors Design

The permanent magnet rotors are mounted on bearings on the shaft and are free-wheeling. They are not coupled to an external shaft. The permanent magnet material used is Neodymium-Iron-Boron (NdFeB) with an energy product of approximately 42 MG-Oe. Each rotor disk has 20 magnets which are inserted into the cavities one at a time, ensuring that the polarity of the magnets alternates in this manner: N-S-N-S. This was done with the aid of a small compass. The bonded NdFeB magnets are composed of rare earth magnetic materials which is superior to bonded ferrite magnetic material. They have approximately
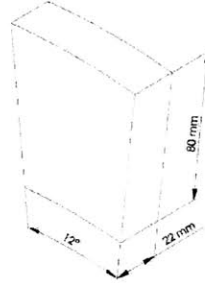
Figure 2.5: Dimensioned drawing of a magnet inserted into slots provided for it in the magnet rotor. *(Source: A. Thomas)*

15% more remnant flux density to weight ratio and also a higher coercive force. NdFeB has nearly twice the $B_r$ and $H_c$ of ceramics.

However they also have a lower operating temperature (120-170°$C$) compared to ferrite based magnets (200-320°$C$) and are several times more expensive.

The magnet rotor plates are aluminum discs 23 mm thick, with cavities machined into the active region that begins around 40 mm from the periphery of the rotor. he dimensions of a magnet that fit into one of these cavities are shown in Figure 2.5.

Once the permanent magnets are embedded into cavities specially made for them on an aluminum disk, they are then bonded with epoxy and covered by thin sheets of aluminum around 0.75 mm thick. A picture of the finished PM rotor disk is presented in the appendix, Figure 2.6(b). The magnet rotors are free spinning and must rotate independent of the other moving parts of the machine. The two rotors on either side of the stator are coupled together with a freewheeling shaft that is hollow in nature and fixed with bolts to holes around the periphery of the bearing which bears upon the driveshaft. The coupling is necessary to force the two PM rotors to move together.

Each rotor disk has 20 magnets which are inserted into the cavities one at a time, ensuring that the polarity of the magnets alternates in this manner: N-S-N-S. This was done with the aid of a small compass.

Images showing the PM rotor in different stages of assembly are presented in Figure 2.6.

### 2.3.4 Power Rotors

The pair of power rotors are coupled securely to the shaft. There are two rotors, one on either side of the stator and each is mounted with a core and 60 phase coils. These coils
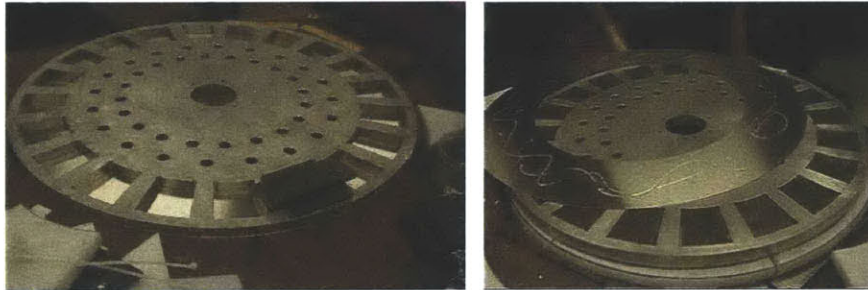
(a) PM Rotor: The slots where the magnets go in are clearly visible. A sample magnet is also shown.



(b) PM Rotor: Assembled, an aluminium plate is glued over the arrangement to keep the magnets in place and also protect it from the other moving parts of the machine.
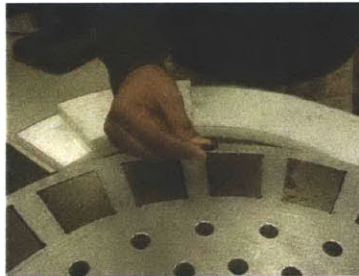


(c) PM Rotor: Poling the magnets to ensure that they are placed correctly in the N-S-N-S fashion.

Figure 2.6: Various stages of magnet rotor assembly.

are conventional in nature but are wound in a different way. The coils are roughly diamond shaped, and are bent so that overlapping coils are made to lay flat on the face of the rotor core. They are also specially shaped to facilitate proper nesting.

A power rotor plate is used to support the rotor core and the windings. The rotors interacts with the rest of the electromagnetic system on one face only and hence they experience a very strong attractive force from the permanent magnets. To keep the rotors from violating the air-gap, the power rotor plates need to have sufficient thickness to support that force. Moreover the two rotors are balanced using the aluminum plates, by drilling holes on the periphery to remove material at strategic distances from the center of the plate. Two 1.75 in. thick aluminum plates are used for these purposes. These plates are slotted for ventilation and have a keyed hole at the center. The keyway is built to withstand the maximum expected torque on it. Details of the mechanical engineering aspects can be found in [12].

Power at slip frequency (skin effects can be neglected) dissipated in the windings is low ($\approx$ 1 kW) and is handled using standard 16 AWG wire for the coils. A Gramme-Ring winding scheme would have resulted in a redundant side (the face away from the stator) and also increase the resistance offered to the slip frequency current thus affecting the efficiency.

The magnet rotors were also perforated to allow air to flow through them. This was be accomplished in the same manner as was for the PM rotors, with holes just on the inside of the inner edge of the magnets.

The 120 rotor windings were wounded and tested. Details of their construction are presented in [19] and an image of a few finished windings are shown in Figure 2.7.

The rotor winding integrity was tested using an impedance analyzer. As the inductance of a coil is directly related to the number of turns on it, merely measuring L would be a sufficient test of the winding's integrity. If there were shorted turns in the coil, the analyzer would give it away by indicating too low an inductance value. A threshold level of 23 turns was set below which the coil was either rejected or rewound. A Winding apparatus was conceived and coupled with a lathe to make 120 such coils (60 for each power rotor). An image of the finished power rotor being balanced appears in the appendix, Figure A.1.

### 2.3.5 Checking Stator Winding Integrity

A simple measurement of winding impedance (finding the winding resistance and reactance) was carried out. This simple technique would have betrayed defects in the winding such as short-circuited turns or few turns in the coil. A relative permittivity of $\mu_r = 100$ was assumed. The core cross-sectional dimensions are $A_c = 0.028 \times 0.08$ meters and the circumference, c, which is essentially the length of the mean path around the stator core is 2 m.

$$\frac{L}{N^2} = \mu_r \mu_o \frac{a}{c} = 14\text{mH/turn}^2 \approx 14\text{muH/coil}. \tag{2.1}$$
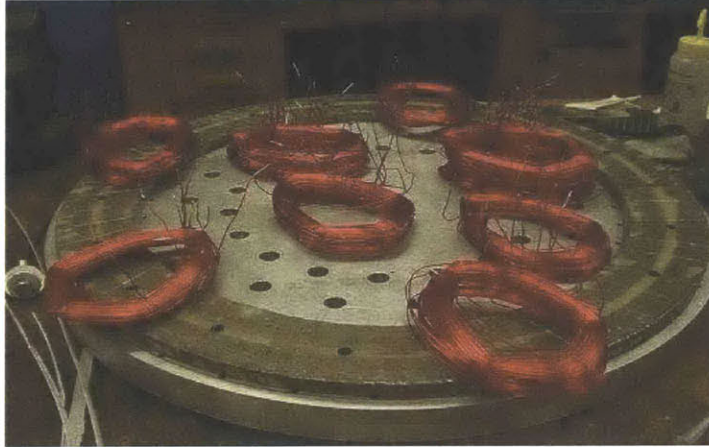
Figure 2.7: Power rotor: Finished rotor windings that were glued to the rotor core.

Another test which we dubbed 'Ring Test' was carried out at rated voltage (full core flux and 60 Hz). It was conducted for the purpose of uncovering any insulation insufficiencies. Ten coils where selected and connected in series with a single phase variac. The rated voltage was slowly stepped up from zero using the variac. An oscilloscope was used to capture the current (using a current probe) and voltage waveforms for $V_{rms}$ = 75 V, 100 V, 150 V and 175 V. The plots of current vs. voltage are shown in Figures 2.8 and 2.9. The ten randomly selected coils when energized with the variac current produced a flux in the core of the stator. Hence currents were induced in the other coils and the completed flux path being closed, eliminated the need to connect the other coils for the same test.

Using the functionality of the oscilloscope, an hysteresis loop of the core on which the stator is wound was obtained by plotting voltage-time (essentially an integral of the voltage across the ten chosen coils) with the current. One such curve is shown in Figure 2.10 for a voltage of $V_{rms}$ = 100 V and a sinusoidal input drive of 60 Hz.

Such hysteresis curves can be used to determine the core flux and saturation field. Also if the curve was traced appropriately, the coercivity of the core material and remanent magnetization in the core can be found. The hysteresis curve of the core indicates a very low magnetic saturation, $B_{sat} \approx 0.55$ Testa. This value corresponds to a magnetic field intensity of $H \approx 120$ A/m.

The remnant magnetization can be read off the graph, $B_r \approx 0.4$ Tesla. Similarly, the coercivity, $H_c$ is around 95 A/m.

**Current vs. Voltage Across 20 Windings**
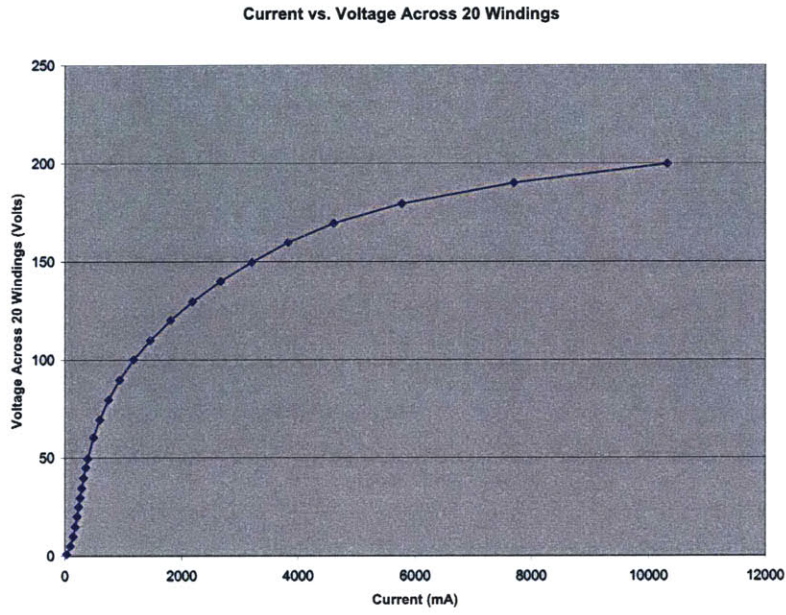


Figure 2.8:  Current vs. Voltage across 20 windings

**Current vs. Voltage of 1 Random Coil**
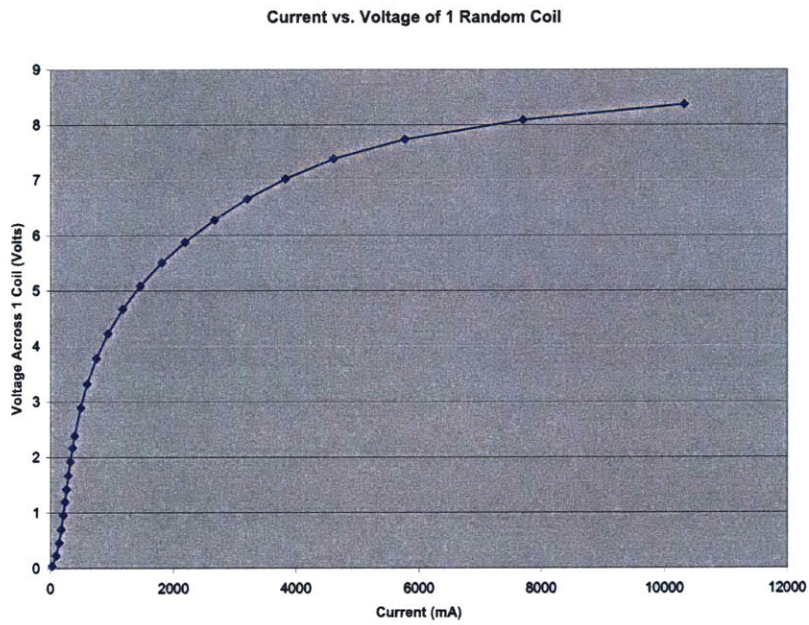


Figure 2.9:  Current vs. Voltage across a single random coil

The electromagnetic phenomena behind these simple observations is easy to follow. The magnetic field intensity, $H$, is given in terms of the current, $i$ and the number of turns, $N$ as indicated in Equation 2.3.

$$H = Ni \qquad (2.2)$$

The flux density in the core is given by Equation 2.3.

$$B = \frac{\int V \, dt}{N A_c} \qquad (2.3)$$

If $B = 1.2$ T, which is not quite achieved, then a voltage per turn ($N = 10$ turns per coil × 20 coils) induced in the stator is given by,

$$\frac{V}{N} = \omega B A = 377 \times 1.2 \times 0.028 \times 0.08 \approx 1 \text{ V}.$$

### Oscilloscope Functionality

Figure 2.10 was obtained on a 2-4 channel (1 mV to 10 V/div Sensitivity) digitizing oscilloscope (Tektronix TDS 744A) using a current probe (maximum current 100 A DC, 600 V bare conductor voltage rating, Tektronix A6303)as input on one channel ($x$- axis) and voltage (proportional to flux density) on the ($y$- axis). After some initial resolution adjustments the two channels were plotted against each other at different voltages keeping the frequency constant. On the TDS 744A this can be done using `Display/Format >> XY-`.

## 2.4 Driveshaft, Free-wheeling Shaft and Bearings

Torsional loading, which is a conservative estimate of the torque handling capability of the generator shaft, was predicted to be around 300 Nm at the time of design [12]. This torque is divided evenly between two rotors due to the symmetry of the structure. Each rotor applies a torque then of approximately 150 Nm on the shaft and an additional 25 Nm must be considered due to the axial forces exerted due to attraction. A stepped and keyed shaft was manufactured for this purpose.

Given that there are considerable amounts of forces being exerted on the shaft, it has to be made of a high-grade steel alloy material. Section 2.4.1 of [19] covers a detailed description of the driveshaft and also presents the final dimensions decided upon. A picture of the driveshaft is presented in Figure 2.11. Accordingly, the minimum shaft diameter that was decided upon was 30 mm. The first shoulder step, 45 mm diameter. The keyways in the shaft measured 2.8 mm deep, 5 mm wide and 48 mm long to key in the power rotor.
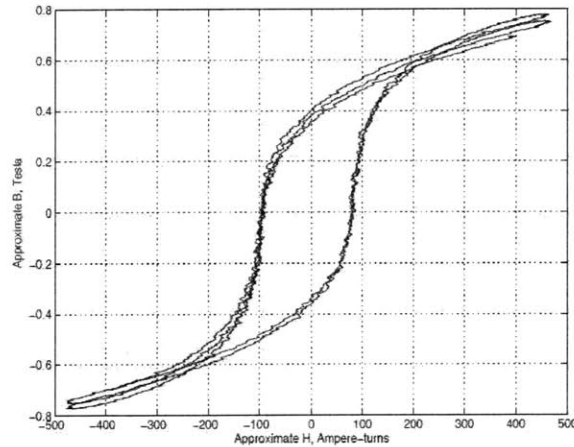
Figure 2.10: Hysteresis loop response for a voltage of $V_{rms} = 100$ V.*(Source: A. Thomas)*

The main bearings are installed within an assembly mounted on the end plates. Images of these bearings are presented in Figure 2.12.

### Free-wheeling Shaft

The free-wheeling shaft couples the two permanent magnet rotors together. This part is fashioned out of aluminum and does not have substantial load exerted upon it. The internal diameter of this shaft is $\approx 48$ mm; just enough to clear the outer diameter of the driveshaft. 6 threaded rods ($\frac{1}{4}$") are used to keep the two PM rotors together and in 'phase'. The outer diameter of this shaft is 120 mm and allows the magnet rotors to be mounted on it.

Special function nuts were made to keep the angular contact bearings in place which has its outer racing bearing against retainer rings within the assembly. To fix the nut on, threads were cut on the shaft for about 45 mm of the way on either side of the center using the lathe thread-cutting functionality. During assembly, the freewheeling shaft must bear axial stress, and under operating conditions, it may be tightly constrained axially, as the clearance to the power rotor and the stator is only about 8 mm.
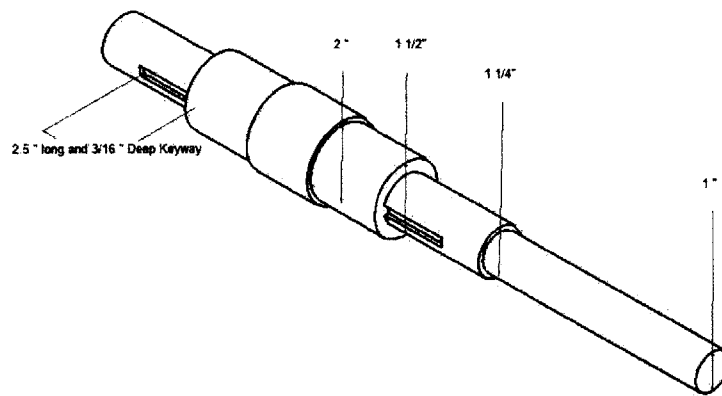
Figure 2.11: Driveshaft element: The power rotors are keyed on to the shaft using the keyways provided for them. Threads (not shown here) were later made on the shaft for special nuts to keep the magnet rotor bearings in place.The length of this element is ≈ 2.2 feet.

(a) Disassembled: Main bearings and casing.



(b) Assembled: Main bearings.

Figure 2.12: Main bearings: The driveshaft is mounted upon this installation which is then fixed to the end plate.
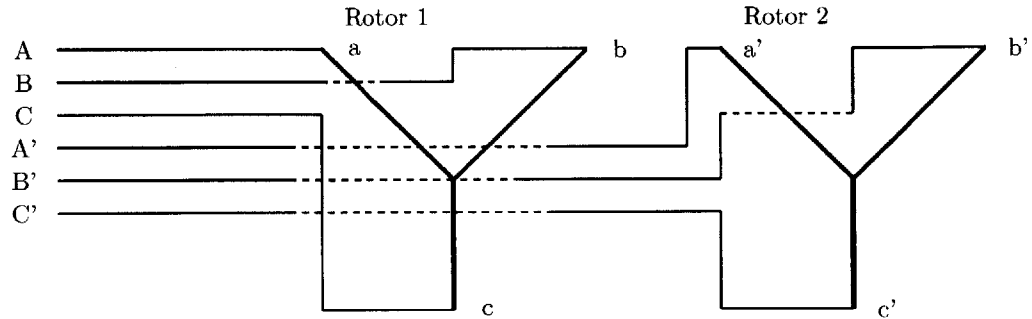
Figure 2.13: Wiring diagram: The two power rotors are connected as a buried neutral Y-connection. The 3 wires that go between the two rotors pass under the bearings through specially made grooves provided in the shaft.

## 2.4.1 Slip Ring Assembly

The wires from the power rotor coils are fed though the shaftway in the center and make their way to the outside face of the power rotor where the are connected to longer leads that travel the length of the shaft to the other outside face. The interesting aspect of the challenge is to come up with a configuration that would minimize the number of wires transiting under the magnet rotor bearings while still feeding all coils in the power rotor arrangement with the same amount of current. A suitable configuration that achieves this was is shown in Figure 2.13. According to the scheme, the far rotor was connected as a floating-wye (buried neutral Y-connection) and the phase ends (3 wires) brought out under the bearings in grooves made for them on the shaft (fiber-glass trapped).

6 ends labelled (a,b,c) for the near power rotor and (a',b',c') for the far rotor were brought out to be connected to the slip ring assembly. For the sake of completeness of literature, other alternative schemes are presented below.

First, the most general of schemes is the obvious 12-ring configuration that allows the power rotors to be wired up in either a $\Delta$ or Wye-configuration or in series and parallel.

An optimum solution that would however make our task harder would be to provide two distinct set of slip-rings as suggested in [19]. This configuration would eliminate the need for wires to traverse under the floating shaft and the bearings. However this configuration would, besides taking up space, need alteration of the existing shaft design and would require a more complicated way of connecting the power electronics to them.
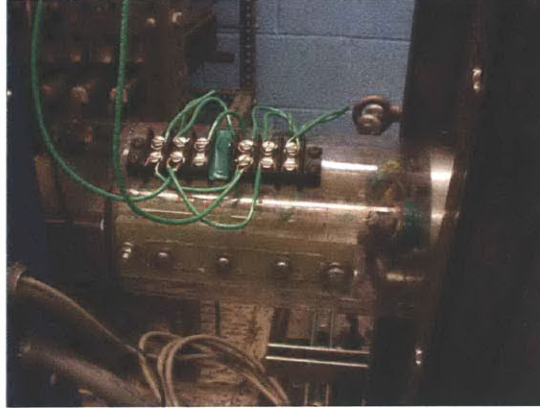
Figure 2.14: Slip-ring and brush holder assembly: The upper set of leads are connected to the corresponding copper bands on the slip-ring and can be labelled from the far left, (a,b,c,a'b'c').

### 2.4.2    Brush Holder Assembly

6 Spring-loaded carbon brushes were connected to each slip ring as shown in Figure 2.15.

A brush holder assembly was fashioned using acrylic plastic tubing and cutting holes in them for the wires to be connected to a set of jumpers on the outer surface. The brushes were affixed to the case and are held against the copper conductive rings, making a rotating contact to the rotor windings. Each copper band on the slip-ring tube corresponds to a phase lead from one of the power rotors. The near three bands correspond to the leads from the far rotor while the far three bands correspond to the leads from the near rotor.

A picture of this assembly appears in Figure 2.14.

## 2.5    Control Scheme

Variable speed operation of the wind turbine is achieved by injecting a variable voltage into the rotor at slip frequency. Vector-control techniques have already been well discussed for doubly-fed induction generators using back-to-back PWM converters as described in [16]. Monitoring the nature of the power output to the mains (purely real power - stator output current is in phase with the mains voltage) and other control related tasks for the hybrid machine have been discussed briefly in [19] but much work remains to be done. Using the three phase transformation (Park's transformation) introduced in Chapter 3 of this work

3- Φ Inverter system (Power Electronics)

A        B        C

(a,b,c), (a',b',c') - Phase leads from
Power Rotor 1 or 2

b        a'       c'

| 1 | 2 | 3 | 4 | 5 | 6 | Slip Ring

a        c        b'
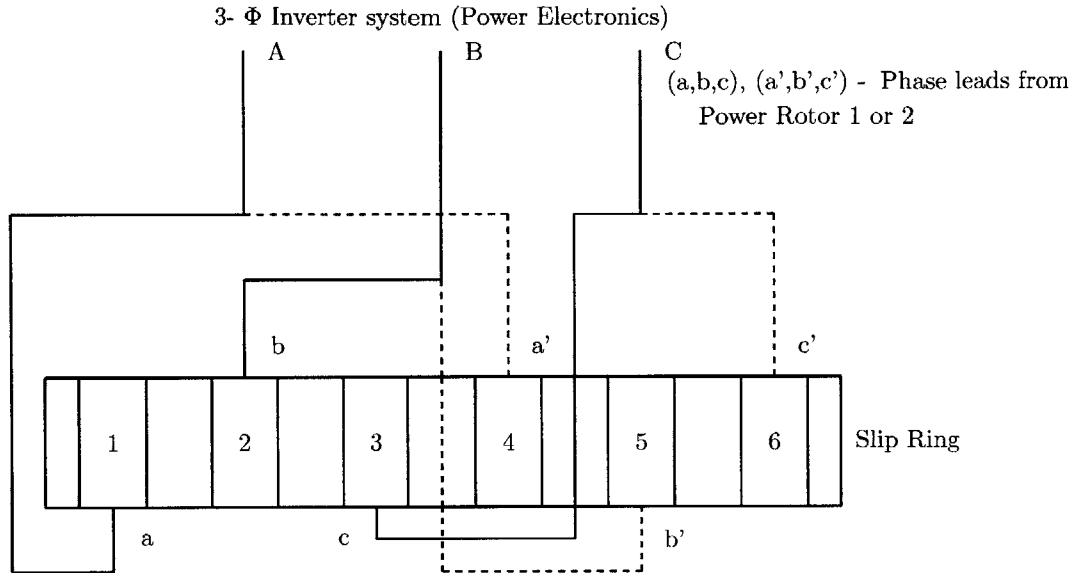
Figure 2.15: Wiring diagram depicting the connections from the slip ring to the power inverter assembly.

and field orientation, a dq- frame is supposed. d- and q- component fluxes representing the flux producing component and the torque producing component respectively are obtained. Now that they are disengaged, these components can be independently controlled using distinct PI controllers. The output of the controller is converted back into its 3-phase quantity using the inverse Park's Transformation. A pulse width modulated output is then used to generate the control signals for the machine using one of three strategies, stator flux, rotor flux or magnetizing flux oriented control.

Another control scheme using microcontrollers (such as PIC16F7X7) is covered in Chapter 5.

## 2.6   Assembly Details

The tasks involved in the assembly of the machine were various and careful planning was necessary to make sure no irreversible changes were made to any portion of the design and assembly. A $1\frac{1}{2}$ ton crane was pressed into service to manoeuvre parts of the machine on the assembly floor.

During assembly, HDPE spacers 5 mm thick were placed strategically in the rotational gaps

to ensure correct spacing until the device was assembled and balanced properly.

The details regarding the assembly process are mundane and will not be covered here. It should suffice to mention though that the process took well over a year. The quarterly reports to NREL covers much of the procedures and techniques to overcome the enormous attractive forces from the magnets during assembly.

A blown-up SOLIDWORKS impression of the assembled machine is shown in Appendix A, Figure A.3.

*Chapter 3*

# Dynamic Analysis: Developing Simulation Models

Power system design codes and standards worldwide are being rewritten to require that winds farms continue to support network voltage and frequency despite system perturbations. Comprehensive simulation models that can be integrated with the rest of the system must hence be built to analyze steady state and dynamic behaviors. The final goal of this research work is develop a generator technology that can be used in a variable speed constant frequency wind turbine. With the increasing penetration of wind power into electricity networks and power grids more elaborate study techniques and tools have to be developed to understand the interaction of wind farms with the rest of the power system.

In this chapter the model of the hybrid Doubly-Fed Induction machine proposed in Chapter 3 of [19] will be carried forward and examined in greater detail. The full-blown tenth order model however complicates the dynamic analysis beyond what is necessary. On further examination of the analysis, a simulation-friendly fifth order working model was developed and is presented. A fairly well accepted notion while developing dynamic models using the $dq-$ rotating frame transformation, is that a synchronous machine rotor can be represented by equivalent windings to describe the various current paths in it. A field winding is supplemented by two damper windings, the d- and q- axis windings which model the paths presented by the rotor body to current flow. If a Permanent Magnet (PM) rotor is employed, then the constant field flux replaces the field winding while representation for the currents in the rotor bodies remain the same.

## 3.1   Overview of the Tenth Order Model

Based on initial analysis, the hybrid Doubly-Fed Induction machine was modeled as a combination of two PM machines. One was considered coupled to the rotating shaft; hence incorporating the effects of the moving frame, and the other, a stationery axial-flux machine which shares its PM rotor with the moving frame machine.

Upon carrying out our very first test on the hybrid machine we discovered that the interaction between the power rotor and the stator was almost negligible. For the test, the power rotor carried upto 15 A of current in its windings (rated for only 10 A) while the machine was spun at approximately 120 rpm. A developed voltage of 67.5 V/phase (peak value) was barely affected by energizing the power rotor circuit. The developed voltage

– **27** –

grew in amplitude and frequency ($\approx$18 Hz at 120 rpm) on the strength of the field created by the PM rotors as the dynamometer speed was raised, but showed negligible reaction to the inclusion of the rotor circuit. A detailed analysis of the waveforms generated will be presented in the next Chapter.

### 3.1.1 Steady State Model: Operational Behavior

The behavior described above was expected and can be explained by comparing peak-flux densities due to the currents in the rotor winding and the magnets (remnant peak-flux density of $B_r = 1.3$ T for neodymium-iron-boron, NdFeB magnets) measured at the stator. However, a more interesting perspective can be found if one was to note that the interaction between the power rotor and the PM rotor is stronger than the interaction between the power rotor and the stator. To support this claim we can examine the same peak-flux densities described above, using the approximation B $\approx B_r \frac{t_m}{t_m+g}$. If the thickness of the magnets, $t_m \approx 22$ mm and the air-gap thickness between the power rotor and the PM rotor, $g \approx 20$ mm (due to mechanical engineering constraints the air-gap thickness of the prototype is now close to 40 mm), the flux density near the power rotor windings is $\approx$ 0.7 T. The peak flux density due to the stator windings is calculated using Ampere's Law thus: $\oint \mathbf{H}.\bar{dl} = 2g_s H_g$. Here $g_s$ is the effective air-gap between the power rotor face and the stator. The magnets are assumed to present a permeability of $\mu_o$ and $N_S I_s \leq 1000$, the stator limit. The peak-flux density as measured at the power rotor face due to the stator currents is given in Equation 3.1.

$$B_s = \frac{\mu_o N_s I_s}{2g_s} = 12.56 \text{ mT} \tag{3.1}$$

The underlying premise was that the stator currents have less effect on the power rotor windings than the permanent magnets thus allowing the separated machines model that follows.

Each power rotor in the generator system interacts with a PM rotor independent of the stator and can be considered as PM synchronous machines rotating at shaft speed. The difference frequency currents injected into the power rotor cause the PM rotor to run at a speed slightly higher than $\Omega_m$, the shaft speed. This speed is represented by $\frac{\omega_r}{p} + \Omega_m$ where $\omega_r$ is the rotor excitation frequency (the difference frequency) and $p$ is the number of pole pairs in the system. It can also be shown that the rotor power is a slip-fraction of the stator power, $P_r = sP_s$.

### 3.1.2 Dynamic Behavior

A generalized per-unit tenth order model which is presented with actual units in [19] is derived keeping the following key points in mind:
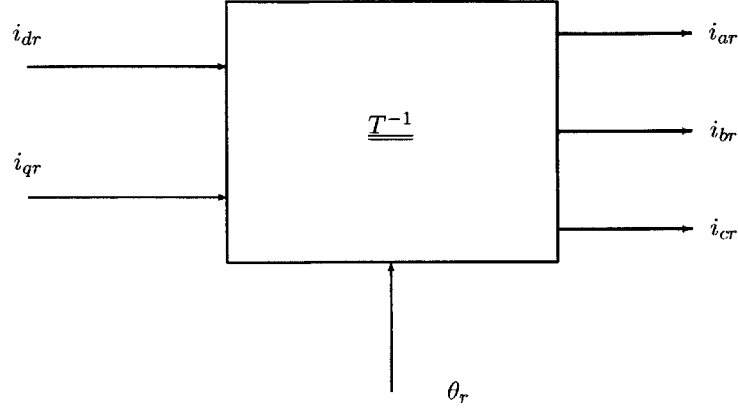
Figure 3.1: Inverse Park's Transform: The rotor per phase quantities can be obtained by reversing the Park's equations.

1. The model was developed using a d- and q- axis synchronous rotating frame representation. Since the d-q frame itself is rotating at a synchronous frequency, all sinusoidally modulated terms vanish after the transformation into this d-q frame. There are two separate PM machines which are integrated together as described in the steady state model. One is the machine model due to the interaction between the stator and the PM rotor (subscript 'S' used to describe this sub-model), and the other is due to the interaction between the power rotor and the PM rotor (subscript 'R' used to describe this sub-model).

2. The analysis will follow per-unit representation as expounded in [1]and [13]. The transformation of the armature winding variables to a coordinate system in which the rotor is stationary is implemented using Park's Transformation as shown in Equation 3.2. This effects a change of the frame of analysis from the standard 3-phase system to a set of quantities called the dq0 system (*direct, quadrature* and *zero-sequence*). For the purpose of our analysis we assume that there is no zero-sequence dynamics which is true if the 3-phase system is balanced.

$$
\begin{pmatrix} u_d \\ u_q \\ u_0 \end{pmatrix} = \underline{u}_{dq} = \underline{\underline{T}}\,\underline{u}_{ph} = \underline{\underline{T}} \begin{pmatrix} u_a \\ u_b \\ u_c \end{pmatrix}
\tag{3.2}
$$

Where $\underline{\underline{T}}$ and its inverse, $\underline{\underline{T}}^{-1}$ are given in Equations 3.3 and 3.4.

$$
\underline{\underline{T}} = \frac{2}{3} \begin{pmatrix} \cos\theta & \cos\left(\theta - \frac{2\pi}{3}\right) & \cos\left(\theta + \frac{2\pi}{3}\right) \\ -\sin\theta & -\sin\left(\theta - \frac{2\pi}{3}\right) & -\sin\left(\theta + \frac{2\pi}{3}\right) \\ \frac{1}{2} & \frac{1}{2} & \frac{1}{2} \end{pmatrix}
\tag{3.3}
$$

$$\underline{\underline{T}}^{-1} = \begin{pmatrix} \cos\theta & -\sin\theta & 1 \\ \cos\left(\theta - \frac{2\pi}{3}\right) & -\sin\left(\theta - \frac{2\pi}{3}\right) & 1 \\ \cos\left(\theta + \frac{2\pi}{3}\right) & -\sin\left(\theta + \frac{2\pi}{3}\right) & 1 \end{pmatrix} \tag{3.4}$$

The currents in the $d - q$ reference frame are constant provided the phase currents are balanced in nature. The angle $\theta$ above is defined in Equation 3.5 below.

$$\theta = \omega t + \theta_o \tag{3.5}$$

Notice how the equations can be reversed to perform an Inverse Park's Transformation to extract the phase variables if necessary from the dq0 variables.

3. The currents flowing into the machine are assumed to be positive and those flowing outward, negative. This is the standard notation used in dynamic models of electrical machines.

4. The d- axis winding is equivalent to one of the phase windings aligned with the field and the q- axis *leads* the field winding by 90°.

5. The two sub-models can driven by either currents or voltages depending on the driving system. In the set of equations to follow, the stator PM machine is voltage driven while the power rotor PM machine is current driven. The advantage of using a current driven system is a reduction in the order of the model by two.

In per-unit notation, the internal field flux of the PM rotor is defined as shown below:

$$\psi_0 = x_{ad} i_{f0} \tag{3.6}$$

Combining the voltage driven and current driven sub-models with the appropriate subscripts as discussed in point 1 above, we get a model that describes the overall behavior of the machine. The stator PM synchronous machine is described by Equations 3.7- 3.14.

Reduction of the model order is necessary in order to make computations less unwieldy and faster. MATLAB simulations require infinitesimally smaller time steps and fewer number of state variables to carry out the computations in each iteration faster and more accurately.

Moreover linearization of these equations will have to be carried out to examine stability issues using the eigenvalue analysis. A steady state situation is assumed as the initial condition for this analysis. However to obtain the perturbation analysis parameters, the steady state condition must first be simulated by considering the dynamic model below and using a time vector long enough for the disturbances in the system to die out.

$$\begin{pmatrix} i_{dS} \\ i_{kdS} \end{pmatrix} = \begin{pmatrix} x_{dS} & x_{adS} \\ x_{adS} & x_{kdS} \end{pmatrix}^{-1} \begin{pmatrix} \psi_{dS} - \psi_0 \\ \psi_{kdS} - \psi_0 \end{pmatrix} \tag{3.7}$$

$$\begin{pmatrix} i_{qS} \\ i_{kqS} \end{pmatrix} = \begin{pmatrix} x_{qS} & x_{aqS} \\ x_{aqS} & x_{kqS} \end{pmatrix}^{-1} \begin{pmatrix} \psi_{qS} \\ \psi_{kqS} \end{pmatrix} \tag{3.8}$$

The voltage driven simulation of the stator-PM rotor synchronous machine is defined by the 6$^{\text{th}}$ order model represented by the equations below. The stator is connected to a stiff voltage source at some point during the testing phase and hence is a voltage driven scheme.

$$\frac{d\psi_{dS}}{dt} = \omega_{0S}v_{dS} + \omega_S\psi_{qS} - \omega_{0S}r_{aS}i_{dS} \tag{3.9}$$

$$\frac{d\psi_{qS}}{dt} = \omega_{0S}v_{qS} - \omega_S\psi_{dS} - \omega_{0S}r_{aS}i_{qS} \tag{3.10}$$

$$\frac{d\psi_{kdS}}{dt} = -\omega_{0S}r_{kdS}i_{kdS} \tag{3.11}$$

$$\frac{d\psi_{kqS}}{dt} = -\omega_{0S}r_{kqS}i_{kqS} \tag{3.12}$$

$$\frac{d\omega_S}{dt} = \frac{\omega_{0S}}{2H_S}(\psi_{dS}i_{qS} - \psi_{qS}i_{dS} + T_{mS}) \tag{3.13}$$

$$\frac{d\delta_S}{dt} = \omega_S - \omega_{0S} \tag{3.14}$$

The following set of equations describe the PM synchronous machine represented by the power rotor - PM rotor interactions which are present on either side of the stator along the shaft. This machine is current driven, i.e., the $\lambda_d$, $\lambda_q$ and $\lambda_0$ in the state equations are replaced with $i_a$, $i_b$ and $i_c$. The d- and q- axis damper winding currents in the PM rotor due to the power rotor currents in per-unit notation are given by Equations 3.15 and 3.16.

$$i_{kdR} = \frac{1}{x_{kdR}}(\psi_{kdR} - x_{adR}i_{dR} - \psi_0) \tag{3.15}$$

$$i_{kqR} = \frac{1}{x_{kqR}}(\psi_{kqR} - x_{aqR}i_{qR}) \tag{3.16}$$

$$\frac{d\psi_{kdR}}{dt} = -\omega_{0R}r_{kdR}i_{kdR} \tag{3.17}$$

$$\frac{d\psi_{kqR}}{dt} = -\omega_{0R}r_{kqR}i_{kqR} \qquad (3.18)$$

However for the model that follows, to make manipulations easier, these damper currents and their state equations will be ignored for now. Since the power rotor is excited by a current source, this sub-model is described by the following $2^{\text{th}}$ order model:

$$\frac{d\omega_R}{dt} = \frac{\omega_{0R}}{2H_R}(\psi_{0R}i_{qR} + T_{mR}) - \frac{\omega_{0R}}{2H_{PR}}(T_{shaft} - T_e) \qquad (3.19)$$

$$\frac{d\delta_R}{dt} = \omega_R - \omega_{0R} \qquad (3.20)$$

In Equation 3.19, an additional term $\frac{\omega_{0R}}{2H_{PR}}(T_{shaft} - T_e)$ appears. The derivative $\frac{d\omega_R}{dt}$, is the acceleration of the PM magnet rotor in the reference frame of the rotating power rotor. Hence it is a resultant of the acceleration terms, $\omega'_R$ seen by a stationery machine and the term presented by the rotating shaft. The shaft torque term experiences an electromagnetic torque due to the currents in the power rotor in the opposite direction.

In Equation 3.19, a special quantity, $H_R$ is introduced, this inertia constant is defined thus, $\frac{\text{Rotational kinetic energy at rated speed}}{\text{Base Power}} = \frac{J\omega_0}{2pT_B}$, where $T_B$ is the base torque. Borrowing from the simulation ahead in this chapter, the effects of $H$ are shown in Figures 3.2 and 3.3.

The key advantage this model offers is the ease of interfacing with network variables. The rotating frame currents, $i_d$ and $i_q$, are extracted from the network phase variables using Equations 3.21 and 3.22 which follows from the Park's Transformation.

$$i_{dR} = i_{aR}cos(\theta) + i_{bR}cos(\theta - \frac{2\pi}{3}) + i_{cR}cos(\theta + \frac{2\pi}{3}) \qquad (3.21)$$

$$i_{qR} = -i_{aR}sin(\theta) - i_{bR}sin(\theta - \frac{2\pi}{3}) - i_{cR}sin(\theta + \frac{2\pi}{3}) \qquad (3.22)$$

$$\theta = \omega_R t + \delta_R \qquad (3.23)$$

Equation 3.23 is simply a restatement of Equation 3.5 with $\theta_o$ replaced by $\delta_R$. The quantities, $\omega_{0R}t$, $\omega_R t$ and $\delta_R$ are defined in electrical radians. Their mechanical equivalents are $\frac{\omega_{0R}}{p}t$, $\frac{\omega_R}{p}t$ and $\frac{\delta_R}{p}$ where $p$ is the number of pole pairs.

$R_{as}$ is the resistance between line-to-neutral, $R_{as}$ would be one half of the measured line-to-line resistance. For most PM based machines, skin effect is not significant and have also been reduced to a great extent by our choice of wire and hence its effects can be safely neglected.
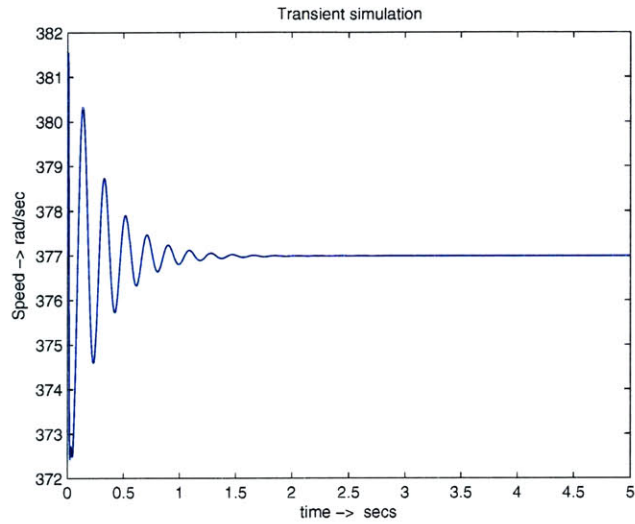
Figure 3.2: Effect of inertia constant on simulation of $\omega_m$. $H_m = 0.1$, the perturbations die after t $\approx$ 1.75 seconds.
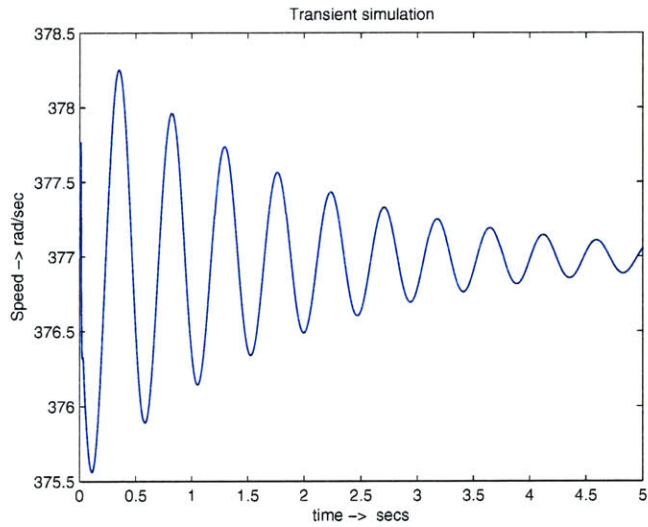


Figure 3.3: Effect of inertia constant on simulation of $\omega_m$. $H_m = 0.6$, the perturbations die after t $>$ 5 seconds.

Also winding resistance is temperature dependent, $R_t = \frac{R_o(K+T)}{(K+T_o)}$. Where K (a constant determined according to the material) = 234.5 for copper. $T_o$ is the base temperature in $^\circ C$ and $R_o$ is its corresponding resistence.

## 3.2 Further Development: A $5^{th}$ order model

Since the PM rotor is common to both components of the hybrid machine, $\psi_{0R} = \psi_{0S} = \psi_0$. The above model treats the hybrid machine as two completely different PM machines. It however fails on several fronts which will be enumerated later. To take the development of the model further a more contained description of the machine is necessary and is the subject of this section.

For the actual simulation $L_{sm}$, $L_{rm}$ and $L_{qm}$ among others have been estimated based on intuition. Determining the actual physical values of these quantities and their p.u. equivalents is not an easy task. To measure inductance, digital RLC meters or inductance bridges are often used. We have not been able to devise satisfactory tests similar to the Open Circuit Characteristics (OCC) test and the Short Circuit Characteristics (SCC) test that have been described in the following chapter.

These tests conducted on the prototype machine gives us an actual estimate of the synchronous impedance and can be cast into their d- and q- axis components. The hybrid machine has cylindrical rotors and and thus there are no or negligible effects due to saliency.

For completeness of literature, it is not out of place to mention briefly about saliency. The modelling of saliency is done by implementing the inductance in a dq-rotor oriented reference frame. The stator inductance is separated in two parts: the leakage inductance and the main inductance. The basis for most low and zero speed control issues is the presence of a difference in the d and q inductances. There are several sources of these differences in Permanent Magnet based machines; i.e., inherent rotor-based saliency, saturation saliency (at the yoke and/or teeth), harmonics due to rotor and stator teeth, saliency due to lamination direction, eddy current based saliency and finally saliency based on rotor eccentricity. As a result of these saliency effects, entire regions of the machine can be seen to have varying relative permeability values. For instance, the permanent magnet (in the rotor), the stator teeth (in the main flux path) and the stator yoke (also in the main flux path). The stator teeth areas are more saturated in comparison to regions of the stator yoke that is saturated.

A possible disadvantage of the slotless ring stator is the difficulty in constructing the armature winding, which must be bonded to the smooth 'bull-noses' of the stator iron. As described in 2.3, a relatively simple and effective gramme-ring winding technique was developed to overcome these challenges while constructing the winding in the prototype.

The notation used in this section is different from preceding sections. To begin with, flux linkage expressions are deployed thus as shown in Equations 3.24, 3.25 and 3.30:
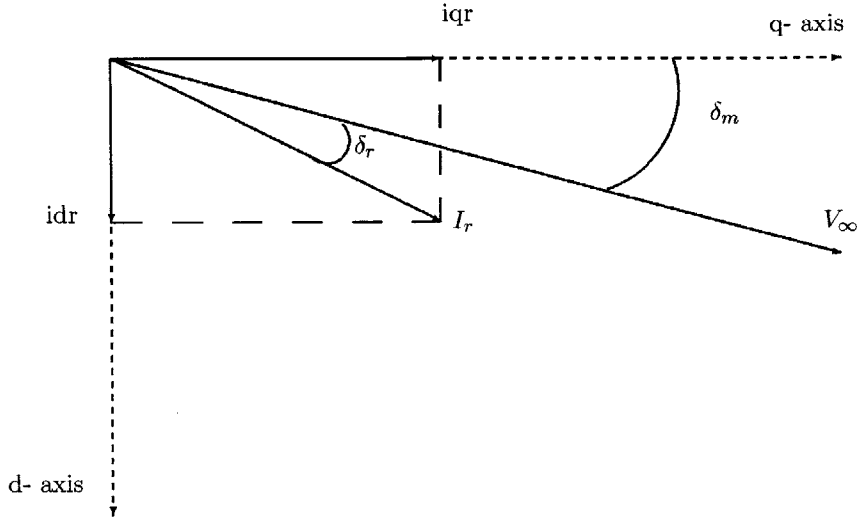
Figure 3.4: Phasor diagram: This rotating frame is on the PM rotor and has an angular speed of $\omega_m$

$$\lambda_{ds} = \lambda_0 + L_{ds}i_{ds} + Mi_{dr} \tag{3.24}$$

$$\lambda_{dr} = \lambda_o + Mi_{ds} + L_{dr}i_{dr} \tag{3.25}$$

In the above two Equations( 3.24 and 3.25) the 'known' variables are $\lambda_{ds}$ (which may also be referred to on occasion as $\lambda_d$ in other sections, dropping the 's' subscript) and $i_{dr}$ which is the controlled current injected into the system.

This current can be squirted anywhere in the rotor making the system less susceptible to the rotor dynamics. The current on the moving frame is a function of the angle $\delta_r$, that displaces the injected current from the frame of the infinite bus. This frame is itself displaced by an angle $\delta_m$ from the moving PM rotor frame. The phasor diagram is shown in Figure 3.4.

From the phasor diagram, Figure 3.4, it can be seen that:

$$V_d = V_\infty \sin \delta_m \tag{3.26}$$

$$V_q = V_\infty \cos \delta_m \tag{3.27}$$

Also,

$$i_{dr} = |I_r| \sin(\delta_m + \delta_r) \tag{3.28}$$

$$i_{qr} = |I_r| \cos(\delta_m + \delta_r) \tag{3.29}$$

$\delta_r$ is also a control term which, along with $I_r$, can be varied to select a point on the rotor where current is squirted into it.

Furthermore for the q- axis, we have:

$$\begin{pmatrix} \lambda_{qs} \\ \lambda_{qr} \\ \lambda_{qm} \end{pmatrix} = \begin{pmatrix} L_{qs} & M & L_{sm} \\ M & L_{qr} & L_{rm} \\ L_{sm} & L_{rm} & L_{qm} \end{pmatrix} \begin{pmatrix} i_{qs} \\ i_{qr} \\ i_{qm} \end{pmatrix} \tag{3.30}$$

In the above matrix equation, the 'known' quantities are $\lambda_{qs}$, $\lambda_{qm}$ and the controllable input current on the q- axis, $i_{qr}$.

With a little algebraic manipulation[1] Equation 3.30 can mauled to yield:

$$i_{qm} = \frac{L_{sm}(\lambda_{qs} - M i_{qr}) - L_{qs}(\lambda_{qm} - L_{rm} i_{qr})}{(L_{sm}^2 - L_{qs} L_{qm})} \tag{3.31}$$

$$i_{qs} = \frac{\lambda_{qs} - M i_{qr} - L_{sm} i_{qm}}{L_{qs}} \tag{3.32}$$

$$\lambda_{qr} = M i_{qs} + L_{qr} i_{qr} + L_{rm} i_{qm} \tag{3.33}$$

Now that we have established the basic framework, the state equations can be presented thus, Equations 3.34 $\sim$ 3.38.

$$\frac{d\lambda_{ds}}{dt} = V_{ds} + \omega_m \lambda_{qs} - r_{as} i_{ds} \tag{3.34}$$

$$\frac{d\lambda_{qs}}{dt} = V_{qs} - \omega_m \lambda_{ds} - r_{as} i_{qs} \tag{3.35}$$

$$\frac{d\lambda_{qm}}{dt} = -r_m i_{qm} \tag{3.36}$$

In Equation 3.36, $\lambda_{qm}$ is the flux induced in the PM rotor body due the current paths and is modeled as a damper winding here. The suffix '$m$' indicates that the quantity belongs to the magnet rotor.

The mechanical equations are more conveniently represented in p.u. notation as follows. The actual simulation is carried out using p.u. quantities.

---

[1]See Appendix B for derivation.

$$\frac{d\omega_m}{dt} = \frac{\omega_o}{2H_m}T_m \tag{3.37}$$

$T_s^e$     Electrial Torque due to the stator currents, per unit notation.

$T_r^e$     Electrial Torque due to the power rotor currents, per unit notation.

$$\frac{d\delta_m}{dt} = \omega_m - \omega_o \tag{3.38}$$

$T_s^e$ and $T_r^e$ are given by the following expressions. Note the negative sign in front of the expression for $T_r^e$. The torque acting on the PM rotor due to the power rotor tends to oppose the electrical drag torque from the stator.

$$T_s^e = \frac{3}{2}p(\lambda_{ds}i_{qs} - \lambda_{qs}i_{ds}) \tag{3.39}$$

$$T_r^e = -\frac{3}{2}p(\lambda_{dr}i_{qr} - \lambda_{qr}i_{dr}) \tag{3.40}$$

## 3.3   Simulation Results

The actual MATLAB Script is presented in the closing sections of this chapter. The simulation was carried out as follows. As mentioned before, for the actual simulation $L_{sm}$, $L_{rm}$ and $L_{qm}$ among others have been estimated based on intuition. Determining the actual physical values of these quantities and their p.u. equivalents values is not an easy task. Open Circuit Characteristics (OCC) and SCC (Short Circuit Characteristics) tests are performed to find the synchronous impedance (and after a DC test, the reactance as well).

Section 5.1 briefly examines generic OC and SC tests determine machine parameters and considers how they make be applied to our machine. These tests will have to be done at synchronous speeds which we have difficulty in reaching at the moment due to the structural stability of the test bed.

### 3.3.1   Simulation Methodology

The simulation of the $5^{th}$ order model presented above is not very complicated. An initial vector is defined as follows:

```
InitVector = [psids0 psiqs0 psiqm0 wm0 deltam0]
```

This vector is given the following initial value:

```
[psids0 psiqs0 psiqm0 wm0 deltam0] = [0 0 0 w0 0]
```

the MATLAB function 'ode23' is used to evaluate the state equations and return a vector, Vector. it accepts as arguments, Initvector and the subroutine, 'hybridver3function'.

Data is fed when the following screen appears:

```
Enter Simulation time vector length(secs) [o to tf]: 3
>>
```

The various simulation graphs are shown in the following figures.
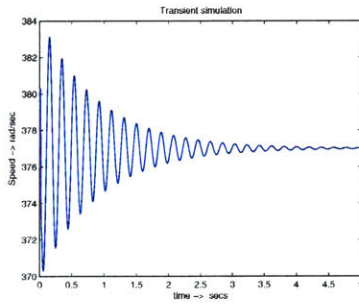


(a) $\omega_m$, Simulation time of 5 seconds.
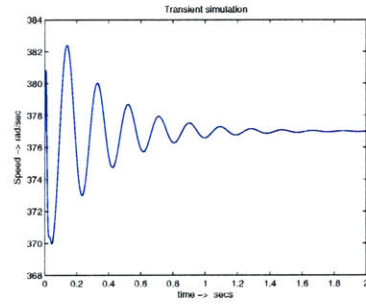
(b) $\omega_m$, Simulation time of 2 seconds.
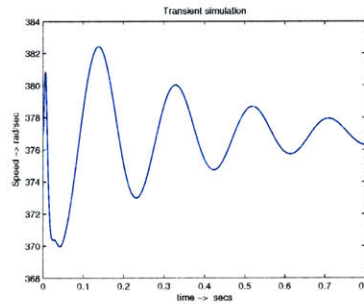
(c) $\omega_m$, Simulation time of 0.8 seconds.

Figure 3.5: These results were obtained by altering the time vector. Steady state condition of $\omega_o$ is reached after approximately 1.5 seconds with a value of $r_m \approx 0.7$ p.u.
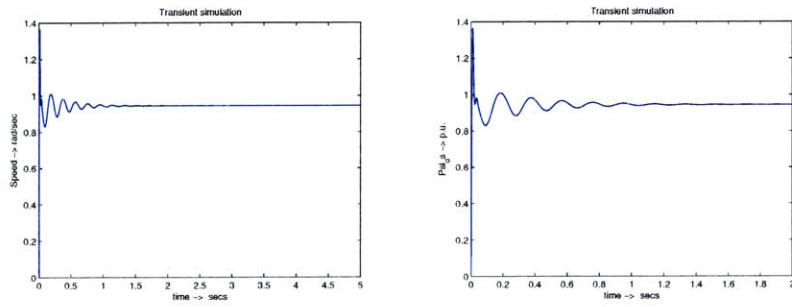
(a) $\psi_{ds}$, Simulation time of 5 seconds.

(b) $\psi_{ds}$, Simulation time of 2 seconds.
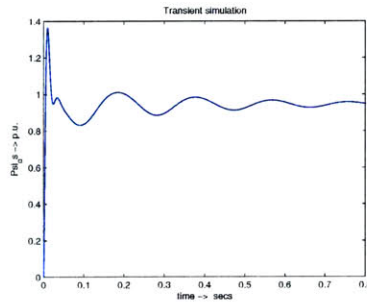
(c) $\psi_{ds}$, Simulation time of 0.8 seconds.

Figure 3.6: These results were also obtained by altering the time vector. Steady state condition of $\psi_{ds} \approx 0.87$ p.u. is reached after approximately 1.35 seconds with a value of $r_m \approx 0.7$ p.u.
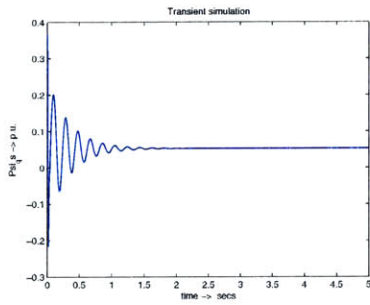
(a) $\psi_{qs}$, Simulation time of 5 seconds.
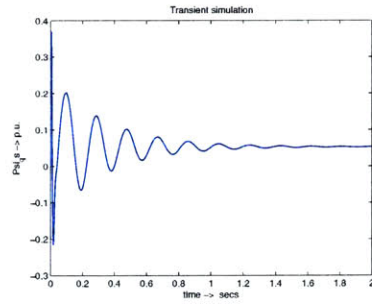


(b) $\psi_{qs}$, Simulation time of 2 seconds.
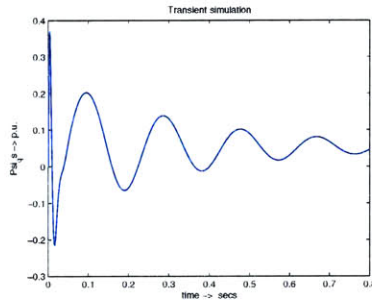


(c) $\psi_{qs}$, Simulation time of 0.8 seconds.

Figure 3.7: Steady state condition of $\psi_{qs} \approx 0.05$ p.u. is reached after approximately 1.35 seconds with a value of $r_m \approx 0.7$ p.u.
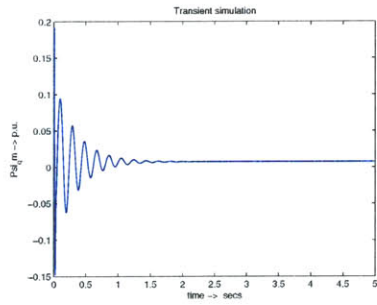
(a) $\psi_{qm}$, Simulation time of 5 seconds.
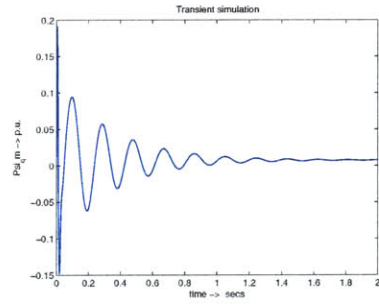


(b) $\psi_{qm}$, Simulation time of 2 seconds.
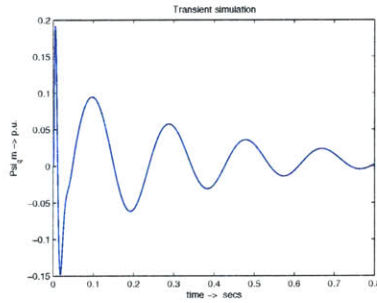


(c) $\psi_{qm}$, Simulation time of 0.8 seconds.

Figure 3.8: Steady state condition of $\psi_{qm} \approx 0.01$ p.u. is reached after approximately 1.4 seconds with a value of $r_m \approx 0.7$ p.u.

## 3.4 Interpreting the Results: Further Analysis

On this front, future work is expected to go along the lines of optimization and development of a linearized model of the hybrid machine. Eigenvalue analysis should then tell us more about the dynamic behavior of the PM rotor and is carried out in the next chapter. Several more tests on the prototype machine must be carried out to verify the results of the simulation. Moreover the quantities defined in the script will also have to be physically verified.

## 3.5 MATLAB Code: Hybrid machine simulation

### 3.5.1 Main file

```
% Hybrid Ver 3.0
% Simulation of our hybrid machine.
% Copyright Sivananda Reddy, MIT LEES.
% This code needs hybridvver3function.m

% needed parameters

% p.u. reactances (important note: Lakq, Lakd etc. are not
% necessary in this simplified picture as they are handled using the equal
% mutuals base system)                                                        10

% cleans up the workspace
clc
clear all


global xds xqs xdr xqr xm xsm xrm xqm Ir ras rm
global psi0 Vs w0 ws Hm Hshaft Tapplied deltar

xds = 1.5;    % no saliency, stator quantities                               20
xqs = 1.5;

xdr = 1.1;    % no saliency, rotor quantities
xqr = 1.1;

xm = 0.8;     % mutual reactance, see section on 'further development' for more details

% quantities associated with the PM rotor
```

```
xsm = 1.0;
xrm = 0.9;                                                                30
xqm = 0.8;
```

*% resistence values, best guesses.*
```
ras = 0.5;
rm = 0.2;   % the larger this value is the longer it taskes for the pertubations to die out.
```

```
Ir = 0.2;
deltar = 0.2;   % radians                                                 40
```

```
psi0 = 1.2;
Vs = 1.0;
w0 = 2*pi*60;
ws = 2*pi*7;
```

```
Hshaft = 0.4;
Hm = 0.1;
Tapplied = 0.7;
```
                                                                          50

*% [psids0 psiqs0 psiqm0 wm0 deltam0]*
```
initialVector = [0 0 0 w0 0];
tf = input('Enter Simulation time vector length(secs) [0 to tf]:');
time = [0 tf];
```

*% [t x] = ode23('currentdrivenmodelfunction', time, x0);*
```
[t Vector] = ode23('hybridVer3function', time, initialVector);
```

*% extracting quantities from the Vector.*                                 60
```
psids = Vector(:,1);
psiqs = Vector(:,2);
psiqm = Vector(:,3);
wm = Vector(:,4);
deltam = Vector(:,5);
```

*% present results*
*% figure(1)*
*% plot(t,wm)*                                                            70
*% title('Transient simulation');*
*% ylabel('Speed -> rad/sec');*

```
% xlabel('time ->  secs');

% figure(2)
% plot(t,psids)
% title('Transient simulation');
% ylabel('Psi_ds -> p.u.');
% xlabel('time ->  secs');
%                                                                    80
% figure(3)
% plot(t,psiqs)
% title('Transient simulation');
% ylabel('Psi_qs -> p.u.');
% xlabel('time ->  secs');
%
figure(4)
plot(t,psiqm)
title('Transient simulation');
ylabel('Psi_qm -> p.u.');                                           90
xlabel('time ->  secs');
%
```

### 3.5.2  Function file

*% Hybrid Ver 3.0 Function.*
*% Copyright Sivananda Reddy, MIT LEES.*
*% This function called by Hybrid Ver 3*

**function** dx = hybridVer2function(t, x)

**global** xds xqs xdr xqr xm xsm xrm xqm Ir ras rm                    10
**global** psi0 Vs w0 ws Hm Hshaft Tapplied deltar

*% electrical parameters*
psids = x(1);
psiqs = x(2);
psiqm = x(3);

*% mechanical parameters*
wm = x(4);
deltam = x(5);                                                         20


vds = Vs***sin**(deltam);
vqs = Vs***cos**(deltam);


idr = Ir***cos**(deltam − deltar);
ids = (psids − psi0)/xds − xm*idr/xds;

iqr = Ir***sin**(deltam − deltar);                                       30
iqm = (xsm*(psiqs − xm*iqr) − xqs*(psiqm − xrm*iqr))/(xsm^2 − xqs*xqm);
iqs = (psiqs − xm*iqr − xsm*iqm)/xqs;

psidr = psi0 + xm*ids + xdr*idr;
psiqr = xm*iqs + xqr*iqr + xrm*iqm;

*% w = (wshaft + ws);*

dpsids = w0*vds + wm*psiqs − w0*ras*ids;

                                                                      40

```
dpsiqs = w0*vqs - wm*psids - w0*ras*iqs;
dpsiqm =   -w0*rm*iqm;


Ts = psids*iqs-psiqs*ids;
Tr = -(psidr*iqr-psiqr*idr);


% torque on the magnet rotor
Tm = Ts - Tr;                                              50

dwm = (w0/(2*Hm))*(Tm);
ddeltam = wm - w0;

% dwshaft = (w0/(2*Hshaft))*(Tapplied - Tr);   % if wshaft is needed, these
% commented lines can be uncommented.


dx = [dpsids dpsiqs dpsiqm dwm ddeltam]';
                                                          60
```

# Linearization and Further Analysis

Until a few years ago, wind turbines were not expected to participate in voltage and frequency control and if a disturbance occurs, the wind turbines were immediately disconnected and reconnected when normal operation of the power system resumed. Thus in spite of the growing presence of wind turbines within power plants, frequency and voltage were maintained by controlling the large power plants as would have been the case without any wind farms present. This was possible, as long as wind power penetration in 3-phase power system grids was low.

However, due to the growing awareness and understanding of how a wind farm operates as well as the harmful effects of conventional energy sources among communities, there is a tendency for increased reliance on wind turbines for electrical power generation. Therefore, power system models need to be upgraded to account for the presence of these generation models; indeed they influence overall power system behavior, making it extremely difficult to run a network grid ignoring them.

This chapter presents a linearized model from the simulation equations developed in the previous chapter. Electrical machines and devices described by nonlinear differential equations, similar to Equations 3.34 - 3.38, will produce nonlinear responses. An equilibrium point is established for the system and is generally the point of maximum stability. For our purpose, linearization of the set of differential equations is done using the Taylor series expansion for a function in the following form:

$$f(x_o + \Delta x) = f(x_o) + \Delta x f(x_o) + \frac{1}{2!}(\Delta x)^2 f(x_o) + \dots \qquad (4.1)$$

For the purpose of this thesis (and most analysis in this domain of electrical machine dynamics), only the first two terms, $f(x_o)$ and $\Delta x f(x_o)$ are considered and the rest of the series is discarded as their contribution is insignificant.

## 4.1   Initial Pass: A Simple Linearized $5^{th}$ Order Model

To explore the swing model and the effects of damping at a given operating point, linearized analysis of the machine is necessary. The small signal model examines the dynamics for small deviations from the operating point. Armature resistance is generally small and a very little voltage drop exists across it. This information is useful while constructing a reduced

order model for the electromechanical transient behavior of the machine. A steady state operating point represented by the vector, $[\lambda_{dso}\ \lambda_{qso}\ \lambda_{qmo}\ \omega_{mo}\ \delta_{mo}]$ is defined and first order variations are setup from the state equations derived earlier. Using the expansion above, each of the state variables and quantities can be perturbed from its stable equilibrium position and represented as shown:

$$\left.\begin{array}{l} \lambda_{ds} = \lambda_{dso} + \widetilde{\lambda_{ds}} \\ \lambda_{qs} = \lambda_{qso} + \widetilde{\lambda_{qs}} \\ \lambda_{qm} = \lambda_{qmo} + \widetilde{\lambda_{qm}} \\ \omega_m = \omega_o + \widetilde{\omega_m} \\ \delta_m = \delta_{mo} + \widetilde{\delta_m} \end{array}\right\} \tag{4.2}$$

The '$\sim$' (*tilde*) in the expressions above indicate that the quantity is a disturbance term of the original and will henceforth be represented with an additional subscript, '1'.

Consider the d- axis voltage, $V_d$. It can be expressed in the following manner,

$$V_d = V\sin(\delta_m)$$

A perturbation in $\delta_m$ manifests as a disturbance in the dependent variable $V_d$ which can then be expressed in the form, $V_{do} + V_{d1}$ which directly follows from Equation 4.2 to give:

$$V_{do} + V_{d1} = V\sin(\delta_{mo} + \delta_{m1}) \tag{4.3}$$

Now Equation 4.1 can be applied to extract the first order term, ignoring the effects of the second and higher order terms.

$$V_{do} + V_{d1} = V\sin(\delta_{mo}) + V\cos(\delta_{mo})\delta_{m1}$$

$$V_{d1} = V\cos(\delta_{mo})\delta_{m1} \tag{4.4}$$

A similar conversion from the $V_{qs}$ in Chapter 3 to the $V_{qs1}$ required in the linearized model can be carried out for the q- axis voltage. It is presented in the following manner,

$$V_q = V\cos(\delta_m)$$

Again, a perturbation in $\delta_m$ appears in the form of a disturbance in the dependent variable $V_q$ which can then be expressed as, $V_{qo} + V_{q1}$ following from Equation 4.2:

$$V_{qo} + V_{q1} = V\cos(\delta_{mo} + \delta_{m1}) \tag{4.5}$$

Equation 4.1 is again applied to extract the first order term, ignoring the effects of the second and higher order terms as before.

$$V_{qo} + V_{q1} = V\cos(\delta_{mo}) - V\sin(\delta_{mo})\delta_{m1}$$

$$V_{q1} = -V\sin(\delta_{mo})\delta_{m1} \tag{4.6}$$

Consider Equation 3.34, the first of the equations that describe the model developed in the previous chapter. Applying linearization to it, the equations take on the form:

$$\frac{d\lambda_{dso}}{dt} + \frac{d\lambda_{ds1}}{dt} = V_{dso} + V_{ds1} + \omega_{mo}\lambda_{qso} + \omega_{mo}\lambda_{qs1} + \omega_{m1}\lambda_{qs1} + \omega_{m1}\lambda_{qso} - r_{as}i_{ds0} - r_{as}i_{ds1}$$

$$\frac{d\lambda_{ds1}}{dt} = V\cos(\delta_{mo})\delta_{m1} + \omega_{mo}\lambda_{qs1} + \omega_{m1}\lambda_{qso} - r_{as}i_{ds1} \tag{4.7}$$

Similarly the rest of the state equations can be expressed as Equations 4.8 ∼ 4.11.

$$\frac{d\lambda_{qs1}}{dt} = -V\sin(\delta_{mo})\delta_{m1} - \omega_{mo}\lambda_{ds1} + \omega_{m1}\lambda_{dso} - r_{as}i_{qs1} \tag{4.8}$$

$$\frac{d\lambda_{qm1}}{dt} = -r_m i_{qm1} \tag{4.9}$$

$$\frac{\omega_{m1}}{dt} = \frac{\omega_o}{2H}(T_{m1}) \tag{4.10}$$

$$\frac{\delta_{m1}}{dt} = \omega_{m1} \tag{4.11}$$

In Equation 4.10, $T_{m1}$ is given by,

$$T_{m1} = \frac{3}{2}p(\lambda_{dso}i_{qs1} + \lambda_{ds1}i_{qso} - \lambda_{qso}i_{ds1} - \lambda_{qs1}i_{dso} + \lambda_{dro}i_{qr1} + \lambda_{dr1}i_{qro} - \lambda_{qro}i_{dr1} + \lambda_{qr1}i_{dro})$$
$$\tag{4.12}$$

### 4.1.1 Simplifying Assumptions

Using the above linearized model ran into complications because it was difficult to come up with a set of linearized equations for the power rotor. As it stands now the dq- frame is a synchronously rotating frame fixed on the magnet rotor. Attempting to find the rotor voltages, $V_{dp}$ and $V_{qp}$ is not an easy task. One way of going about doing this is to consider the torque on the power rotor.

$$T_p = \frac{3}{2}p(\lambda_{qp}i_{dp} - \lambda_{dp}i_{qp}) \tag{4.13}$$

And using the following expression for power, $P_p$.

$$P_p = T_p\frac{1}{p}\omega_s \tag{4.14}$$

The reactive element of this power is given by

$$Q_p = \frac{3}{2}\omega_s(\lambda_{qp}i_{dp} + \lambda_{dp}i_{qp}) \tag{4.15}$$

The power rotor voltages on the dq- frame are then given by,

$$V_{dp} = -\omega_s\lambda_{qp}$$
$$V_{qp} = \omega_s\lambda_{dp}$$

A simplifying assumption would be to look at the power rotor as remaining in steady state and not subject to the perturbations described above. This is a reasonable assumption since the parameters to the power rotor, i.e. current and also shaft positioning are control variables.

In light of this assumption, The model reduces to the following set of equations, presented here in $p.u.$ notation as they are used in the MATLAB script appended to the end of this chapter.

$$\frac{d\psi_{ds1}}{dt} = \omega_o V\cos(\delta_{mo})\delta_{m1} + \omega_{mo}\psi_{qs1} + \omega_{m1}\psi_{qso} - \omega_o r_{as}i_{ds1} \tag{4.16}$$

$$\frac{d\psi_{qs1}}{dt} = -\omega_o V\sin(\delta_{mo})\delta_{m1} - \omega_{mo}\psi_{ds1} - \omega_{m1}\psi_{dso} - \omega_o r_{as}i_{qs1} \tag{4.17}$$

$$\frac{d\psi_{qm1}}{dt} = -\omega_o r_m i_{qm1} \tag{4.18}$$

$$\frac{\omega_{m1}}{dt} = \frac{\omega_o}{2H_m}(\psi_{dso}i_{qs1} + \psi_{ds1}i_{qso} - \psi_{qso}i_{ds1} - \psi_{qs1}i_{dso}) \tag{4.19}$$

$$\frac{\delta_{m1}}{dt} = \omega_{m1} \tag{4.20}$$

## 4.2 Stability: State Space Modeling

Starting from the most general form of a state space model which is described by the following equations:

$$\text{Input Vector} = \text{U(t)} = \begin{pmatrix} u_1(t) \\ u_2(t) \\ u_3(t) \\ u_4(t) \\ \vdots \\ u_m(t) \end{pmatrix} ; \text{State Vector} = \text{X(t)} = \begin{pmatrix} x_1(t) \\ x_2(t) \\ x_3(t) \\ x_4(t) \\ \vdots \\ x_n(t) \end{pmatrix} ;$$

$$\text{Output Vector} = \text{Y(t)} = \begin{pmatrix} y_1(t) \\ y_2(t) \\ y_3(t) \\ y_4(t) \\ \vdots \\ y_k(t) \end{pmatrix}$$

The state of a dynamic system is a minimal set of variables which are called state variables such that the knowledge of these variables at $t = t_o$ together with the knowledge of the input variables for a set of times, $t \geq t_o$, completely describes the behavior of the system for $t > t_o$. From Figure 4.1 several important facts about state space systems can be gleaned. The above information can be cast into the following forms. Equation 4.21 is called the state equation and Equation 4.22, the output equation.

$$\frac{dX(t)}{dt} = \underline{A}X(t) + \underline{B}U(t) \tag{4.21}$$

$$\frac{dY(t)}{dt} = \underline{C}Y(t) + \underline{D}U(t) \tag{4.22}$$
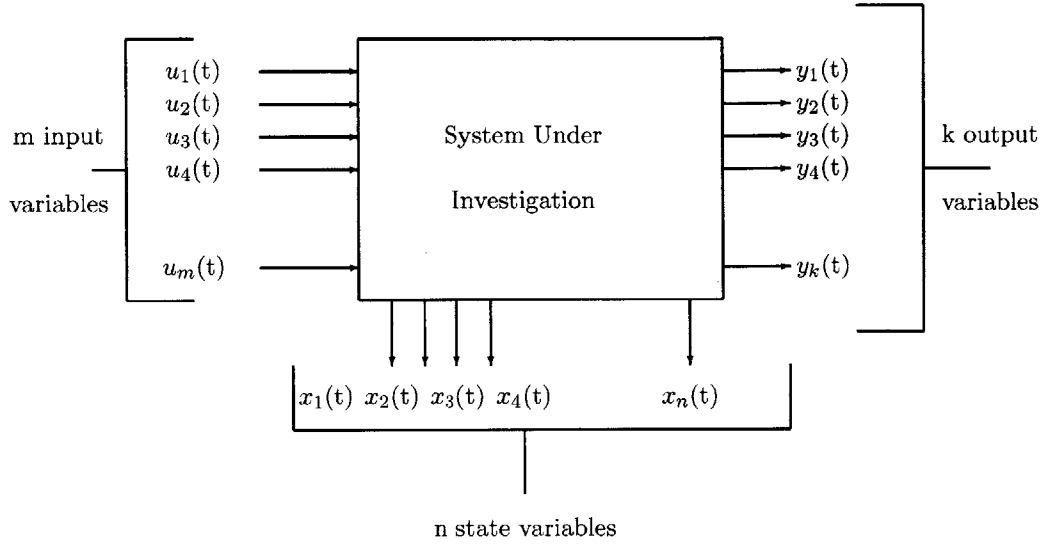
Figure 4.1: State Space depiction of an n- state, m- input, k- output system. This is the most general representation of a dynamic system.

Now Equations 4.16- 4.20 can be put in the form $\frac{dX}{dt} = \underline{A}X + \underline{B}U$ where only the term $\underline{A}X$ is of any interest to us.

Thus,

$$
\frac{d}{dt}\begin{pmatrix} \psi_{ds1} \\ \psi_{qs1} \\ \psi_{qm1} \\ \omega_{m1} \\ \delta_{m1} \end{pmatrix} = \begin{pmatrix} 0 & \omega_o & 0 & \psi_{qso} & \omega_o V \cos(\delta_{mo}) \\ -\omega_o & 0 & 0 & -\psi_{dso} & -\omega_o V \sin(\delta_{mo}) \\ 0 & 0 & 0 & 0 & 0 \\ i_{qso}\frac{\omega_o}{2H_m} & -i_{dso}\frac{\omega_o}{2H_m} & 0 & 0 & 0 \\ 0 & 0 & 0 & 1 & 0 \end{pmatrix}\begin{pmatrix} \psi_{ds1} \\ \psi_{qs1} \\ \psi_{qm1} \\ \omega_{m1} \\ \delta_{m1} \end{pmatrix} \quad (4.23)
$$

One may ask the question looking at the system matrix in Equation 4.23, where do we get $i_{qso}$ and $i_{dso}$ ? These are the equilibrium point values for the input variables to the system. At the close of Chapter 3 the simulations provided us with details of equilibrium values of the state variables. These values can be used to derive $i_{qso}$ and $i_{dso}$ and is done so in the MATLAB script.

### 4.2.1 Stability Analysis

The above model is a system of 5 first-order ODEs. The standard investigation technique for a set of equations given by $\frac{dX}{dt} = F(x)$ where x* is the stable point, such that, $F(x^*) = 0$ is to consider the behavior to a small perturbation as described above, $x(t) = x^* + \delta x(t)$. This yields, $F(x^* + dx) = F(x^*) + D_x F(x^*)dx +$ higher order terms which can be ignored ($D_x(x^*)$) denotes the Jacobian matrix of the partial derivatives of F).

The Jacobian is given by,

$$D_x F = \begin{pmatrix} \frac{\partial F^1}{\partial t^1} & \frac{\partial F^1}{\partial t^2} & \cdots & \frac{\partial F^1}{\partial t^N} \\ \frac{\partial F^2}{\partial t^1} & \frac{\partial F^2}{\partial t^2} & \cdots & \frac{\partial F^2}{\partial t^N} \\ \frac{\partial F^3}{\partial t^1} & \frac{\partial F^3}{\partial t^2} & \cdots & \frac{\partial F^3}{\partial t^N} \\ \frac{\partial F^4}{\partial t^1} & \frac{\partial F^4}{\partial t^2} & \cdots & \frac{\partial F^4}{\partial t^N} \\ \vdots & \vdots & \vdots & \vdots \\ \frac{\partial F^N}{\partial t^1} & \frac{\partial F^N}{\partial t^2} & \cdots & \frac{\partial F^N}{\partial t^N} \end{pmatrix} \qquad (4.24)$$

The eigenvalues of the Jacobian matrix given above equal the roots of the characteristic equation, if it were written out. Thus, if we had 5 state variables, we would have 5 eigenvalues, and if the magnitude of the largest eigenvalue was less than 1, then the equilibrium would be stable. Thus, only the Jacobian matrix needs to be known to evaluate the stability and is the reason why knowing $\underline{B}$ is not necessary. Most mathematical assistants will calculate eigenvalues (in MATLAB, the `eig` command performs the quick manipulation), as the math can become extremely messy. Therefore, for any number of state variables, the stability of any equilibrium can be found from the magnitude of the dominant eigenvalue of A, the Jacobian matrix.

Equation 4.24 is evaluated at $x(t) = x^*$. Non-trivial solutions for $\lambda$ to the Nth order characteristic polynomial, $det[D_x F - \lambda I] = 0$ yield a set of eigenvalues, $\lambda_1$, $\lambda_2$, $\lambda_3$ ...$\lambda_i$. The eigenvalues are also called the characteristic exponents and the real part of the eigenvalues determine the stability of the solution. Since $D_x F$ is a real matrix as shown above, the roots of the Nth order characteristic polynomial can either be real or else exist as complex conjugate pairs. If the real part of the characteristic exponents are positive the solutions are unstable and if they are negative the solutions are stable.

MATLAB code that evaluates the above derived matrix and also details the linearized model is presented in the next section.

## 4.3 MATLAB Code: Linearized Hybrid machine simulation

### 4.3.1 Main file

```
% Linear Hybrid Ver 1.0
% Simulation: Linearized hybrid machine model.
% Copyright Sivananda Reddy, MIT LEES.
% This code needs linearfunction.m

% needed parameters

% p.u. reactances (important note: Lakq, Lakd etc. are not
% necessary in this simplified picture as they are handled using the equal
% mutuals base system)                                                      10

% cleans up the workspace
clc
clear all


global xds xqs xdr xqr xm xsm xrm xqm Ir ras rm
global psi0 Vs ws Hm Hshaft Tapplied deltar
global psids0 psiqs0 psiqm0 w0 deltam0 iqs0 ids0
                                                                            20
xds = 1.5;   % no saliency, stator quantities
xqs = 1.5;


xdr = 1.1;   % no saliency, rotor quantities
xqr = 1.1;


xm = 0.8;   % mutual reactance, see section on 'further development' for more details

% quantities associated with the PM rotor
xsm = 1.0;                                                                  30
xrm = 0.9;
xqm = 0.8;


% resistence values, best guesses.
ras = 0.5;
rm = 1.1;   % the larger this value is the longer it takes for the pertubations to die out.
            % when rm = 1.2 or higher the system goes unstable.
```

```
Ir = 0.2;                                                           40
deltar = 0.2;   % radians

psi0 = 1.2;
Vs = 1.0;
w0 = 2*pi*60;
ws = 2*pi*7;

Hshaft = 0.4;
Hm = 0.1;
Tapplied = 0.7;                                                     50

% initial values imported from hybrid Ver 3.0
psids0 = 0.95;
psiqs0 = 0.055;
psiqm0 = 0.01;
deltam0 = -0.18;

% [psids0 psiqs0 psiqm0 wm0 deltam0]
initialVector = [psids0 psiqs0 psiqm0 w0 deltam0];
tf = input('Enter Simulation time vector length(secs) [0 to tf]:');  60
time = [0 tf];


options = odeset('RelTol',1e-1,'AbsTol',[1e-3 1e-4 1e-4 1e-5 1e-6]);
[t Vector] = ode113('linearfunction', time, initialVector,options);


% extracting quantities from the Vector.
psids1 = Vector(:,1);
psiqs1 = Vector(:,2);                                               70
psiqm1 = Vector(:,3);
wm1 = Vector(:,4);
deltam1 = Vector(:,5);


% present results

figure(1)
plot(t,wm1)
title('Transient simulation of perturbation');                     80
ylabel('Speed pertubation, \omega_1 -> rad/sec');
xlabel('time -> secs');
```

```
figure(2)
plot(t,deltam1)
title('Transient simulation of perturbation');
ylabel('Angle, \delta_1 -> rad/sec');
xlabel('time ->  secs');

figure(3)                                                              90
plot(t,psiqm1)
title('Transient simulation of perturbation');
ylabel('Psi_qm_1 -> p.u.');
xlabel('time ->  secs');

figure(4)
plot(t,psiqs1)
title('Transient simulation of perturbation');
ylabel('Psi_qs_1 -> p.u.');
xlabel('time ->  secs');                                               100

figure(5)
plot(t,psids1)
title('Transient simulation of perturbation');
ylabel('Psi_ds_1 -> p.u.');
xlabel('time ->  secs');


% construction of the system matrix. The derivation of these
% terms appears in the text.                                           110

c1 = -w0*ras / xds;

c2 = w0*Vs + ((w0*ras*xm*Ir*cos(deltar)) / xds);

c3 = ((w0*ras*(xsm^2)) / (xqs*((xsm^2) - xqm*xqs))) - (w0*ras / xqs);

c4 = (-w0*ras*xsm*xqs) / ((xqs*(xsm^2) - xqm*xqs));

c5 = (-w0*rm*xsm) / ((xsm^2) - xqm*xqs);                               120

c6 = (w0*rm*xqs) / ((xsm^2) - xqm*xqs);

c7 = (w0 /(2*Hm))*((1 / xqs) - ((w0*(xsm^2)) / ...
(xqs*((xsm^2) - xqm*xqs))) - (1 / xds) + (psi0 / xds));
```

```
c8 = (xsm*xqs) / (xqs*((xsm^2) − xqm*xqs));

B = [c1  w0  0  0  c2
     −w0  c3  c4  −1  0
      0  c5  c6  0  0
      0  c7  c8  0  0
      0  0  0  1  0]
lambda = eig(B)
```

                                                                                    130

*% end of main file.*

## 4.3.2   Function file

*% Linear Hybrid Ver 1.0 Function.*
*% Copyright Sivananda Reddy, MIT LEES.*
*% This function called by Linear Hybrid Ver 1.0*

**function** dx = linearfunction(t, x)

**global** xds xqs xdr xqr xm xsm xrm xqm Ir ras rm                                      10
**global** psi0 Vs ws Hm Hshaft Tapplied deltar
**global** psids0 psiqs0 psiqm0 w0 deltam0 ids0 iqs0

*% electrical parameters*
psids1 = x(1);
psiqs1 = x(2);
psiqm1 = x(3);

*% mechanical parameters*
wm1 = x(**4**);                                                                          20
deltam1 = x(**5**);

*% vds  =  Vs*sin(deltam);*
*% vqs  =  Vs*cos(deltam);*

idr1 = Ir***cos**(deltam1 + deltar);
ids1 = (psids1 − psi0)/xds − xm*idr1/xds;
                                                                                          30
idr0 = Ir***cos**(deltam0 + deltar);
ids0 = (psids0 − psi0)/xds − xm*idr0/xds;

iqr1 = Ir***sin**(deltam1 + deltar);
iqm1 = (xsm*(psiqs1 − xm*iqr1) − xqs*(psiqm1 − xrm*iqr1))/(xsm^2 − xqs*xqm);
iqs1 = (psiqs1 − xm*iqr1 − xsm*iqm1)/xqs;

iqr0 = Ir***sin**(deltam0 + deltar);
iqm0 = (xsm*(psiqs0 − xm*iqr0) − xqs*(psiqm0 − xrm*iqr0))/(xsm^2 − xqs*xqm);
iqs0 = (psiqs0 − xm*iqr0 − xsm*iqm0)/xqs;                                                  40

```
psidr1 = psi0 + xm*ids1 + xdr*idr1;
psiqr1 = xm*iqs1 + xqr*iqr1 + xrm*iqm1;


dpsids1 = w0*Vs*cos(deltam0)*deltam1 + w0*psiqs1 + wm1*psiqs0 - w0*ras*ids1;

dpsiqs1 = -w0*Vs*sin(deltam0)*deltam1 - w0*psids1 - wm1*psids0 - w0*ras*iqs1;
dpsiqm1 =  -w0*rm*iqm1;
```
50
```

Ts1 = psids0*iqs1 + psids1*iqs0 - psiqs0*ids1 - psiqs1*ids0;



% torque on the magnet rotor
Tm1 = Ts1;

dwm1 = (w0/(2*Hm))*(Tm1);
ddeltam1 = wm1;
```
60
```


dx = [dpsids1 dpsiqs1 dpsiqm1 dwm1 ddeltam1]';


% end of function file.
```

### 4.3.3   Eigenvalue Analysis: Examining the Inconsistency in Equation 4.23

Linearizing about the operation point, one arrives at a system matrix similar to Equation 4.23. The appended MATLAB script demonstrates the determination of its eigenvalues using an in-built function. A snippet of the output is shown below:

*%sample output*

Enter Simulation time vector **length**(secs) [0 to tf]:5

lambda =

 1.0e+02 *

 −0.0010 + 3.7702i
 −0.0010 − 3.7702i
  0.0010 + 0.2116i
  0.0010 − 0.2116i
      0

10

Consider -0.0010 $\pm$ 3.7702i, the two eigenvalues associated with $\pm\omega_0$ in Equation 4.23. We know that $\Re\{e^{i\theta}\}$ represents the euler equivalent of a signal. Where $\theta = \omega t$ and $\omega = 2\,\pi f$. Hence, $f \approx \frac{3.7702 \times 100}{2 \times \pi} \approx 60$ Hz. The more interesting information provided here however are the two unstable eigenvalues, $0.0010 \pm 0.2116$i, $f \approx\ = 21.16$ rad/sec or 3.37 Hz and damped at a rate associated with 0.0010, the real part.

The two $\approx +/-$ 377 j are the stator modes and are present because of the Park's transformation operation carried out earlier. This happens to be the basic rotational mode of the machine. The other complex pair should be the natural oscillation of the machine (swing mode). It is fast (22 radians/second is about 3.5 Hz possibly because the rotor is light. The zero frequency eigenvalue is related to the fact that rotor position is the integral of velocity in the above set of expressions. The swing mode is slightly unstable and we have seen that in machines before.

However, the two swing eigenvalues which are associated with the two mechanical degrees of freedom are complex, as one would expect. The final eigenvalue should then approximate the time constant of the damper. But here we have a zero eigenvalue, which can be associated with an integrator. The system matrix defined by Equation 4.23 indicates the '0' eigenvalue; indeed this suggests the existence of an integrator which is worrisome in this state-space analysis because integrators tend to contribute heavily to instability.

A second look pass at linearizing the state equation about its zero point is attempted in

the next section and this model successfully accounts for the behavior shown in chapter 3.

The eigenvalues also provide information about the equilibrium. As mentioned in Section 4.2.1 above, the roots to the characteristic equation can be real or imaginary numbers. If the roots (which are called eigenvalues) are real, then the system will move monotonically towards or away from the equilibrium point. If they are complex, and are imaginary numbers raised to a power, they are then are oscillatory over time. This is true because a complex number can be represented as $a + bi$ (after normalization in the case of electrical variables), which is basically a point in the complex plane with the coordinates $(a,b)$.

## 4.4 Linearized Model: Simulation Results

The actual MATLAB Script has been presented in the previous section on stability analysis. For academic interest the simulation of the linearized set of equations were also carried out. The simulation methodology is similar to that of the original system. Again, $L_{sm}$, $L_{rm}$ and $L_{qm}$ were estimated based on intuition. As has been pointed out before, determining the actual physical values of these quantities and their p.u. equivalents values is not an easy task.

### 4.4.1 Linearized Model: Simulation Methodology

The simulation of the $5^{th}$ order linearized model presented above is not very complicated. An initial vector is defined as follows:

```
InitVector = [psids0 psiqs0 psiqm0 wm0 deltam0]
```

This vector is given the following initial value:

```
[psids0 psiqs0 psiqm0 wm0 deltam0] = [0.87 0.05 0.01 w0 -0.18]
```

the MATLAB function 'ode45' is used to evaluate the state equations and return a vector, Vector. it accepts as arguments, Initvector and the subroutine, 'linearfunction'.

Data is fed when the following screen appears:

```
Enter Simulation time vector length(secs) [o to tf]: 3
>>
```

The various simulation graphs are shown in the following figures.
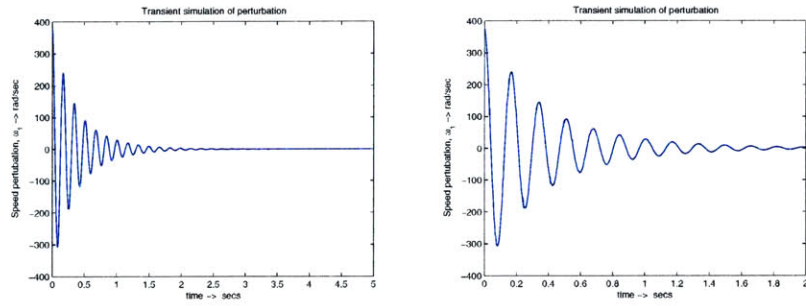
(a) Speed perturbation, $\omega_{m1}$, Simulation time of 5 seconds.

(b) $\omega_{m1}$, Simulation time of 2 seconds.
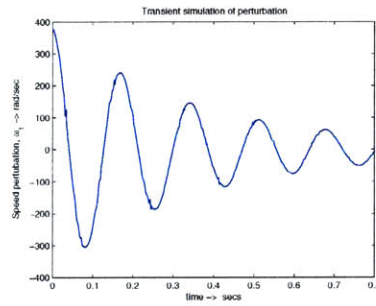


(c) $\omega_{m1}$, Simulation time of 0.8 seconds.

Figure 4.2: Linearized model simulation results: Perturbation of $\omega_{m1}$ dies to zero in a finite time.
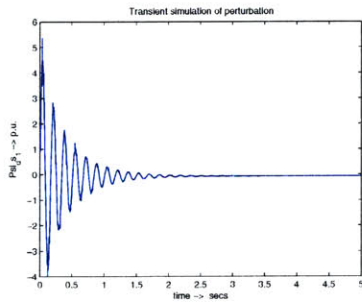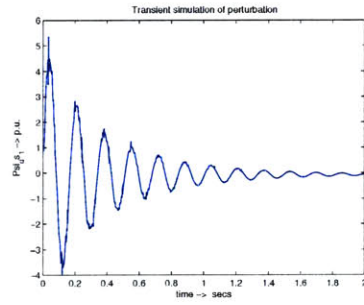
(a) $\psi_{ds1}$, Simulation time of 5 seconds.      (b) $\psi_{ds1}$, Simulation time of 2 seconds.
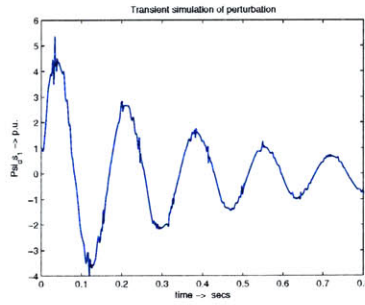


(c) $\psi_{ds1}$, Simulation time of 0.8 seconds.

Figure 4.3: Linearized model simulation results: Perturbation of $\psi_{ds1}$ dies to zero in a finite time.

(a) $\psi_{qs1}$, Simulation time of 5 seconds.



(b) $\psi_{qs1}$, Simulation time of 2 seconds.



(c) $\psi_{qs1}$, Simulation time of 0.8 seconds.
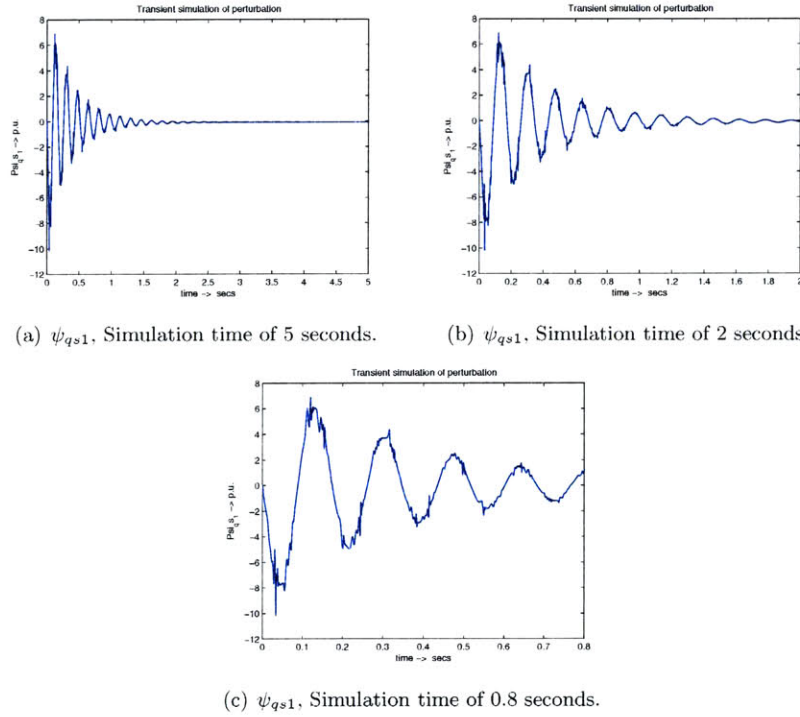
Figure 4.4: Linearized model simulation results: Perturbation of $\psi_{qs1}$ dies to zero in a finite time.
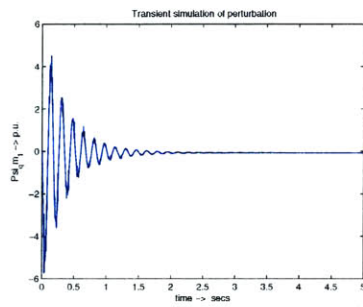
(a) $\psi_{qm1}$, Simulation time of 5 seconds.
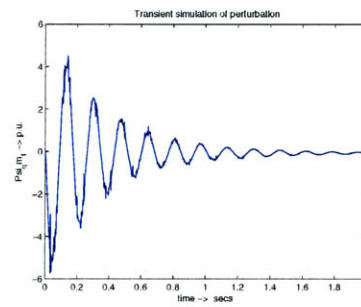


(b) $\psi_{qm1}$, Simulation time of 2 seconds.
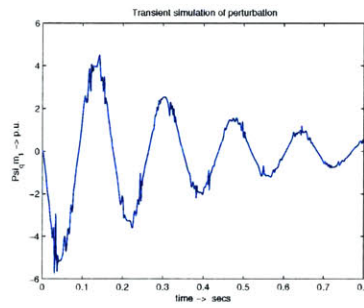


(c) $\psi_{qm1}$, Simulation time of 0.8 seconds.

Figure 4.5: Linearized model simulation results: Perturbation of $\psi_{qm1}$ dies to zero in a finite time.

(a) $\delta_{m1}$, Simulation time of 5 seconds.

(b) $\delta_{m1}$, Simulation time of 2 seconds.

(c) $\delta_{m1}$, Simulation time of 0.8 seconds.
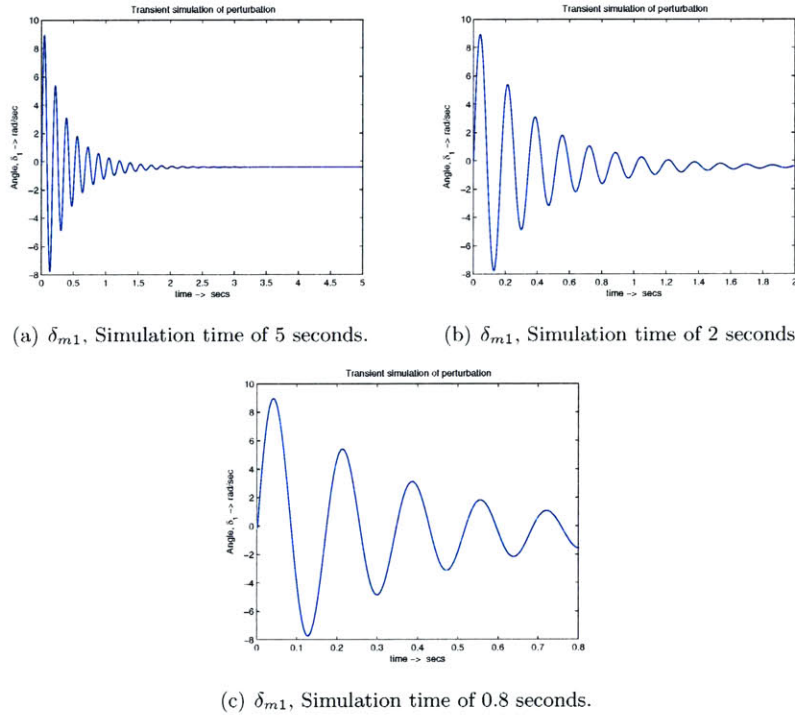
Figure 4.6: Linearized model simulation results: Perturbation of $\delta_{m1}$ dies to zero in a finite time.

## 4.5    Derivation: Full-Blown Model

So far we have from escaped actually carrying out the elaborate steps to finally arrive at a linearized state model. In this section a complete linearized $5^{th}$ order model is derived and cast into a system matrix for stability analysis about the zero point.

It is important to study the local behavior of the system in the neighborhood of the zero point, and the process to obtain the solutions of a set of linear differential equations is relatively straightforward. The local properties of the state space in the neighborhood of an equilibrium point can be studied by locally linearizing the differential equations at that point. Many techniques for the design and analysis of engineering systems zero in only on the local behavior, because in general the nominal operating point of any system is located at an equilibrium point, and if perturbations are small then the linear approximation gives a simple usable model of the dynamic system.

For convenience, we start by endeavoring to restate an altered form of the $5^{th}$ order model from Chapter here. The currents are first defined, Equations 4.28 - 4.30, followed by the state Equations 4.31 - 4.38.

Equation 3.24 and Equations 3.31 - 3.32 are reproduced here.

$$i_{qm} = \frac{L_{sm}(\lambda_{qs} - Mi_{qr}) - L_{qs}(\lambda_{qm} - L_{rm}i_{qr})}{(L_{sm}^2 - L_{qs}L_{qm})} \tag{4.25}$$

$$i_{qs} = \frac{\lambda_{qs} - Mi_{qr} - L_{sm}i_{qm}}{L_{qs}} \tag{4.26}$$

$$\lambda_{ds} = \lambda_0 + L_{ds}i_{ds} + Mi_{dr} \tag{4.27}$$

Equation 4.27 is recast to define $i_{ds}$ and these expressions are rewritten in the *p.u.* system, we get:

$$i_{ds} = \frac{\psi_{ds} - \psi_o}{x_{ds}} - \frac{x_m i_{dr}}{x_{ds}} \tag{4.28}$$

$$i_{qm} = \frac{x_{sm}(\psi_{qs} - x_m i_{qr}) - x_{qs}(\psi_{qm} - x_{rm}i_{qr})}{(x_{sm}^2 - x_{qs}x_{qm})} \tag{4.29}$$

$$i_{qs} = \frac{\psi_{qs} - x_m i_{qr} - x_{sm}i_{qm}}{x_{qs}} \tag{4.30}$$

To linearized the state space system, the above Equations 4.28 - 4.30 are substituted into the model below. Before that, the state space equations are defined in *p.u.* notation as

well. Rotor torque perturbations are ignored for the moment and thus appears merely as $T_r$ here.

$$\frac{d\psi_{ds}}{dt} = \omega_o V_s \sin \delta_m + \omega_m \psi_{qs} - \omega_o r_{as} i_{ds} \tag{4.31}$$

$$\frac{d\psi_{qs}}{dt} = \omega_o V_s \sin \delta_m - \omega_m \psi_{ds} - \omega_o r_{as} i_{qs} \tag{4.32}$$

$$\frac{d\psi_{qm}}{dt} = -\omega_o r_m i_{qm} \tag{4.33}$$

$$\frac{d\delta_m}{dt} = \omega_m - \omega_o \tag{4.34}$$

$$\frac{d\omega_m}{dt} = \frac{\omega_o}{2H} T_m \tag{4.35}$$

$$T_m = T_s^e - T_r \tag{4.36}$$

$$T_s^e = (\psi_{ds} i_{qs} - \psi_{qs} i_{ds}) \tag{4.37}$$

$$T_r^e = -(\psi_{dr} i_{qr} - \psi_{qr} i_{dr}) = T_r. \tag{4.38}$$

Since we are linearizing about the zero point, the equilibrium vector can be defined as follows, $[\ \psi_{dso}\ \ \psi_{qso}\ \ \psi_{qmo}\ \ \omega_{mo}\ \ \delta_o\ ] = [\ 1\ 0\ 0\ \omega_o\ 0\ ]$. To facilitate the substitutions, the following expressions are evaluated:

$$-\omega_o r_{as} i_{ds} = \frac{-\omega_o r_{as}\psi_{ds}}{x_d s} + \frac{\omega_o r_{as}\psi_o}{x_d s} + \frac{\omega_o r_{as}x_m}{x_d s}i_{dr} \tag{4.39}$$

$$-\omega_o r_m i_{qm} = \frac{-\omega_o r_m x_{sm}}{x_{sm}^2 - x_{qm}x_{qs}}\psi_{qs} + \frac{\omega_o r_m x_{sm}x_m}{x_{sm}^2 - x_{qm}x_{qs}}i_{qr} + \frac{\omega_o r_m x_{qs}}{x_{sm}^2 - x_{qm}x_{qs}}\psi_{qm}\cdots$$
$$\cdots - \frac{\omega_o r_m x_{qs}x_{rm}}{x_{sm}^2 - x_{qm}x_{qs}}i_{qr} \tag{4.40}$$

$$-\omega_o r_{as} i_{qs} = \frac{-\omega_o r_{as}\psi_{qs}}{x_{qs}} + \frac{\omega_o r_{as}x_m}{x_{qs}}i_{qr} + \frac{\omega_o r_{as}x_{sm}}{x_{qs}}i_{qm} \tag{4.41}$$

In Equation 4.41, the term $\frac{\omega_o r_{as} x_{sm}}{x_{qs}} i_{qm}$ can be further evaluated using Equation 4.29.

$$\frac{\omega_o r_{as} x_{sm}}{x_{qs}} i_{qm} = \frac{\omega_o r_{as} x_{sm}^2}{x_{qs}(x_{sm}^2 - x_{qm} x_{qs})} \psi_{qs} - \frac{\omega_o r_{as} x_{sm}^2 x_m}{x_{qs}(x_{sm}^2 - x_{qm} x_{qs})} i_{qr} \cdots$$

$$\cdots - \frac{\omega_o r_{as} x_{sm} x_{qs}}{x_{qs}(x_{sm}^2 - x_{qm} x_{qs})} \psi_{qm} + \frac{\omega_o r_{as} x_{sm} x_{qs} x_{rm}}{x_{qs}(x_{sm}^2 - x_{qm} x_{qs})} i_{qr} \qquad (4.42)$$

Now for the evaluation of the torque cross terms. This can get extremely messy, so only the final expressions are presented here:

$$\psi_{ds} i_{qs} = \frac{\psi_{ds} \psi_{qs}}{x_{qs}} - \frac{x_m i_{qr} \psi_{ds}}{x_{qs}} - \frac{x_{sm} i_{qm} \psi_{ds}}{x_{qs}} \qquad (4.43)$$

Again, the term $\frac{x_{sm} i_{qm} \psi_{ds}}{x_{qs}}$ can be replaced by the following expression using Equation 4.29 once more.

$$-\frac{x_{sm} i_{qm} \psi_{ds}}{x_{qs}} = -\frac{x_{sm}^2 \psi_{qs} \psi_{ds}}{x_{qs}(x_{sm}^2 - x_{qm} x_{qs})} + \frac{x_{sm}^2 x_m i_{qr} \psi_{ds}}{x_{qs}(x_{sm}^2 - x_{qm} x_{qs})} + \cdots$$

$$\cdots \frac{x_{sm} x_{qs} \psi_{qm} \psi_{ds}}{x_{qs}(x_{sm}^2 - x_{qm} x_{qs})} - \frac{x_{qs} x_{sm} x_{rm} i_{qr} \psi_{ds}}{x_{qs}(x_{sm}^2 - x_{qm} x_{qs})} \qquad (4.44)$$

The other cross term, $-\psi_{qs} i_{ds}$ can also be evaluated and is given by,

$$-\psi_{qs} i_{ds} = -\frac{\psi_{qs} \psi_{ds}}{x_{ds}} + \frac{\psi_o \psi_{ds}}{x_{ds}} + \frac{x_m i_{dr} \psi_{qs}}{x_{ds}} \qquad (4.45)$$

In Equation 4.45, the product $i_{dr} \psi_{qs}$ contains perturbable terms and can be expressed as follows. Equation 4.46 is composed of two terms. The term, $I_r \cos \delta_r \delta_{m1} \psi_{qs1}$ is a product of two perturbation terms and hence is a small quantity.

$$i_{dr} \psi_{qs} = I_r \sin(\delta_{mo} + \delta_{m1} + \delta_r)(\psi_{sqo} + \psi_{qs1})$$

$$= I_r \cos \delta_r \delta_{m1} \psi_{qso} + I_r \cos \delta_r \delta_{m1} \psi_{qs1} \qquad (4.46)$$

The rotor current components, $i_{dr}$ and $i_{qr}$, occur several times in the above equations. To deal with them the following simplification is done which is a treatment similar to the stator voltage quantities in Equations 4.4 and 4.6. Thus, $i_{dr} = I_r \sin(\delta_m + \delta_r)$ and $i_{qr} = I_r \cos(\delta_m + \delta_r)$ can be rewritten as, $I_r \cos \delta_{mo} \delta_{m1}$ and $I_r \sin \delta_{mo} \delta_{m1}$.

### 4.5.1 Final Restatement: Full-Blown Linearized Model

Using the above set of Equations 4.39 - 4.46 and the state-space model presented above, the linearized model can be derived and is presented here. A couple of assumptions were made while reducing the equations above to the linearized form below. the most important of them is the assumption that $\sin \delta_r \approx 0$, since $delta_r$ is a small quantity, and likewise if need be it can also be assumed that $\cos \delta_r \approx 1$.

$$\frac{d\psi_{ds1}}{dt} = \omega_o V_s \delta_m + \omega_o \psi_{qs1} - \frac{\omega_o r_{as} \psi_{ds1}}{x_{ds}} + \frac{\omega_o r_{as} x_m}{x_{ds}} I_r \cos \delta_r \delta_m \qquad (4.47)$$

$$\frac{d\psi_{qs1}}{dt} = -\omega_{m1} \psi_{do} - \omega_o \psi_{ds1} - \frac{\omega_o r_{as} \psi_{qs1}}{x_{qs}} + \frac{\omega_o r_{as} x_{sm}^2}{x_{qs}(x_{sm}^2 - x_{qm} x_{qs})} \psi_{qs1} \cdots$$

$$\cdots - \frac{\omega_o r_{as} x_{sm} x_{qs}}{x_{qs}(x_{sm}^2 - x_{qm} x_{qs})} \psi_{qm1} \qquad (4.48)$$

$$\frac{d\psi_{qm1}}{dt} = -\frac{\omega_o r_m x_{sm}}{x_{sm}^2 - x_{qm} x_{qs}} \psi_{qs1} + \frac{\omega_o r_m x_{qs}}{x_{sm}^2 - x_{qm} x_{qs}} \psi_{qm1} \qquad (4.49)$$

And the torque related state equations are give below. The torque acting on the PM rotor due to the power rotor tends to oppose the electrical drag torque from the stator. This term is shown as $T_r$ above, but disappears in the linearized model as it is assumed constant for this purpose.

$$\frac{d\omega_{m1}}{dt} = \frac{\omega_o}{2H} \left[ \frac{\psi_{qs1}}{x_{qs}} - \frac{x_{sm}^2 \psi_{qs1}}{x_{qs}(x_{sm}^2 - x_{qm} x_{qs})} - \frac{\psi_{qs1}}{x_{ds}} + \frac{\psi_o}{x_{ds}} \psi_{qs1} + \frac{x_{sm} x_{qs}}{x_{qs}(x_{sm}^2 - x_{qm} x_{qs})} \psi_{qm1} \right]$$
$$(4.50)$$

$$\frac{d\delta_{m1}}{dt} = \omega_{m1} \qquad (4.51)$$

The script to implement the system matrix derived from the above set of equations has been appended to an earlier section in this chapter.

The new system matrix takes on the form shown in Equation 4.53. Of course this follows from $\frac{dX}{dt} = \underline{A}X + \underline{B}U$ where again only the term $\underline{A}X$ is of any interest to us.

$$\underline{\underline{A}} = \begin{pmatrix} -\frac{\omega_o r_{as}}{x_{ds}} & \omega_o & 0 & 0 & \omega_o V_s + \left(\frac{\omega_o r_{as}}{x_{ds}} I_r \cos\delta_r\right) \\[2ex] -\omega_o & \left[\frac{\omega_o r_{as} x_{sm}^2}{x_{qs}(x_{sm}^2 - x_{qm}x_{qs})} - \frac{\omega_o r_{as}}{x_{qs}}\right] & -\left[\frac{\omega_o r_{as} x_{sm} x_{qs}}{x_{qs}(x_{sm}^2 - x_{qm}x_{qs})}\right] & -1 & 0 \\[2ex] 0 & -\left[\frac{\omega_o r_m x_{sm}}{x_{sm}^2 - x_{qm}x_{qs}}\right] & \left[\frac{\omega_o r_m x_{qs}}{x_{sm}^2 - x_{qm}x_{qs}}\right] & 0 & 0 \\[2ex] 0 & \begin{aligned}\frac{\omega_o}{2H}\Big\{\frac{1}{x_{qs}} &- \left[\frac{x_{sm}^2}{x_{qs}(x_{sm}^2 - x_{qm}x_{qs})}\right]\dots \\ \dots &- \frac{1}{x_{ds}} + \frac{\psi_o}{x_{ds}}\Big\}\end{aligned} & \left[\frac{x_{sm}x_{qs}}{x_{qs}(x_{sm}^2 - x_{qm}x_{qs})}\right] & 0 & 0 \\[2ex] 0 & 0 & 0 & 1 & 0 \end{pmatrix}$$

$$(4.52)$$

The matrix $\underline{\underline{A}}$ above finds a place in the following equation as shown. This thus represents the linearized system matrix derived around the zero point of the system.

$$\frac{d}{dt}\begin{pmatrix} \psi_{ds1} \\ \psi_{qs1} \\ \psi_{qm1} \\ \omega_{m1} \\ \delta_{m1} \end{pmatrix} = \underline{\underline{A}}\begin{pmatrix} \psi_{ds1} \\ \psi_{qs1} \\ \psi_{qm1} \\ \omega_{m1} \\ \delta_{m1} \end{pmatrix} \qquad (4.53)$$

### 4.5.2 Output Sample: Interpretation

*%sample output*

Enter Simulation time vector **length**(secs) [0 to tf]:5

lambda =

  1.0e+03 *

  −0.0260 + 0.3771i
  −0.0260 − 0.3771i

10

$$-0.4361 + 0.6100i$$
$$-0.4361 - 0.6100i$$
$$-0.5210$$

Now consider -0.0260 ± 0.3771i, the two eigenvalues associated with $\pm\omega_0$ in Equation 4.23. We know that $\Re\{e^{i\theta}\}$ represents the euler equivalent of a signal. Where $\theta = \omega t$ and $\omega = 2\pi f$. Hence, $f \approx \frac{0.3771 \times 1000}{2 \times \pi} \approx 60$ Hz.

The fact that all eigenvalues have negative real parts indicate that the system is stable. However as we will demonstrate in the next section, it is possible to drive the system into instability by altering the resistance of the PM rotor damper circuit.

The magnitude of a complex eigenvalue is denoted by r on the polar plane, and if this value is less than 1, then the system will show damped oscillations towards equilibrium, and if they are greater than 1, the system will show oscillations with increasing amplitude away from equilibrium. For the special case where r=1, there will be stable oscillations around the equilibrium. Hence, the dominant eigenvalue provides information on whether the system will return to an equilibrium following a perturbation and also informs up whether it moves towards or away from an equilibrium monotonically.

## 4.6   Damper Circuit Resistance: 'Critical Point'

Returning to the simulation of Chapter 3, if $r_m$ on line 35 of the main code was altered, the waveforms change drastically. This is understandable as altering the damper circuit resistance results in a pronounced change in the time taken for the perturbations to die out as indicated in the comment (lines 35-36 of the code). However for a particular value $r_m \approx$ 1.35 $p.u.$ the system goes unstable.

This behavior is demonstrated in the following Figures 4.7 and 4.11.

Several techniques can be used to increase machine stability such as the addition of amortisseur windings[2]. Now, if the stator magnetic field rotates at a speed of $N_s$ and varies with the speed variations of the PM rotor which also remains at the same speed, then no voltage will be induced in the amortisseur circuits. However interaction of the magnetic field produced by the windings when there is a speed disparity and the magnetic field from the stator produces a torque which alters the stability profile of the system. In fact, it is not necessary to have a physical set of windings, but the rotor bodies can be modeled as damper circuits which result in the increase of state-space order.
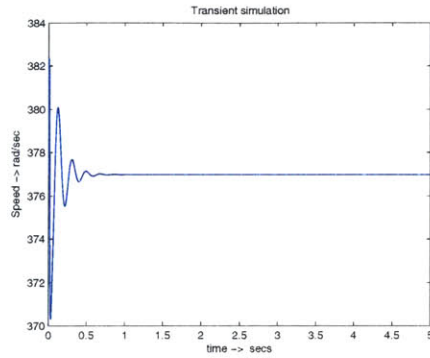
(a) $r_m$=0.2 $p.u.$ The perturbation dies out after 0.65 seconds. This indicates good stability.
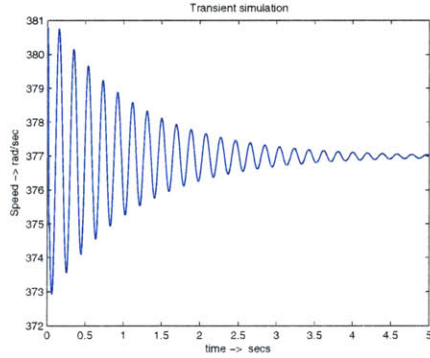


(b) $r_m$=0.5 $p.u.$ The perturbation takes longer (t > 5 seconds) to die out, but does go away eventually.
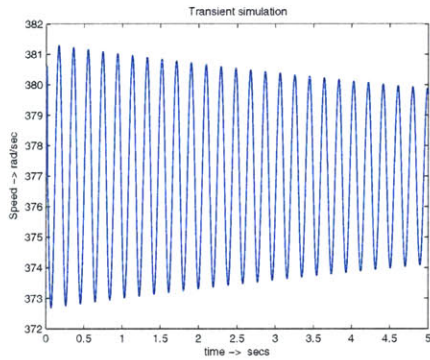


(c) $r_m$=1.1 $p.u.$ The perturbation stays around for a long time (t > 15 seconds). The outer envelope suggests that it does die out eventually.

Figure 4.7: Stable linearized model simulation results: Perturbation of $w_m$ dies to zero in a finite time for different values of $r_m < 1.3$ $p.u.$

Figure 4.8: Near critical point, $r_m = 1.3\ p.u.$: The perturbations appear to remain constant as indicated by the outer envelope in this graph of t $\leq$ 5 seconds.
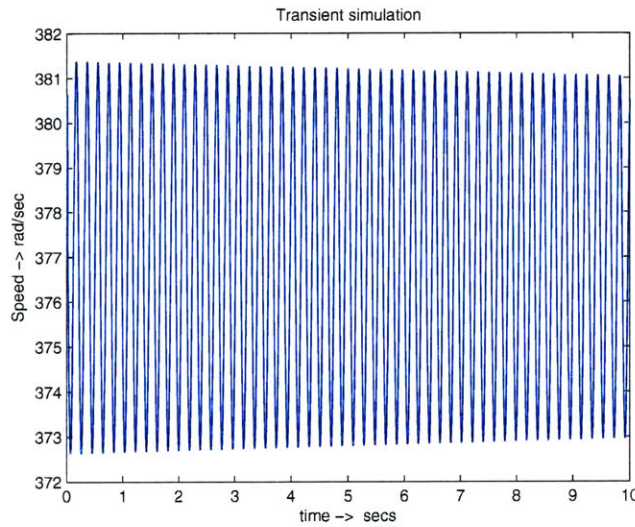


Figure 4.9: Near critical point, $r_m = 1.3\ p.u.$: The perturbations now clearly seem to be dying out in this graph of t *leq* 10 seconds.
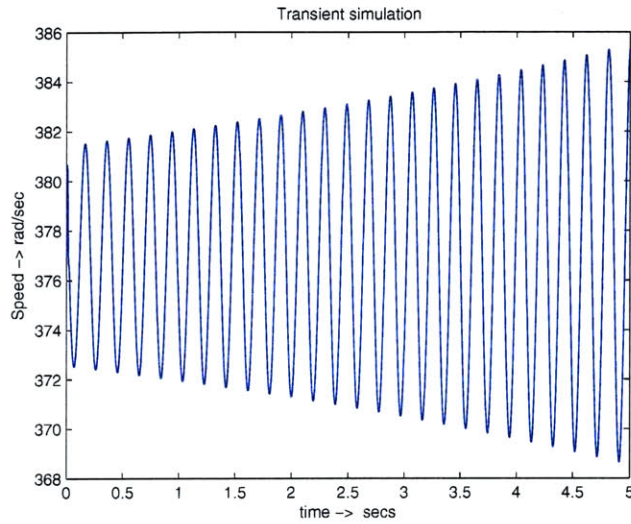
Figure 4.10: beyond critical point, $r_m = 1.5$ $p.u.$: The perturbations increase in amplitude indicating an unstable system, $r_m > 1.35$ $p.u.$
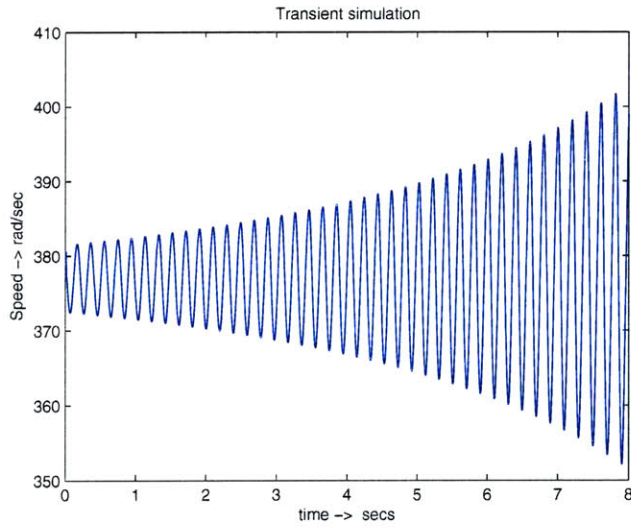


Figure 4.11: Far beyond critical point, $r_m = 1.7$ $p.u.$: Pertubations continue to increase in amplitude as the system goes unstable, $r_m \gg 1.35$ $p.u.$

# *Preliminary Tests: Acquisition of Initial Data*

The prototype hybrid machine was subjected to a few initial tests after it was mounted on the test-bed. Chapter 2 had expounded on the design and construction of the hybrid generator. A description of the test bed setup is given in Chapter 6 which also endeavors to describe the components external to the generator itself. Moreover the test circuits are briefly described to give an idea of how the results presented in this chapter were obtained.

## 5.1 Generic OC, SC and DC tests for alternators

Open circuit tests are performed to obtain the open circuit characteristics (OCC) of three-phase alternators. OCC is a curve showing the variation of open circuit terminal voltage, $V_t$ (or $E_g$) with field current, $I_f$ when the machine is running at synchronous speed. The values of $V_t$ for incremental changes in $I_f$ are recorded till the magnetic circuit shows saturation effects and the OCC is plotted. Since the power rotor in our prototype is located far from the stator on account of the presence of the magnet rotors in their midst, the effect of 10 $\sim$ 15 A of current is small; but with well defined field strength to air-gap ratio one can expect better results.

Short circuit test is performed to obtain the short circuit characteristics (SCC). It is the variation of the armature current, $I_a$ with the field current, $I_f$ when the machine is running at synchronous speed and the external windings are shorted. We had to take care that rated $I_a$ was not exceeded at anytime during the test. The alternator is driven at the synchronous speed and $I_a$ for incremental changes in $I_f$ were recorded. The SCC in regular alternators is a straight line as compared to the OCC(no magnetic saturation).

The synchronous impedance is then thus obtained from the results of these tests using the relation given in Equation 5.1 where $Z_s$ is the synchronous impedance per phase.

$$Z_s = \frac{V_{os}}{I_{sa}} \tag{5.1}$$

$V_{os}$ Rated voltage at field current, $I_f$.

$I_{sa}$ Short circuit armature current at $I_f$ corresponding to rated voltage $V_{os}$ on the OCC test.

The effective AC resistance $R_s$ is calculated to obtain the synchronous reactance $X_s = \sqrt{Z_s^2 - R_s^2}$. The DC resistance of the armature winding is simply obtained by using the ammetervoltmeter method. The effective AC resistance is then taken to be 1.6 times the DC resistance to include the effects of the temperature rise and the skin effect caused by the 60 Hz (and harmonics) alternating current during running condition.

## 5.2   Initial runs

The above tests described for alternators are not immediately applicable to our prototype machine. To be able to run the hybrid generator all the way to its synchronous speed, the dynamometer speed must be $\approx$ 1080 rpm. This presents a new challenge in terms of structural test bed stability. A few low speed tests however were carried out and the waveforms generated by the stator terminals are presented here.

At the time of writing this thesis, only low speed tests (machine speed of 120-160 rpm, dynamometer speeds of 360-400 rpm.) could be performed on the machine. The PM rotors and the power rotors appeared to be out of balance but that possibility was ruled out after several vibration tests were carried out. A mechanical shifting motion that occurs once per revolution of the main shaft as the the PM rotor assembly readjusts itself against the magnetic stress, caused presumably by the angular contact bearings not nested flatly against the surface of the permanent magnet rotor was yet to be resolved. The entire PM assembly would suddenly shift during the revolution and this motion significantly alters the air-gap profile on either side of the PM rotor.

A description of the internal structure of the main shaft (and the floating shaft) assembly has been presented in Chapter 2, Section 2.4.

### 5.2.1   Stator Voltage Waveforms

One of the first tests carried out on the assembled machine was to examine the response of the stator voltage to injected DC into the power rotors. With minimal current injection, the magnet rotor coupled to the driveshaft and when rotated at a relatively low speed, it spun with the power rotor. A fourier analysis on the voltage waveform indicated that all time harmonics were insignificant and well within the range of the noise generated by the experimental setup ($\approx$ 1V). The measurements were taken with the help of an oscilloscope and the data transferred to MATLAB for analysis.

A comparison of the measured waveform with a sine wave curve fit by superimposing the waves was carried out and the waveforms in Figure 5.1 were obtained.
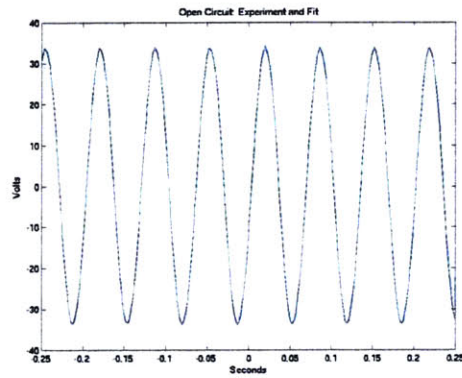
(a) Sine wave open circuit output: Sine wave fit.
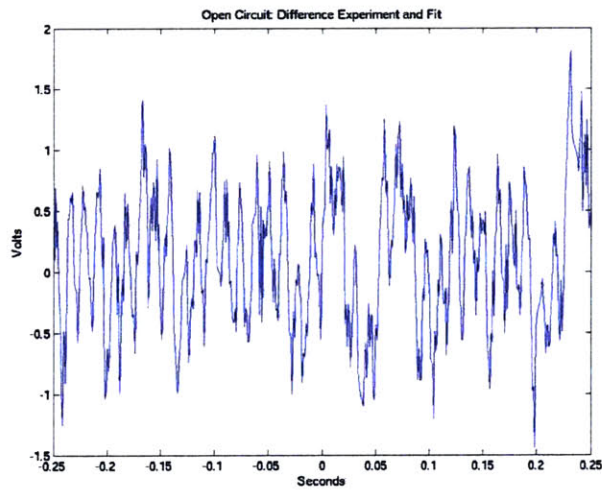


(b) Sine wave open circuit output: Difference fit.

Figure 5.1: Stator Open Circuit Waveforms: A sine fit and difference fit that indicates a near perfect sine output. (*Adapted from the Tenth Quarterly Report.*)

| Rotor Voltage V V (DC) | Power Rotor Current (DC) | Induced Volts/Hz (Peak) | RMS Voltage at 60 Hz |
|---|---|---|---|
| 13 | 5 | 2.221 | 94.247 |
| 30 | 10 | 2.228 | 94.553 |
| 41.5 | 15 | 2.235 | 94.822 |
| 48.7 | 20 | 2.500 | 95.112 |

Table 5.1: Power Rotor Current: RMS Open-circuit voltage seen at the stator leads.

The sine wave 'curve fit' was carried out to demonstrate that the open circuit waveform was very close to a sine wave. A fourier analysis of the data indicated no significant harmonics level beyond experimental noise levels. Notice from the difference curve fit, the maximum peak values do not exceed $\approx 1.75$ V. This is indeed acceptable given the noisy equipment and mechanical conditions we are dealing with.

The DC voltage injected into the power rotor was done in accordance to Table 5.1. The voltage waveforms were taken with a range of current in the power rotor. The effect of the power rotor current on the variations in the open circuit waveforms is barely noticeable. This is an indication of the strength of the magnetic field produced by the magnet rotors while 'drowns' out the variations in in power rotor current.

The induced open circuit voltage hovers about the 94V mark which falls short of the expected value. This can be attributed to large airgaps in the machine due to manufacturing constraints.

An adaptation from the *Tenth Quarterly report* appears here that describes the mechanical constraints mentioned above.

"...[The low voltage] is most likely due to the larger than designed air-gap, which is in turn due to the alignment and bearing difficulties we have encountered. This is a minor issue in view of the mechanical problems described below: we have the facilities required to synchronize the machine at arbitrary voltage.

An attempt was made to measure short circuit current, which would have allowed us to estimate synchronous reactance of the machine. As it turns out this measurement did not work out. We could not put enough current in the power rotor to entrain the
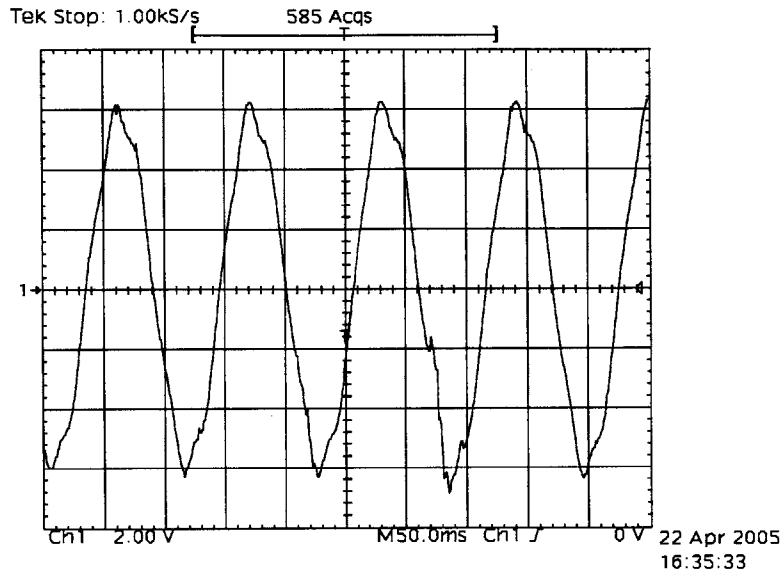
Figure 5.2: Rotor waveform: Image produced by oscilloscope with 20A DC injected into stator winding and external drive running at 150 rpm (machine speed ≈ 55 rpm.)

permanent magnet rotor. The shorted stator of the machine acted like an induction motor to produce a large retarding torque on the permanent magnet rotor, which turned at a speed substantially less than that of the power rotor...

...[We have been unsuccessful, to date] to turn the rotor at a speed faster than about half of rated, because of vibrations of the complete motor system. The rails on which the machine is mounted are somewhat flexible, leading to a vertical motion as the rotor is sped up. We have not, so far, attempted to drive the machine through what appears to be a critical speed at roughly half speed. Stiffening up the mounting system by fixing the outer end to the concrete floor was not successful. The motion of the machine had enough force to pull the screws out of the floor..."

## 5.3 Rotor Waveforms

The rotor waveforms were obtained by reversing the setup described in the previous section. Figure 5.2 shows the waveform captured on the oscilloscope for 20A of current and the driveshaft rotating at 55 rpm. The glitch on the waveform is presumably caused by the wobble of the PM rotor assembly which is covered in detail in Section 7.4.3.
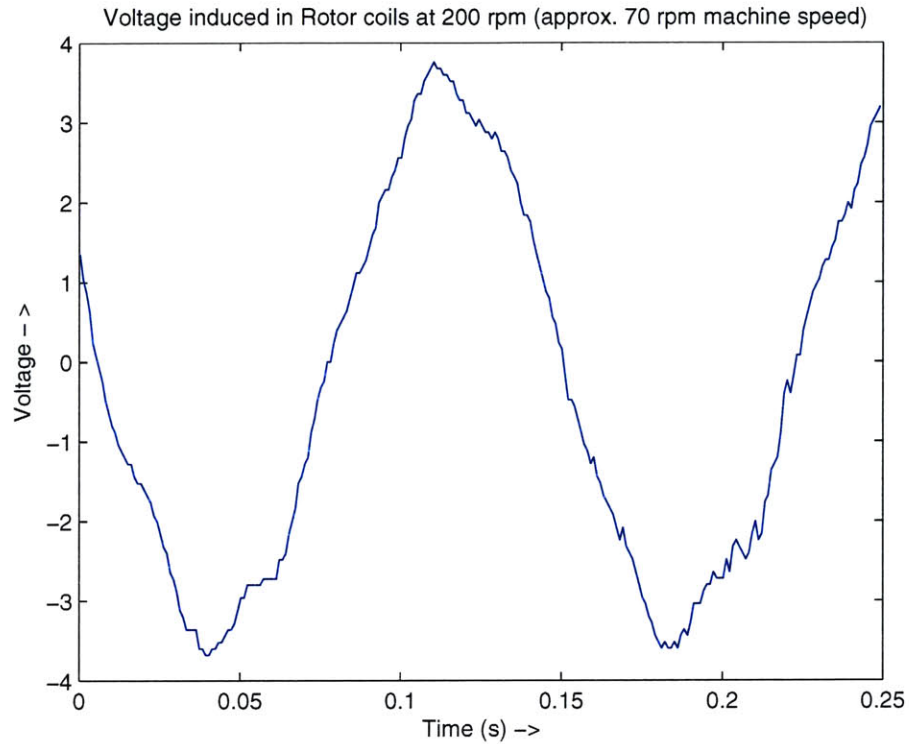
Figure 5.3: Rotor waveforms: MATLAB interpretation of rotor waveform with 20A DC injected into stator winding and external drive running at 200 rpm (machine speed $\approx$ 65 rpm.)

Using MATLAB to plot the other curves obtained from the oscilloscope at different speeds while keeping the current constant, Figures 5.3 and 5.4 were obtained.

Again the voltage value falls below the expected mark and this is probably due to the large air gaps in the machine. At different speeds the effect of the current injected in the power rotor is not seen to have an significant influence. A superimposition of the two waveforms is presented in Figure 5.5 and provides an insight into the relative magnitudes as the speed increases. The phase shift component is not accurately displayed because these images are oscilloscope snapshots.
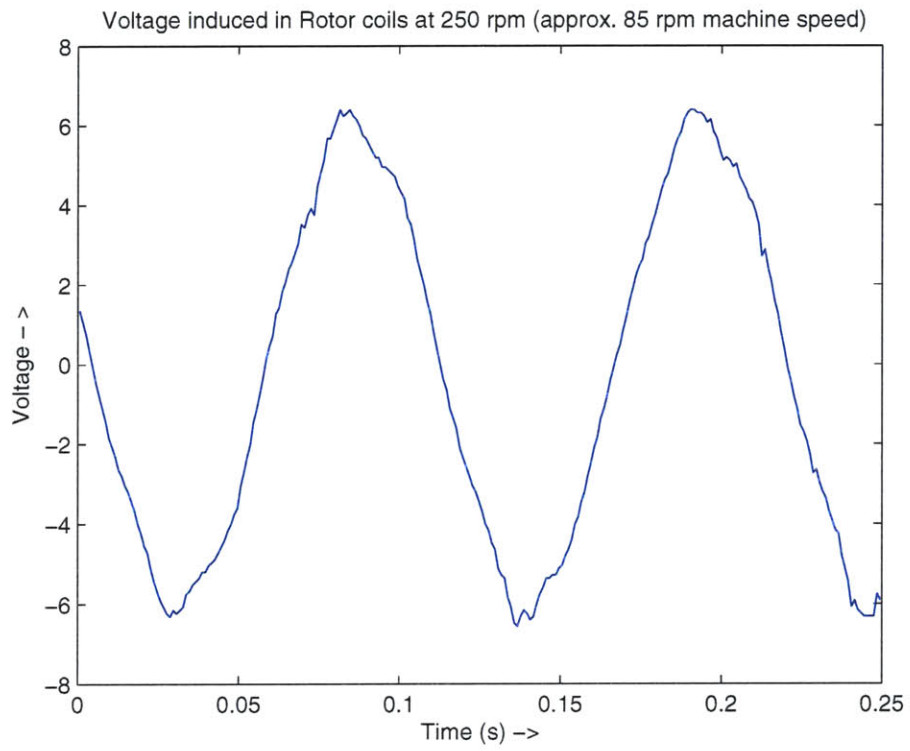
Figure 5.4: Rotor waveform: MATLAB interpretation of rotor waveform with 20A DC injected into stator winding and external drive running at 250 rpm (machine speed $\approx$ 80 rpm.)
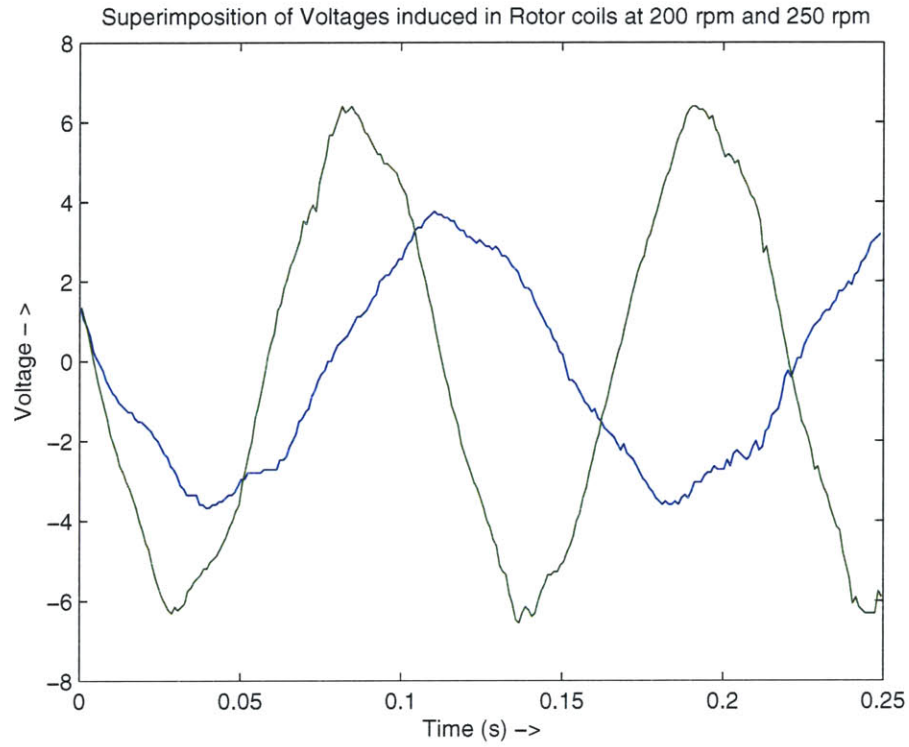
Figure 5.5: Rotor waveform: Superimposed waveforms to provide an insight into the relative magnitudes of the rotor voltage as the speed increases from 200 rpm (lower magnitude voltage) to 250 rpm (higher magnitude voltage). The phase shift component is not accurately displayed as these are oscilloscope snapshots.

## 5.4   Controller and Power Electronics Scheme

If the hybrid machine were to run as a variable speed motor, a variable frequency drive (VFD) that controls the rotor speed using a microcontroller is used. A variable speed drive generates variable frequency (from the inverter under the control of a microcontroller) to vary the speed of the motor. It is known that in such applications the base speed of the motor is proportional to the supply frequency and inversely proportional to the number of stator poles which remains a fixed number and cannot be changed. The supply frequency can be altered instead, changing the equivalent impedance of the circuit as seen by the machine and increasing of reducing the current drawn by the system.

Adapting from the Microchip document AN889 titled, 'VF Control of 3-Phase Induction Motors Using PIC16f7X7 Microcontrollers', A three phase inverter bridge has been built out of power electronic components capable of handling upto 20 A current and an operating frequency, variable between 7 Hz and 25 Hz. Details of the construction will be presented in a later document by Pilawa, the graduate student working on it.

Microchip PIC16F7X7's features are summarized below:

Special Microcontroller Features - File-Safe Clock Monitor - Power-On Reset - Power-up Timer (PWRT) and Oscillator Start-Up Timer (OST).

Peripheral Features - Two 8-bit timer/counter with Prescalar - One 16-bit timer/counter - High source/sink current: 25mA - Master Synchroonous Serial Port (MSSP) - Parallel Slave Port (PSP): 40/44 pin-device only.

Low Features - Primary Run(XT, RC, Oscillator, 76 A, 1MHz, 2V) - RC_RUN (7A, 31.25kHz, 2V) - Timer1 Oscillator (1.8 A, 32kHz, 2V).

Analog Features - 10-bit, up to 14-channel Analog-to-Digital Converter - Dual Analog Comparators - Programmable Low-Voltage Detect (LVD).

Oscillators - Three Crysal modes: LP, XT, HS (up to 20 MHz) - Two External RC modes - ECIO (up to 20 MHz) - 8 user-selectable frequencies.

A pin diagram of the PIC16F7X7 appears in the appendix, Figures A.5 and A.6.

## 5.5   Blocked Power Rotor Test: Injecting 3-$\Phi$ Low Frequency Current

This test was marred with several difficulties as the carbon brushes kept losing contact with the slip rings at random orientations of the driveshaft. The current in each phase was hence not equal and intermittent destroying the credibility of the test results.

With the power rotor engaged and held by the drive mechanism, and a current of around 10A injected into the power electronics assembly, the magnet rotor rotated haltingly forward. On occasion, it would oscillate and travel ahead at a low frequency possibly due to poor brush contacts. An increase in the excitation frequency caused a corresponding increase in the frequency of oscillations by the PM rotor.

However at one point several complete revolutions were observed for an excitation frequency close to 20 Hz. As expected, the rpm increased with an increase in the frequency of the excitation signal produced by a signal generator and fed to the power electronics assembly.

Before any further testing can be done on the machine, the wobble in the PM rotor assembly must be rectified and the slip ring contacts made more reliable.

*Chapter 6*

# Test Bed Setup: External Components and Configuration

---

This chapter describes briefly the configuration of the dynamometer used to run the hybrid machine and also presents overview of alternative arrangements. Results for each experiment performed using the setup presented in this chapter are given in Chapter 5.

The dynamometer is mounted on a T-slot base plate which is also used to provide stability to the whole mounting arrangement of the hybrid machine. A pair of rails are affixed to the T-Slots in the base plate and are approximately 62" inches apart. The next section expounds further on this and relevant portions from an earlier thesis work listed as [21] can be referred to for additional details on the hardware.

## 6.1 Dynamometer Description

The base plate that accommodates the dynamometer weighed approximately 1500 lbs premachining and has four T-slots about 6 inches apart. 1/2" - 13 threaded bolts and nuts were used to fix the rails into the T-slots.

A flexible shaft coupling connects the rotor side on the dynamometer shaft to the torquemeter thus providing a tolerance mechanism for planar and angular offsets. The load motor is a 20 HP Kollmorgen permanent magnet synchronous machine. This motor is controlled by a VECTORSTAR inverter[1] and power supply. The setup is wired in accordance to a schematic shown in the manual.

Detailed description of this hardware including a dimensioned picture is presented in Chapter 4 of [21].

## 6.2 Testbed Setup

The housing of the machine must be fastened securely to the test-bed. The method of attachment was to secure two $4\frac{1}{2}$" iron plates on either end-plate near the bottom with a hole large enough to pass an iron rod that would behave as the pivot point of the machine.

---

[1]Donated to LEES by the Kollmorgen Corporation for an earlier research project.
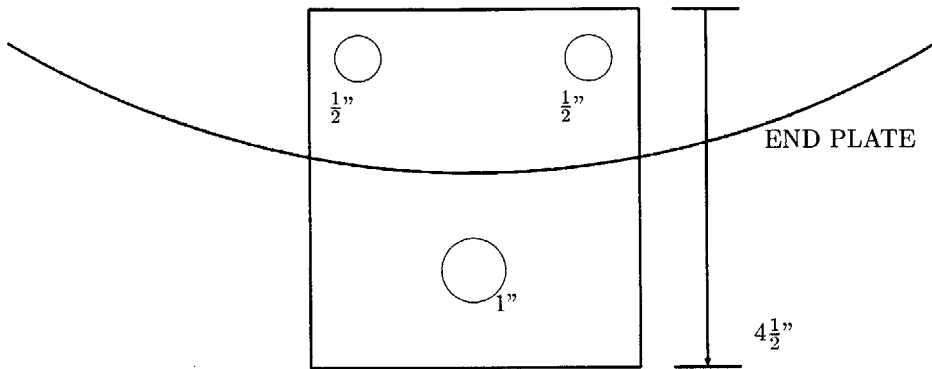
Figure 6.1: Iron Plate fastened to either end-plate with a $1\frac{1}{2}$' hole provided to allow an iron rod to pass through them.

The hybrid machine was setup to be belt-driven similar to belt-driven starters/generators used to run induction machines by coupling with an engine. Belt-driven induction machines or starter-generators are often easier to design and deploy in contrast with flywheel-mounted systems, which require elaborate power-train modifications and in many cases gives rise to additional issues which tend to shift the focus of research. The prototype machine based on a belt-driven system mounted on rails is described further in this chapter.

## 6.2.1   Mounting Arrangement

The original method of attachment was to use aluminum feet that were to be secured to the ring around the stator. The feet were to be bolted to the outer radial face of this ring and placed appropriately to provide a base wide enough to give support to the structure and level the machine. Then a securing mechanism would be used to attach the feet by bolting them to a block which in turn is fixed into the baseplate of the dynamometer described earlier.

However after the machine was assembled it was seen that several aspects of this mounting scheme could not be realized and a new scheme as described below had to be implemented. On assembly, two iron plates one of which is shown in the dimensioned Figure 6.1 was fixed to the outside of the endplates and aligned such that an iron rod could be passed through them. As mentioned above this rod behaves as the pivoting point of the entire machine assembly.

The rod is bolted to the iron rails using angle-irons, a Solidworks impression of which is
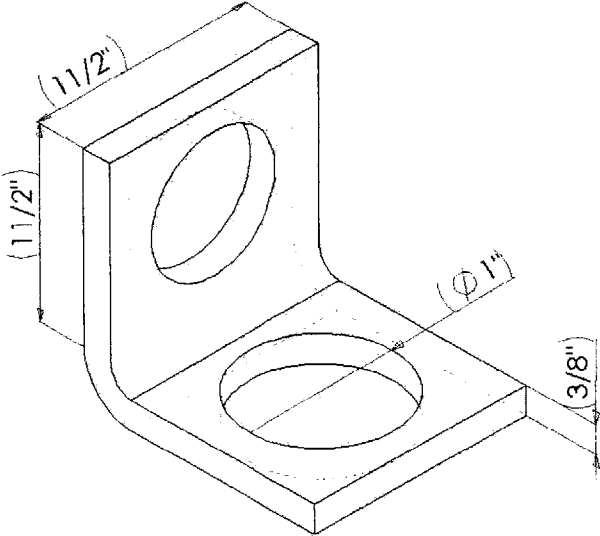
(a) Solidworks impression of an angle iron.
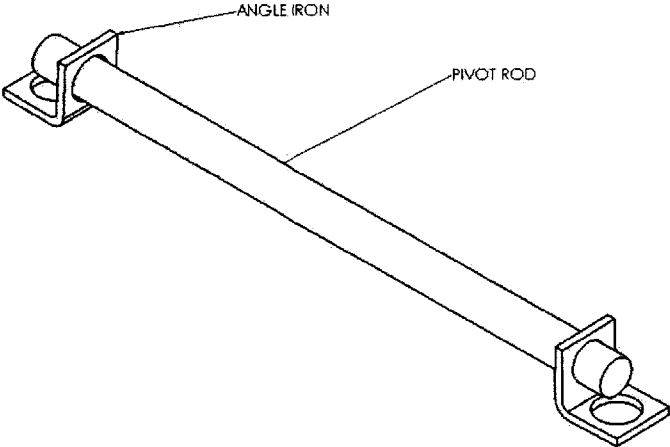


(b) Assembly of angle irons and pivot rod beneath the machine.

Figure 6.2: Angle iron were used to transfer the weight of the machine from the end plates to the rails. The holes permit one side to be fixed to the rail while the other side allows a 1" rod which passes through a similar angle iron fixed to the other end plate.

shown in Figure 6.2(a), serving to transfer the weight of the assembly from the end-plates to the rails and to the support structure beneath. A picture of the pivotal rod assembly beneath the machine is shown in Figure 6.2(b).

## 6.2.2 Support Structure

The machine is supported on either side by turnbuckles which transfer the weight of the structure over a wider area. Being adjustable as they are, it is easy to monitor the tension on the belt and also keep the machine from vibrating too close to the support structure's resonant frequency. Machine vibration, magnified by resonance is almost always due to non-rotating parts such as a segment of the iron rails at the base, support columns or turnbuckles. A non-rotating part is said to be the source for amplitude magnifying resonance in approximately 15-20% mechanical machines. However many engineers, until they see these numbers, do not regard this phenomenon as their own experience is limited to relatively fewer machines. When magnifications become very large resonance is easily detected. On the other hand when source vibration is, for instance, about 12% away from the peak of the resonance curve, the magnification is no more a serious consideration and resonance may not be detected.

Initial test runs of the machine were carried out at approximately 300-360 rpm (dynamometer speed) and excessive vibrations of the machine were witnessed as the speed rose. This was attributed to poor rotor balancing at the manufacturing stage. The power rotors were 'statically' balanced and that turned out to be insufficient.

## 6.3 Drive Mechanism: Belt Drive and Sheaves

To couple the hybrid machine to the dynamometer a system of pulley sheaves and belts were used. The taper-lock sheave on the machine side is larger and bears a ratio with the dynamometer side sheave of approximately 3:1. The machine side sheave is locked on the shaft using its taper-lock facility and a key that was fashioned to fit in a groove running along the length of the shaft.

These sheaves and the belt had to be regularly checked for damage and wear which was expected because of the irregular setup. One of the chief reasons why belts are a better choice than chains is because they tolerate misalignment better than chain systems, but that does not make sheave alignment anything less to worry about. Misalignment could lead to uneven wear on a single side of the belt or cause the belt to roll over in the sheave and place all the load on one side. It can also cut drastically into belt life, causing excess energy consumption and serious running noise.

Before starting, and each time the belt is 'tensioned' or 'untensioned', alignment must be checked and drive train maintenance carried out if necessary. A misalignment of more than

| Model Number (old) | 9 - 023 - (4 - 3) |
| --- | --- |
| Model Number (new) | 2804T |
| Serial Number | 9T - 1554 - 2989 |
| Maximum Speed | 75000 rpm |
| Range | 4000 Lb.in. |

Table 6.1: MCRT® Torquemeter Specifications

half a degree should be corrected immediately for most drive belts.

One of the final and most important pre-run checks of a drive component inspection is belt tension. Too much tension potentially stretches the belt and thus speeds up the belt wear and tear process and shortens bearing life. If belt tension is too lax it could result in belt slipping which also shortens belt life and wears the sheave. The ideal tension is the minimum magnitude of tension at which the belt will not slip under peak load conditions. Tension testers and tables of recommended values are available from belt manufacturers' and distributors' websites. For increased belt speeds, larger sheaves and longer belts are recommended. This scheme often often saves energy and improves efficiency. Larger sheaves also applies lower stretching stress on the belt and eases tension.

## 6.4 Torquemeter

A torquemeter is installed between the load motor and the drive. An MCRT® torquemeter which measures static as well as dynamic shaft torque is used on the drivestand.

The torquemeter requires a signal conditioner or a carrier amplifier with AC excitation. The carrier frequencies are within the range of 2.4 - 6 Khz. Optimum operating characteristics are achieved at 3 Khz. Signal conditioners used for this purpose must satisfy a set of requirements. General Specifications and further information on this device can be found in [7]. The name plate details are given in Table 6.1.

At several instances when the machine was stationary, significant noise interference was present. This was due to the fact that our setup lives on a laboratory floor with several other electric and electronic equipment at different stages of operation. Following from the
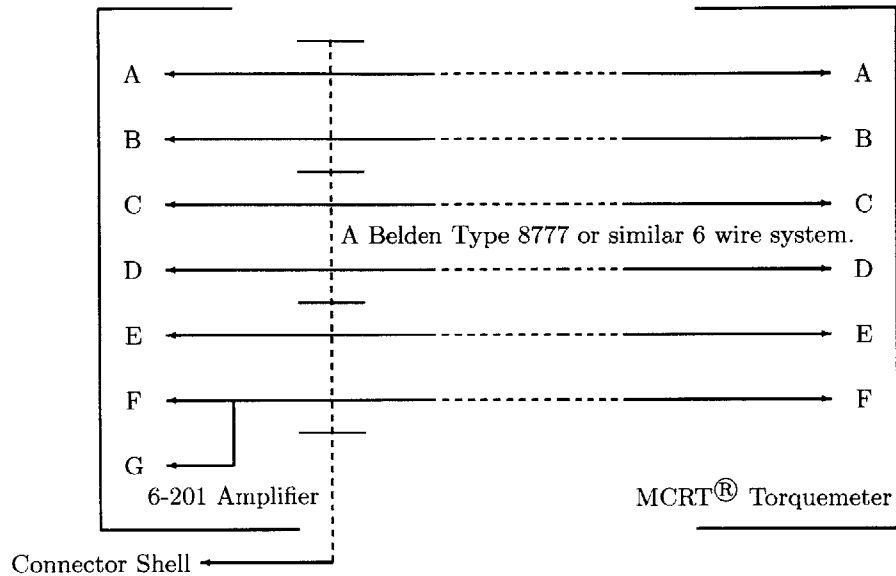
Figure 6.3: 6-Wire connection preferred cable system for the torque connector lead of the torquemeter.

manual instructions for 'Erratic Output When the Shaft is Stationary'(D.4.3 on Page 16 of Manual), the instrument was isolated from the machine by powering it with a different source. The noise in the proximity was reduced using shielded wires.

The torquemeter had been already installed on the shaft for its previous application in accordance to the installation procedures outlined in the manual. The torquemeter is bidirectional (CW - clockwise with positive output, CCW - counterclockwise with negative output) and its output polarity reverses with the direction of the transmitted torque. In our application we are only concerned with CW torque. The convention followed by Himmelstein in this case is to look from the drive end. If the shaft turns clockwise then the torque is CW, and otherwise, CCW.

Two leads appear on the periphery of the torquemeter. One is an optional speed signal lead and the other a torque signal lead. The torque connected has six pins labelled A-F for excitation, excitation senses and the signals. A six wire cable (Belden Type 8777 computer cable was used in our setup) combined with a suitable carrier amplifier adds an excitation sense function and this combination in accordance to the manual regulates the excitation at the torquemeter rather than at the amplifier as is the case in other wiring systems (4 wire or 7 wire). It is hence the preferred cable system and the wiring diagram is shown in Figure 6.3.

## 6.5    6-201 Transducer Amplifier and the Power Instrument

This section briefly introduces the 66032 Power Instrument and its components. The model 6-201 is a 3 KHz transducer amplifier with a low pass signal filter and the facility for selecting cut-off frequencies. Important specifications are given in Table 6.2. The Model 66032 Power Instrument measures and displays torque, speed and other physical parameters such as force and velocity.

### 6.5.1    Signal Conditioning

The 6-201 and a crystal-based digital counter are used for signal conditioning. Channel 01 and Channel 02 are 7-pin female connectors that are used to interface the two with the the 66032 Power Instrument. The Digital Counter has a range from 10 - 99,999 Hz and is essentially independent of waveform. Its sensitivity is 5 mV and handles a maximum of 136 V(rms).

Other units contained within the 66032 are an Analog to Digital Converter, Digital Displays and an Internal Z80A Processor (32K, 8K CMOS static RAM) with selectable baud rates from 75 to 19200 Baud.

Detailed information on how to operate the 66032 as well as programming instructions can be found in [6]. Most of the initial setup and testing was already done as part of a previous research project [21].

## 6.6    Servo System

The drive to the hybrid machine is provided by a load motor, the nameplate details of which is given in Table 6.4. This motor is controlled using a motion control package called VEC-TORSTAR (Manufactured by Kollmorgen Motion Technologies Group, the VECTORSTAR Programmable Positioning System is now obsolete). In this section relevant details of the setup and running procedures are discussed purely from the operational point of view. The intention of this section is not to present a detailed description of the system but rather its interfacing with a computer and its control mechanism. Detailed instructions on how to setup, test and run the package is given in the Technical Manual listed in the bibliography as [3].

### 6.6.1    Setup

Connector C5 on the VECTORSTAR is the serial communications connector and is located on the front panel. It is a 9-pin, D-type sub-miniature plug connector (DE-9P) and the

| | |
|---|---|
| Transducer Impedance | 80-2000 $\Omega$ |
| Amplitude | 6 V(rms), regulated |
| Frequency | 3Khz $\pm$ 1% |
| Sensitivity | 0.3 mV/V |
| Sensitivity Range | 5 - 0.3 mV/V |
| Input Impedance | 25 M$\Omega$ |
| CMR | 120 dB |
| Filter Attenuation | 80 dB per decade above cut-off frequency |

Table 6.2: Signal Conditioner(Strain Gage Amplifier): Model 6-201 Transducer Amplifier specifications. (Adapted from *S. Himmelstein and Company* Operating Instructions.)
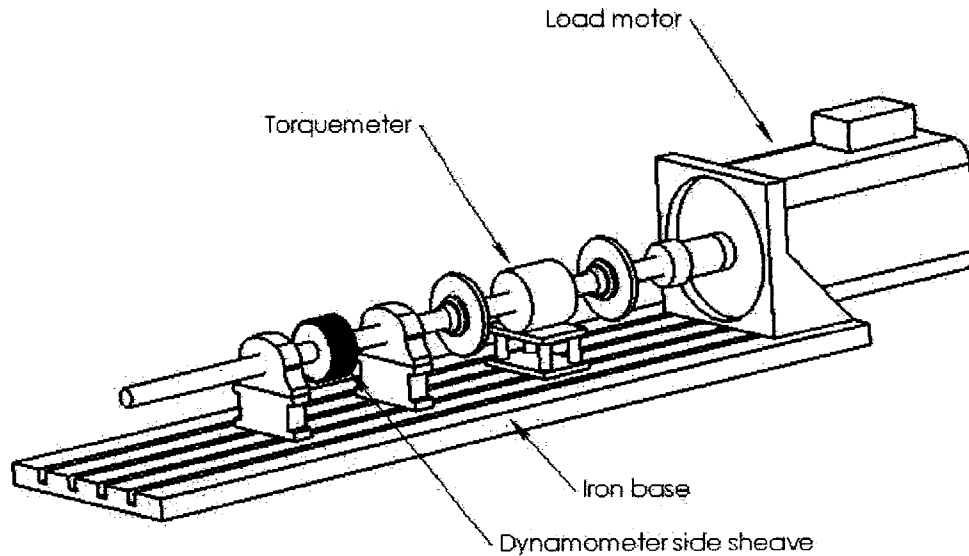
Figure 6.4: Drive mechanism: SOLIDWORKS impression of the drivestand assembly used to operate the hybrid machine.

communications cable must have a mating DE-9S connector. The wiring diagram of the RS-232 scheme for connectivity to a terminal computer is adapted from the manual ([3], Figure B.4 Serial Port.) and can be found in the appendix, Figure A.4.

There are two different setup schemes for communication with a terminal and either scheme has certain advantages and disadvantages. A 3 wire-with-shield cable was used with the DE-9S Connector. RS-232 is simple, universal, well understood and supported. It generally works well over short distances (upto 40 ft. according to the manual) and length of the cable can affect the selection of baud rate. Most computers are fitted with one 9-pin RS-232 serial port. Wiring of the RS-232 terminals is given in Table 6.3.

Once communications are setup and initial test runs are conducted, the system is ready to

| VECTORSTAR (DE-9P) Female | | IBM-PC (DB-25S) Female |
|---|---|---|
| 1 | SHIELD | 1 |
| 2 RxD (receive) | | RxD 2 |
| 3 TxD (transmit) | | TxD 3 |
| 5 (ground) | COM | 7 |

Table 6.3: RS-232 PC Wiring

receive instructions. In the next section a step-by-step approach to turning on the machine is presented. As we are dealing with a belt and sheave mechanism, a belt guard was built from acrylic plastic and installed to complete cover the rotating larger sheave and most of the exposed belt.

## 6.7 Machine Operation Instructions

On the front panel of the 66032 is a keyboard that can be operated in two modes (OPER and PRGM). Except for the initial setup stage our experiment bypasses usage of this panel. The possible values for baud rate are: 75, 110, 150, 300, 600, 1200,2 400, 4800, 9600 and 19200(entered as 1920). Since we are using the 66032 for most of the initial tests in read-out mode, nothing further needs to be done except create a hyperterminal connection.

To communicate with VECTORSTAR, the settings for our hyperterminal application is presented in Table 6.5.

The RS-232 serial port on the PC is configured as Date Terminal Equipment (DTE) which is the standard default configuration. The VECTORSTAR manual cautions that the PC and VECTORSTAR *must* share the same power supply to prevent damage to either machine due to the voltage difference.

The steps for starting the load motor and hence the drive system are presented in Table 6.6.

| | |
|---|---|
| Voltage at Base Speed (L/L) | 230 V |
| Current at Base Speed | 95 A(rms) |
| Maximum Speed | 4000 rpm |
| base Speed | 575 rpm |
| Constant HP Speed Range | 6.1 |
| no. of Phases | 3 |
| Rated HP | 20 |
| Model Number | V3144-BE24-004 |
| Serial Number | 99G319-501 |

Table 6.4: Nameplate Details of the Variable Frequency AC Load Motor used to drive the hybrid machine.

| Hyper Terminal Field | Value/Setting |
|---|---|
| Baud Rate | 9600 |
| Data Bits | 8 |
| Parity | None |
| Stop Bits | 1 |

Table 6.5: Hyperterminal settings for VECTORSTAR communication.

| | Steps to start load motor via Windows Hyper Terminal. |
|---|---|
| 1 | Precautionary Procedures: Ascertain the immediately area around the test machine and the load motor setup is cleared of loose items. Check to confirm that MOTION switch is turned OFF. |
| 2 | Turn on Power supply (230 V) |
| 3 | Check Hyper Terminal settings (Settings appear as "9600 8-N-1" on the status bar of the application). |
| 4 | When the prompt ('--→') appears, communication link has been established. |
| 5 | PULL out red STOP button. |
| 6 | PUSH black START button |
| 7 | Type 'ok2en' at Hyper Terminal prompt. 7.a If '0' is displayed, recheck all required initial conditions. Other scenarios may be possible depending on the Error message. 7.b Continue to next command. |
| 8 | Type 'en' at Hyper Terminal prompt. |
| 9 | Type 'j <*speed*>'. at Hyper Terminal prompt. Machine speed should be increased in a gradual manner from 0 to <*upper_limit_speed*>. |
| 10 | Termination: machine speed MUST be reduced gradually in small decrements of speed, say 25 rpm. |
| 11 | Turn MOTION switch OFF. |
| 10 | PUSH in red STOP button. |
| 10 | Turn off power supply. |

Table 6.6: Algorithm to start generator for testing. *(Adapted from Start-up instruction sheet, R. Pilawa).*

Chapter 7

# *Conclusions: Using Wind Data and Future Work*

The goals of this research thesis was to model the dynamic behavior of the proposed hybrid technology machine and to present a detailed description of the constructional features. Moreover a set of preliminary low speed tests results from the machine were presented.

Experimental Power curve determination techniques and the procedure for constructing an actual full-blown simulation model of the entire wind turbine system are briefly introduced in an effort to appreciate the nature of work yet to be accomplished before this machine can be taken off the laboratory floor. This should lay the groundwork for forthcoming research on this technology. Our hybrid machine currently does not have an associated turbine arrangement for actual field measurements or even the capability to use simulated data. Further work is expected to move along the lines of developing or using an existing wind-wind turbine interaction model.

## 7.1   Wind-Wind Turbine Interaction Modeling

The analysis for the latter begins with the the blade element theory which explain related phenomena and energy capture by the rotor blades. The nature of wind is extremely complex and has stochastic magnitude as its intensity and direction varies in space (millimeters to kilometers) and time (milliseconds to even months). Fictitious wind regimes are generated for this simplified model and are not actually obtained from meteorological measurements. A turbulence intensity that is representative of the conditions that is being modelled is chosen and wind data that fits this profile is generated. One could, of course also comb data sets for winds of the desired mean and turbulence intensity, but that is a lot of work and these simulation codes haven proven very useful and are designed to correctly represent wind characteristics.

Following the above realization, wind seen by the rotor is modelled using either software such as SNLWIND-3D[1] or using one of many good generation methods available. An instance of wind profile generation is the temporal series of non-homogenous incident wind speed field on a turbine. A famous generation technique is the Shinozuka method where cosines of random frequencies for each temporal point are added with the magnitudes obtained

---

[1]A stochastic, full-field, turbulent-wind simulator. The code can be obtained from *http://wind.nrel.gov/designcodes/simulators/snlwind3d/*

from the spectrum altering the mean and variance of the wind speed. Thus in order to achieve a reliable power curve, the best way would be to use simulated wind that has the characteristics that your desire. SNLWind-3D can be used to generate turbulent wind data with a specified mean wind speed and turbulence intensity while other NREL codes may also be used to generate just hub height wind.

Before embarking on this aspect of our research work, a trivial solution was attempted as an alternative to the above modeling method. 20 Hz m/s data (hub height 80 m, Mt. Tom) was acquired from researchers at the Renewable Energy Research Laboratory, University of Massachusetts, Amherst and scaling techniques applied as a simplified method to the problem. This idea was abandoned when it was realized that such a trivialization was not representative of actual wind profiles experienced by turbine rotors in the field.

Simulating the extraction of kinetic energy contained in the wind using the above developed model is excruciating as the simulation is extremely slow since the Shinokuna process requires enormous processing power. Further development of a faster simulation model is described in [4].

Power curve modeling allows prediction of wind farm power for a predicted wind speed and direction. This modeling is been carried out by means of different methods based on statistical tools and is not related to the core nature of this thesis work.

## 7.2  Power Curve of a Wind Turbine

The power curve of a wind turbine is a graph that plots electrical power output for the turbine at different wind speeds.

### 7.2.1  General Methodology

Power curves are found quite simply by actual field measurements using an anemometer[2] which is placed a little distance away from a live operating wind turbine on a regular reasonably windy day. Assuming that the anemometer is distanced sufficiently away from the turbine to escape artificial turbulence caused by the rotor blades, the readings can be plotted against the electrical power output of the turbine to create the power curve.

---

[2]The measurement of wind speeds is usually done using a cup anemometer. The cup anemometer has a vertical axis and three cups which capture the wind and records electronically the number of revolutions per minute. Ultrasonic or laser anemometers detect phase shifting of sound or coherent light reflected from the air molecules.

## 7.2.2 Power Curves: Uncertainties

There are several uncertainties in the methodology described above due to the fact that wind speed fluctuates substantially. High error percentages (a 3% in wind speed data could lead to a 9% estimation error in energy extraction), poor reproducibility of a power curve in a certain area, variations in temperature and pressure etc. all affect the accuracy and reliability of a power curve. Wind turbines reach their rated power at their rated wind speed in meters per second (m/s). Rated power is different from peak power (they could be the same on occasion).

## 7.2.3 Simulation Models for Wind Turbines

Exhaustive literature exists on overall modeling of DFIG wind turbines and since our machine is not very different from the original DFIG, turbine models intended for use with DFIGs can be inserted into the system for our purpose. [8] is a good introductory paper to Wind turbine modeling for power systems dynamics. The authors also present argument that it is possible to reuse the same power system dynamic simulation model for different kinds of variable speed wind turbines. It may also be viable to use the pre-defined components in the MATLAB Power System Simulation package for initial analysis. The issue here is that shaft torque in our machine depends on the turbine control system and the generator dynamic response. A power curve also depends on the control system and rotor dynamics which once once fixed becomes just a measure of the steady state generator efficiency and the effects of the mean of any non-linear responses to the higher frequency control responses and dynamics.

# 7.3 Summary of Completed Tasks

A few preliminary tests like the ones outlined in Chapter 5 were carried out and their results documented, though these results do not provide much insight into what behavior may be expected of the machine when connected to a stiff voltage source for example. With the completion of this thesis work however, it is expected that the design and construction of the machine has reached closure. Fabrication of most accessories such as the brush-holder and slip-ring assemblies have been completed with the exception of the control system. A power electronics package has also been developed and tested. Simple mathematical models of the machine were built and evaluated for dynamic behavior as well as the steady state response characteristics which were simulated in MATLAB. The steady-state description of the machine was extended to model dynamic behavior using linearization and a simplified but complete state-space model was produced. The stability of the system with variation in PM rotor damper circuit resistance has been examined and the critical point beyond which the machine might go unstable has been documented. The controller for the machine has been considered in previous literature with the aim to deliver optimum real power to a 3-

phase voltage source connected directly with the stator windings. Typically, by controlling the power rotor excitation as well as the shaft speed, this can be achieved.

Thus the PM rotor dynamic behavior, which was the primary concern of this endeavor, was analyzed and will be useful at a later stage. The slip-rings and brush-holder assembly were constructed as outlined in Section 2.4.1. The next section describes some of the technical problems associated with this assembly and how they must be overcome before moving forward with this project.

So far ventilation has not arisen as a major concern, but it has been addressed in prior work as well as in Chapter 2 of this thesis in a general fashion. Assembly of the machine took place on the laboratory floor of the LEES workshop and involved several tasks and personnel.

Some effort has been expended on acquiring data for the testing phase of the machine from researchers at the University of Massachusetts, Amherst through the Laboratory for Energy and the Environment (LFEE) at MIT. As described earlier in this chapter, a fully defined model of the wind turbine system and wind interactions with the turbine has to be developed before comparison parameters with conventional and competing technologies can be wholly defined. Hence this aspect of the work remains yet to be accomplished and will be the subject matter of future literature on this hybrid technology.

## 7.4 Recommendations for Future Work

### 7.4.1 Wind Data: Wind-Wind Turbine Interaction phenomena modeling

There are other aspects of simulation that need to be considered from the perspective of the investigator who decides what observations are worth recording. Turbulence occurs at frequencies of say below 1 Hz and rotational sampling of turbulent eddies occurs at harmonics of the blade passing frequency (approximately 2 Hz and up). Blade vibrations occur at higher frequencies. Will this translate into current spikes due to sudden torque changes or should the model be designed to ignore these effects and just measure steady state variables?

For a variable speed machine the torque is a function of mean wind speed, turbulence, the rotor design, blade pitch, control system and speed. Now considering that the hybrid machine is a new system, it would be prudent to measure efficiency at different operating speeds and torques. Once this were done, then one could think about how to use it in a wind turbine. Neglecting higher frequency effects and recording simply the response to turbulence, the easiest way test the hybrid machine[3] would be to propose a rotor with a given $C_p$ Vs. tip speed ratio curve (" $C_p$-$\lambda$" curve; assume fixed pitch) and a proposed control algorithm (rotor speed Vs. torque or wind speed or power level) and then using

---

[3]Thanks to Prof. Anthony L. Rogers, RERL, Univ. of Massachusetts, Amherst for pointing this out.

sample turbulent wind data and the $C_p$-$\lambda$ curve to determine rotor power and from that, rotor torque and speed(rpm) using the control algorithm. Using a variety of wind speeds, a power curve can be determined. How comparable that would this curve be with other turbines will be unclear at first, given the possible variations of control algorithms and rotors. A simple $C_p$-$\lambda$ rotor model can also be implemented in MATLAB.

Another possibility for further consideration is operation at constant $C_p$ up to some pre-determined wind speed, then constant power and constant speedy. Using sample turbulent wind files, once could easily determine the power/rpm during constant $C_p$ operation. During constant power operation, the power and speed(rpm) are fixed, so is the torque.

### 7.4.2 Power Electronics and Controller

The power electronics package has been built and tested on the machine with mixed results. Further development and testing is necessary. Standard controllers are expected to suffice and there are copious amounts of literature which document control algorithms for generic doubly-fed induction systems. [19] suggests the use of a programmable microcontroller as the heart of the control system. DC servomechanisms for velocity and position control are described in [1]. Chapter 5 of this work also suggests the precise microcontroller that may be used for the purpose. Effort has been expended to program the microcontroller to generate the required signals for the control circuitry, but much work remains to be done.

### 7.4.3 Mechanical Engineering Tasks

Starkly put, the machine was not a model of good mechanical engineering design and practice. At the time of writing this, the machine had to be taken apart again to determine the source of the imbalance in the PM rotor assembly. Based on several investigations, a theory for why this might be occurring was developed.

With the machine stationary, several marks were made on the periphery of the power rotor and it was gently rotated noting the orientation of the PM rotor with the power rotor every time the PM rotor assembly jerked. This was noticed to be occurring periodically at the close of each revolution and the intersection point between the PM rotor and the power rotor mark when it happened travelled a few degrees/revolution in the direction of the rotation. Next, with the power rotor locked and rotating just the PM rotor assembly it was observed that there was no sudden shifting motion. A first analysis of this behavior indicates that the shaft might be bent. If this is the case, considerable amount of work will have to be done to rectify the problem. However, we suspect there might be another possible explanation for the problem that will be easier to fix if it turned out to be right. Another interesting observation was that if the PM rotor assembly was pried at, using a long handle crowbar, it would shift about an axis passing diametrically through the cross-section of the machine. The axis remained at the same point on the the frame of the power rotor (i.e., it did not travel. This can be easily verified by spinning the driveshaft and repeating the test). What

this reveals is that the inner race of the angular contact bearings is not a tight fit and allows the driveshaft to wobble in it. To fix this problem we are currently disassembling the machine to gain access to the free-wheeling shaft.

An unrelated, but equally important task to be carried out is to ensure that the brush contacts are secure and steady at all orientations of the driveshaft and while spinning. At the moment the copper rings are not provided a constant contact surface and will need to be removed and cleaned.

### 7.4.4 Developing Machine Models

Further analysis should be done to more fully specify the dynamic operating characteristics of the machine; indeed this will entail increasing the order of the model. Using the model, capability, compounding, and vee-curves have to be developed and compared with experimental results which can be obtained after successfully synchronizing the machine against a stiff voltage source. This should conclusively demonstrate the utility of the new design geometry.

### Conclusion

In conclusion it is our hope that we will soon be able to contribute a meaningful new geometry that will have much to offer the wind energy community in terms of cost-effectiveness and reliability as well as ease of manufacturability. On several occasions it has been quite inaccurately pointed out to this author that research in this field has long reached maturity. Much work remains to be done to develop efficient wind turbines and generators that could have a substantial impact on future energy production technologies and solutions for sustainable generation.

*"Fundamentally, sustainable development is a notion of discipline. It means humanity must ensure that meeting present needs does not compromise the ability of future generations to meet their needs."*

– Dr. Gro Harlem Brundtland

# List of Symbols

A comprehensive list of symbols used in this thesis appears here. Note that several symbols in the text may take on different meanings depending on the superscript/subscript. The rotor/stator-defined PM machine are subscripted 'R'/'S' depending on the quantity being described.

$\beta$    Is the wave propagation constant., page 19.

$\delta$    Rotor angle, rad/sec.

$\lambda_0$    zero-sequence axis flux linkage. amp-turns.

$\lambda_d$    d-axis flux linkage. amp-turns.

$\lambda_q$    q-axis flux linkage. amp-turns.

$\lambda_{dr}$    d- axis power rotor related flux linkage, amps-turns.

$\lambda_{ds}$    d- axis stator flux linkage, amps-turns.

$\lambda_o$    PM flux placed in the d- axis of the rotating frame, amps-turns.

$\lambda_{qm}$    q- axis PM rotor 'damper' related flux linkage, amps-turns.

$\mu_o$    Permeability of free space, $WbA^{-1}m^{-1}$.

$\mu_r$    Relative permeability.

$\omega_0$    Synchronous angular speed, rad/sec.

$\Omega_m$    Mechanical speed, rad/sec , page 20.

$\omega_r$    Rotor difference frequency in angular velocity units, rad/sec.

$\psi_0$    Internal field flux due to the permanent magnets in the system in per-unit notation.

$\psi_{ad}$    Armature, d- axis mutual flux linkage, per-unit notation.

$\psi_{aq}$    Armature, q- axis mutual flux linkage, per-unit notation.

$\psi_d$    d- axis flux linkage, per-unit notation.

$\psi_{kd}$    Damper, d- axis mutual flux linkage, per-unit notation.

$\psi_{kq}$    Damper, q- axis mutual flux linkage, per-unit notation.

$\psi_q$    q- axis flux linkage, per-unit notation.

$\tau_e$    Electrical torque produced by the machine, Nm.

$\tau_m$    Mechanical torque due to loading, Nm.

$\theta_o$    Initial angle between the rotor d- axis and the primary phase of the stator winding. Angle of the rotor at time t=0, rad.

$\underline{T}$    Park's Transform. Its inverse is $\underline{T}^{-1}$ , see equation (3.3), page 21.

$A_c$    Stator core cross-sectional area, $m^2$ or $mm^2$.

$B_s$    Peak flux density in the stator, T.

$g_s$    Stator-to-power rotor air gap, mm, see equation (3.1), page 20.

$H$    Intertia constant defined as $\frac{\text{Rotational kinetic energy at rated speed}}{\text{Base Power}} = \frac{J\omega_0}{2pT_B}$, where $T_B$ is the base torque.

$i_d$    d- axis current, per-unit notation.

$i_{f0}$   Steady state field current, per-unit notation.

$i_{kd}$   d- axis damper winding current, per-unit notation.

$i_{kq}$   q- axis damper winding current, per-unit notation.

$i_{qm}$   q- axis PM rotor 'damper' related current, amps-turns.

$i_q$   q- axis current, per-unit notation.

$I_r$   General form of current squirted into the rotor. This current can be DC or three phase AC., amps.

$I_s$   Current in the stator coils, A.

$J$   Rotational intertia constant of the machine.

$L$   Inductance, H.

$L_{dr}$   d- axis self-inductance refered to rotor, H.

$L_{ds}$   Self-inductance. The subscripts for these quantities are self-explanatory, H.

$M$   Mutual inductance in its most general form, H.

$N_s$   Number of turns in a stator coil.

$p$   Number of pole pairs (10 in this hybrid technology machine).

$P_r$   Power in rotor, w.

$P_s$   Power dissipated in the stator, w.

$r_a$   Per-unit armature resistence.

$r_{kd}$   Per-unit d- axis damper winding resistence, rad/sec.

$r_{kq}$   Per-unit q- axis damper winding resistence.

$s$   Slip fraction $= \frac{P_r}{P_s}$.

$T_e$   Per-unit electrical torque produced by the machine.

$T_m$   Per-unit mechanical torque due to loading.

$T_r^e$   Electrial Torque due to the power rotor currents, per unit notation.

$T_{shaft}$   External Torque applied on the shaft, per unit notation.

$T_s^e$   Electrial Torque due to the stator currents, per unit notation.

$v_d$   Per-unit voltage on the d- axis. If subscript 'S' appears the symbol refers to the stator-PM rotor synchronous machine.

$v_q$   Per-unit voltage on the q- axis. If subscript 'R' appears the symbol refers to the power rotor-PM rotor synchronous machine.

$x_{ad}$   Armature, d- axis mutal flux linkage reactance, per-unit notation.

$x_{aq}$   Armature, q- axis mutal flux linkage reactance, per-unit notation.

$x_d$   d- axis reactance, per-unit notation.

$x_{kd}$   d- axis damper winding reactance, per-unit notation.

$x_{kq}$   q- axis damper winding reactance, per-unit notation.

$x_q$   q- axis reactance, per-unit notation.

H   Magnetic field intensity, A/m.

# Machine Pictures and Data Sheets

This section contains images and drawings of different parts of the generator and test-rig during the design and construction process. Microcontroller Data sheets as well as a VECTORSTAR wiring diagram are also presented.
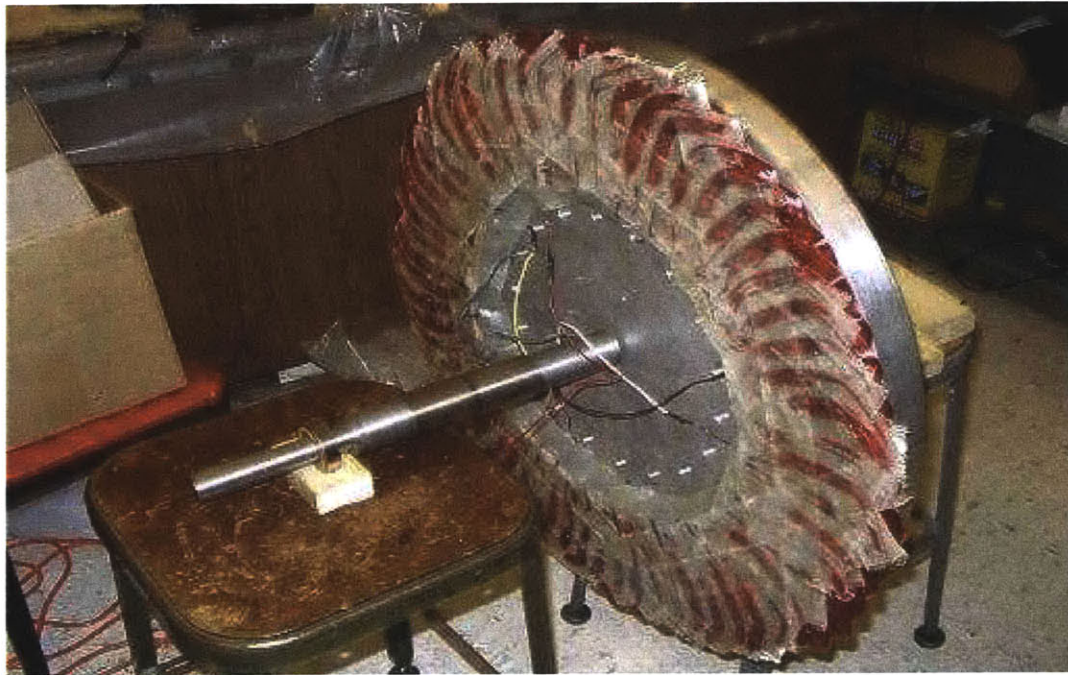
Figure A.1: Wound power rotor fabricated of 120 coils using standard 16 AWG wire and finished with epoxy and glass cloth wrap. the aluminum plate on which the arrangement is mounted is slotted for ventilation and has a keyed hole at the center. This component has a mirror component similar in every aspect. After fabrication the rotor was balanced using a 'static balance' technique; adding/removing material from the outside face just inside of the outer periphery by drilling holes (removing weight) or screwing bolts (adding weight).
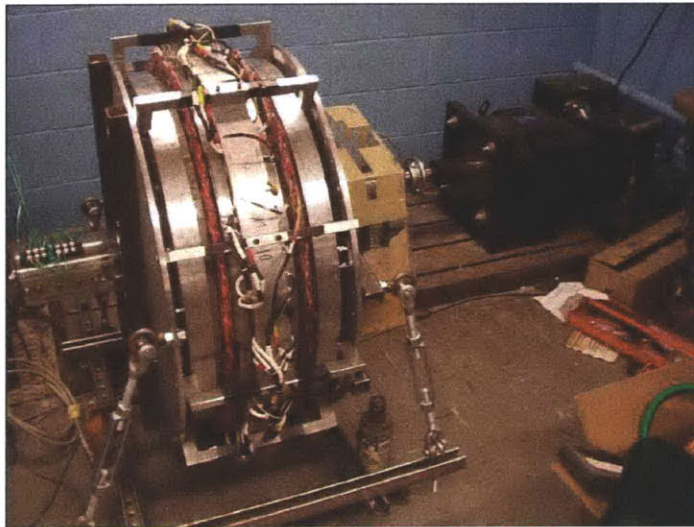
Figure A.2: Assembled prototype of the 20 kW Doubly-fed Permanent Magnet hybrid technology wind generator. Iron rails were used to extend the heavy base of the dynamometer arrangement to mount the machine. Turnbuckles were subsequently used to secure the machine to the rails while further work was being done on the accessories. The load motor used to drive the machine can also be seen in the picture.
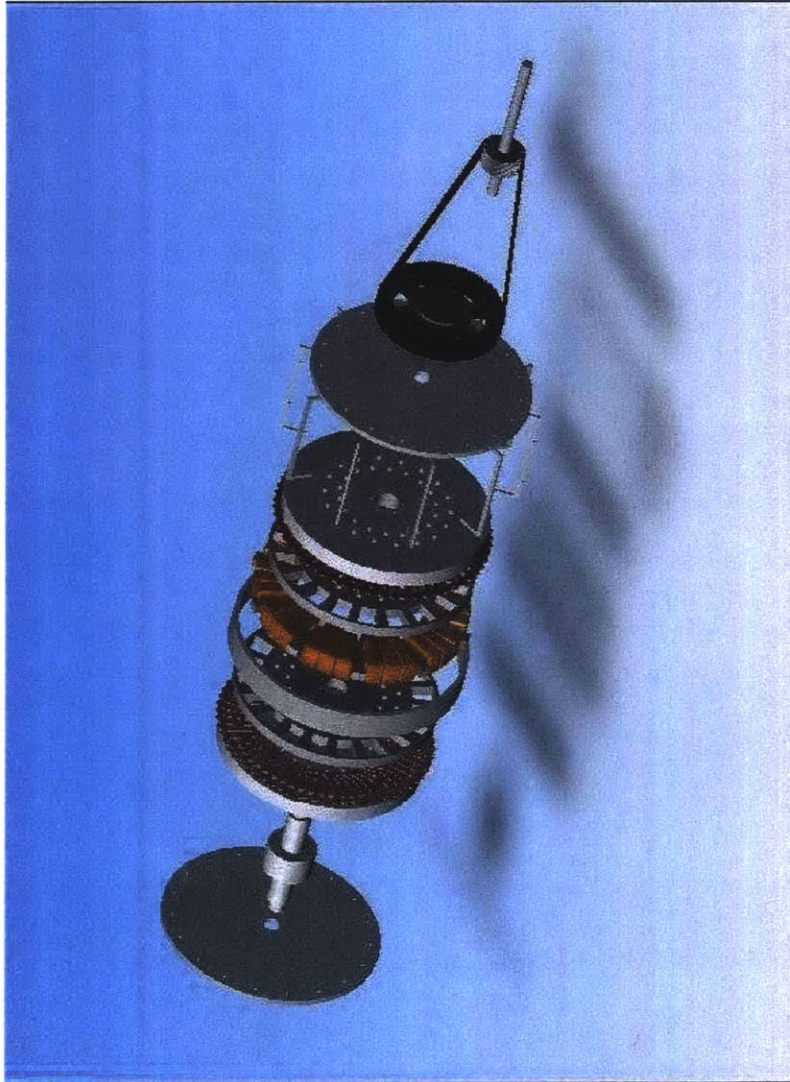
Figure A.3: SOLIDWORKS explosion view of the finished machine.
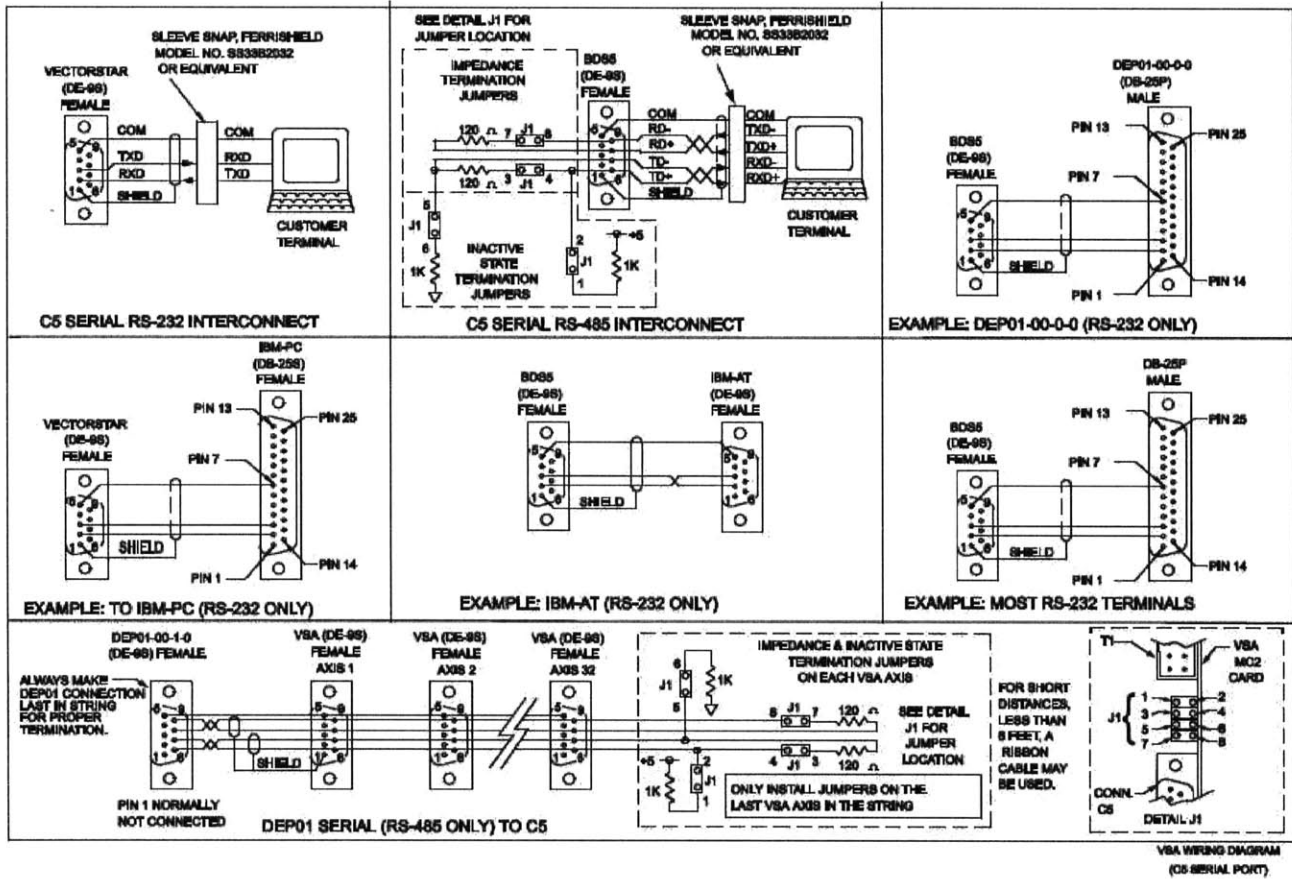
**PDIP (40-pin)**



| | | | | |
|---|---|---|---|---|
| MCLR/Vpp/RE3 | → | 1 | 40 | ←→ RB7/PGD |
| RA0/AN0 | ←→ | 2 | 39 | ←→ RB6/PGC |
| RA1/AN1 | ←→ | 3 | 38 | ←→ RB5/AN13/CCP3 |
| RA2/AN2/VREF-/CVREF | ←→ | 4 | 37 | ←→ RB4/AN11 |
| RA3/AN3/VREF+ | ←→ | 5 | 36 | ←→ RB3/CCP2(1)/AN9 |
| RA4/T0CKI/C1OUT | ←→ | 6 | 35 | ←→ RB2/AN8 |
| RA5/AN4/LVDIN/SS/C2OUT | ←→ | 7 | 34 | ←→ RB1/AN10 |
| RE0/RD/AN5 | ←→ | 8 | 33 | ←→ RB0/INT/AN12 |
| RE1/WR/AN6 | ←→ | 9 | 32 | ← Voo |
| RE2/CS/AN7 | ←→ | 10 | 31 | ← Vss |
| Voo | → | 11 | 30 | ←→ RD7/PSP7 |
| Vss | → | 12 | 29 | ←→ RD6/PSP6 |
| OSC1/CLKI/RA7 | ←→ | 13 | 28 | ←→ RD5/PSP5 |
| OSC2/CLKO/RA6 | ←→ | 14 | 27 | ←→ RD4/PSP4 |
| RC0/T1OSO/T1CKI | ←→ | 15 | 26 | ←→ RC7/RX/DT |
| RC1/T1OSI/CCP2(1) | ←→ | 16 | 25 | ←→ RC6/TX/CK |
| RC2/CCP1 | ←→ | 17 | 24 | ←→ RC5/SDO |
| RC3/SCK/SCL | ←→ | 18 | 23 | ←→ RC4/SDI/SDA |
| RD0/PSP0 | ←→ | 19 | 22 | ←→ RD3/PSP3 |
| RD1/PSP1 | ←→ | 20 | 21 | ←→ RD2/PSP2 |

PIC16F747/777
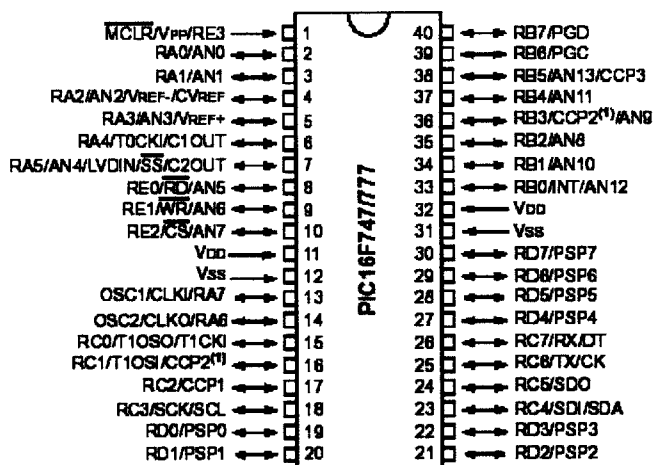
Figure A.5: Pin Diagram of PIC16F7X7, PDIP 40-pin.

| | Units | INCHES* | | | MILLIMETERS | | |
|---|---|---|---|---|---|---|---|
| Dimension Limits | | MIN | NOM | MAX | MIN | NOM | MAX |
| Number of Pins | n | | 28 | | | 28 | |
| Pitch | p | | .100 | | | 2.54 | |
| Top to Seating Plane | A | .140 | .150 | .160 | 3.56 | 3.81 | 4.06 |
| Molded Package Thickness | A2 | .125 | .130 | .135 | 3.18 | 3.30 | 3.43 |
| Base to Seating Plane | A1 | .015 | | | 0.38 | | |
| Shoulder to Shoulder Width | E | .300 | .310 | .325 | 7.62 | 7.87 | 8.26 |
| Molded Package Width | E1 | .275 | .285 | .295 | 6.99 | 7.24 | 7.49 |
| Overall Length | D | 1.345 | 1.365 | 1.385 | 34.16 | 34.67 | 35.18 |
| Tip to Seating Plane | L | .125 | .130 | .135 | 3.18 | 3.30 | 3.43 |
| Lead Thickness | c | .008 | .012 | .015 | 0.20 | 0.29 | 0.38 |
| Upper Lead Width | B1 | .040 | .053 | .065 | 1.02 | 1.33 | 1.65 |
| Lower Lead Width | B | .016 | .019 | .022 | 0.41 | 0.48 | 0.56 |
| Overall Row Spacing § | eB | .320 | .350 | .430 | 8.13 | 8.89 | 10.92 |
| Mold Draft Angle Top | α | 5 | 10 | 15 | 5 | 10 | 15 |
| Mold Draft Angle Bottom | β | 5 | 10 | 15 | 5 | 10 | 15 |

\* Controlling Parameter
§ Significant Characteristic
Notes:
Dimension D and E1 do not include mold flash or protrusions. Mold flash or protrusions shall not exceed
.010" (0.254mm) per side.
JEDEC Equivalent: MO-095
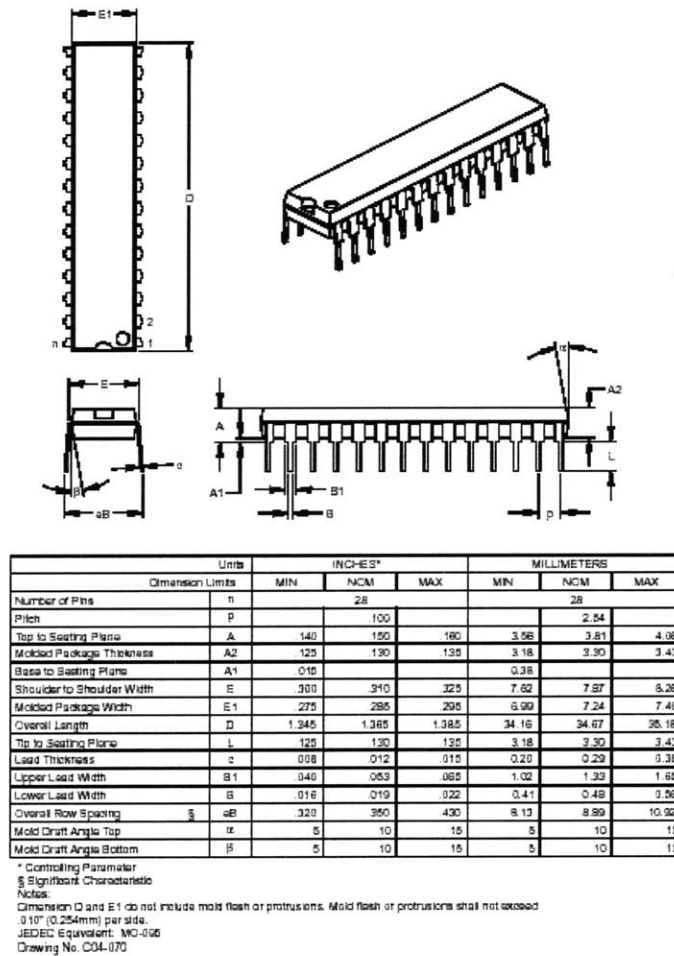Drawing No. C04-070

Figure A.6: PIC16F7X7: Dimensional Drawing.

– 113 –

# *Derivation of Equations 3.31 - 3.33*

A crude back-of-the-envelope mathematical derivation of Equations 3.31 - 3.33 is presented here. 1,2,3...9 represent elements of the 3x3 matrix in Equation 3.30 which can thus be can be rewritten as follows:

$$\begin{pmatrix} a \\ x \\ b \end{pmatrix} = \begin{pmatrix} 1 & 2 & 3 \\ 4 & 5 & 6 \\ 7 & 8 & 9 \end{pmatrix} \begin{pmatrix} y \\ c \\ z \end{pmatrix} \tag{B.1}$$

x, y and z are the unknowns for which expressions will be derived. Equation B.1 can be expressed in another way,

$$a = 1y + 2c + 3z$$
$$x = 4y + 5c + 6z$$
$$b = 7y + 8c + 9z$$

Moving terms around we get,

$$a - 2c = 1y + 3z$$
$$b - 8c = 7y + 9z$$

Also,

$$7(a - 2c) = 7.1y + 7.3z$$
$$1(b - 8c) = 1.7y + 1.9z$$

Hence,

$$[7(a - 2c) - 1(b - 8c)] = (7.3 - 1.9)z$$

$$z = [\frac{7(a - 2c) - 1(b - 8c)}{7.3 - 1.9}] \tag{B.2}$$

$$1y + 3z = a - 2c$$
$$1y = a - 2c - 3z$$

And the other two unknowns are:

$$y = \frac{a - 2c - 3z}{1} \tag{B.3}$$

$$x = 4y + 5c + 6z \tag{B.4}$$

Mapping a,b,c,x,y,z,1,2,3... to their actual elements in Equation 3.30 such that a$\equiv \lambda_{qs}$ and so on, Equation 3.31 can be arrived at.

# Bibliography

[1] H Wayne Beaty and Jr. J. L. Kirtley. *Electric Motor Handbook.* ISBN 0-07-035971-7. McGraw-Hill, New York.

[2] Stephen J. Chapman. *Electrical Machinery Fundamentals.* McGraw-Hill Book Company, 1985.

[3] Kollmorgen Motion Technologies Group. *VectorStar Installation, Setup and User's Manual M96200.* Kollmorgen Motion Technologies Group, 201 Rock Road Radford, VA 24141 USA, 1996.

[4] J.R. Puiggali H. Camblong, M. Rodriguez Vidal. Principles of a simulation model for a variable-speed pitch-regulated wind turbine. *Wind Engineering*, 28, no. 2:157–175(19), May 2004.

[5] L. H. Hansen, L. Helle, F. Blaabjerg, E. Ritchie, S. Munk-Nielsen, H. Bindner, P. Srensen, and B. Bak-Jensen. *Conceptual survey of generators and power electronics for wind turbines.* ISBN 87-550-2743-8. Ris National Laboratory, Roskilde, Denmark, Tech. Rep., 2001.

[6] S. Himmelstein and Company. *Model 66032 Power Instrument Operating Instructions.* S. Himmelstein and Company, July 1989.

[7] S. Himmelstein and Company. *MCRT® mV/V Torquemeter Installation, Operation and Trouble Shooting Guide (Revision B).* S. Himmelstein and Company, 2490 Pemborke Ave., Hoffman Estates, IL 60195, 1991, 1993, 1996. Torquemeter and Calibration and Certification for MIT by SHC. (Factory Ref. 16381-TE, Torquemeter Model: MCRT 9-02T(4-3)).

[8] H. Polinder W.L. Kling J.G. Slootweg, S.W.H. de Haan. Modeling wind turbines in power system dynamics simulations. Technical report, IEEE, 2001.

[9] A. Thomas J.L. Kirtley Jr. Report to national renewable energy laboratory subcontract number xcx-2-32227-06. Technical report, MIT Laboratory for Electromagnetic and Electronic Systems, March 2003. Second quaterly report.

[10] J. L. Kirtley Jr. *Class notes for MIT Course 6.685 Electric Machines Chapter 11*, 2003.

[11] J. L. Kirtley Jr. Dual rotor, constant frequency, variable speed generator. Technical report, MIT Laboratory for Electromagnetic and Electronic Systems, March 2003. Sixth Quaterly Report to the National Renewable Energy Laboratory.

[12] J. L. Kirtley Jr. Dual rotor, constant frequency, variable speed generator. Technical report, MIT Laboratory for Electromagnetic and Electronic Systems, December 2002, June 2003. Proposal and Reports to the National Renewable Energy Laboratory.

[13] P. C. Krause. *Analysis of Electric Machinery.* New York: McGraw-Hill, 1986.

[14] J. B. Ekanayake L. Holdsworth, X. G. Wu and N. Jenkins. Comparison of fixed speed and doubly-fed wind turbines during power system disturbances. In *IEE Proceedings Generation Transmission and Distribution*, volume 150, pages 343–352, May 2003.

[15] Butterfield C.P. Yih-Huie Wan Muljadi, E. Axial-flux modular permanent-magnet generator with a toroidal winding for wind-turbine applications. *IEEE Transactions on Industry Applications*, 35(4):831–836, July-Aug 1999.

[16] G. M. Asher R. Pena, J. C. Clare. Doubly fed induction generator using back-to-back pwm converters and its application to variablespeed wind-energy generation. In *IEE Proc. Electr. Power Appl.*, volume 143 of *3*, pages 231–241, May 1996.

[17] J. C. Clare R. Pena and G. M. Asher. A doubly fed induction generator using back-to-back pwm converters supplying an isolated load from a variable speed wind turbine. In *IEE Proceedings Electric Power Applications*, volume 143, pages 380–387, September 1996.

[18] Lipo T.A. Sarlioglu, B. Assessment of power generation capability of doubly-salient pm generator. In *Electric Machines and Drives*. International Conference IEMD '99, 1999.

[19] A. J. Thomas. A doubly-fed permanent magnet generator for wind turbines. Master's thesis, Massachusetts Institute of Technology, June 2004.

[20] M. S. Vicatos and J. A. Tegopoulos. Steady state analysis of a doubly-fed induction generator under synchronous operation. In *IEEE Transactions on Energy Conversion*, volume 4, pages 495–501, September 1989.

[21] David D. Wentzloff. Experimental characterization of an integrated starter/generator. Master's thesis, Massachusetts Institute of Technology, August 2002.